PORTABLE FAST NEUTRON COMPUTED TOMOGRAPHY SYSTEM FOR VOID FRACTION MEASUREMENTS

PORTABLE FAST NEUTRON COMPUTED TOMOGRAPHY SYSTEM FOR VOID FRACTION MEASUREMENTS

By GARIK PATTERSON, B.Eng.

A Thesis

Submitted to the School of Graduate Studies

In partial Fulfillment of the Requirements for the Degree

Doctor of Philosophy

McMaster University

DOCTOR OF PHILOSOPHY (2023) MCMASTER UNIVERSITY
(Engineering Physics) Hamilton, Ontario, Canada

Title: Portable Fast Neutron Computed Tomography System for
Void Fraction Measurements

Author: Garik Patterson, B.Eng. (McMaster University)

Supervisor: Dr. D.R. Novog

Number of Pages: 1, 204

Lay Abstract

Subchannel analysis codes have been a valuable tool for nuclear safety analysis by providing key metrics such as the degradation of heat transfer from the fuel to the coolant, called the critical heat flux (CHF). Such codes use correlations and constitutive relationships to model two-phase flow parameters, such as the void fraction, as well as empirically derived relationships for complicated two-phase mixing phenomena, such as void drift, which have a direct impact on the flow distribution and hence the heat transfer modelling. In order to both validate existing two-phase flow models and develop more accurate models for complex void phenomena, experimental data are required. However, there is a lack of high-pressure, high-temperature local phase measurements for water-cooled full-scale bundle geometries, which significantly impacts the accurate modelling of two-phase flows in subchannel codes.

Fast neutron computed tomography (FNCT) is particularly suited to such measurements since it is non-intrusive, has high penetration capability for thick metallic structural materials, and provides several point measurements in a single scan. This study outlines the design of a fast neutron portable imaging system through developing suitable imaging models and providing experimental testing to quantify the imaging capabilities based on those models.

Abstract

Subchannel analysis codes have been a valuable thermalhydraulic safety analysis tool for fuel bundle analysis by providing key metrics such as the deterioration of heat transfer from the fuel to the coolant, called the critical heat flux (CHF). To predict the occurrence and location of CHF accurately, experimental data of the void distribution are required to validate the code models. However, there is a lack of such local phase measurements for full-scale bundle geometries, in particular for CANDU geometries, which significantly impacts the modelling of two-phase flow in subchannel codes.

A portable fast neutron computed tomography (FNCT) imaging system is developed to measure the steam-water phase distributions within a full-scale heated bundle at an experimental facility. The system is built to address the need for more local measurement techniques to improve the prediction accuracy of safety analysis codes for nuclear reactor design and licensing. Specifically, the nuclear industry in Canada has identified a major impediment in adopting new and accurate predictive methodologies is the lack of detailed phase-field measurements in realistic full-scale fuel assembly geometries under prototypical full-scale reactor conditions.

This research involves the modelling, design, development, assembly, and demonstration of the functionality of a portable FNCT imaging system to measure the void fraction distribution in a full-scale heated bundle at a thermalhydraulic test facility. The system uses a modern fast-neutron deuterium-deuterium (D-D) fusion generator coupled with state-of-the-art silicon photomultiplier (SiPM) detectors. Key design parameters such as the resolution and void fraction prediction capabilities have been determined to be within theoretical predictions. A first application of machine learning to void fraction imaging has been done to enhance imaging capabilities and increase the effectiveness of void fraction prediction under limited scan time constraints. This study provides a fully operational industry-grade tool for use in advanced thermalhydraulic measurements.

Acknowledgements

Firstly, I would like to acknowledge the financial support of both the Natural Sciences and Engineering Research Council (NSERC) and the CANDU Owner's Group (COG).

I want to thank my supervisory committee, Dr. J-M Le Corre, Dr. L. K. Leung, and Dr. J. S. Cotton for providing valuable technical advice and feedback over the years. I will always appreciate the support in this research, and personally, through the many roadblocks that appeared along the way. I think there might have been some sort of pandemic or something. I would also like to thank the personnel at Ontario Tech for allowing me to use their labs, and for taking the time to babysit me so I could operate their accelerator.

Dr. Novog, I'm not sure there enough pages in this thesis to go through all of the things I have to say. We've worked together for a very long time, and you've taught me not only what it takes to be a researcher, but what it takes to be a truly great leader. You've always led with empathy first. I think if academia and the nuclear industry are populated with leaders like yourself, it is in good hands. So, thank you for supporting me all these years and showing me what it means to be a great leader.

There are many people to acknowledge during my degree. Firstly, Mike, Liz, and Kai, thank you for all of the great discussions in the office and for all of the table tennis tournaments. Phil and Mitch, thank you for all of the amazing discussions in the lab, all of the 5th coffee runs (that were totally warranted), and just being all-around great humans.

To the staff of the Tandem Accelerator Building, particularly Justin and Scott, thank you for your patience and lending your expertise to teach this grad student how to fix and operate accelerators. I can't even put into words the amount of fun I had working with you over the years.

James and Ken. You both taught me so much about thermalhydraulics research, but also how to navigate the lab when things go wrong. I will always value the time you spent teaching me the ropes and making sure I was set up to succeed. Without your mentorship, I would not be nearly as successful in my research.

To all of my friends, old and new, your support and encouragement over the years has given me the drive to push through. You are always there for me and for that I thank you.

Chris, what a ride huh? I was thinking about cutting your section because I only knew you for a brief 10 years, but somehow you made it in. Honestly though, the chats we would have on a daily basis, whether it be about life or our projects, has been invaluable to me and something I will never forget. The amount of time we spent juggling students, fixing lab components, complaining about politics… it all seems like a blur. You have really taught me about what it takes to be a successful researcher. The amount of work you put in has always been an inspiration to me, and I thank you for taking the time to impart that knowledge to me. Now go make some real money.

To my family, thank you for always supporting me through all the stress and my crazy physics rants. Alex: you are always there to inspire me to chase my dreams. I could not have done this without your love, support, and advice. To my mom, that when I first told you about doing a PhD your response was “why?”. Hilarious. As it turns out, I ended up asking that question a lot. In seriousness, you have always been my inspiration, from raising two kids and always supporting whatever we wanted to become, whether it was an artist, a mechanic, or as Keith would put it: “a firetruck”. I hope to one day be as great an inspiration to someone as you are to me.

Table of Contents

List of Figures

List of Tables

List of Symbols and Abbreviations

Symbols

$\boldsymbol{A}$	system matrix
A	attenuation
B	background fraction
d	detector pixel size
E	Energy
f	image domain variable, for resolution calcs: source resolution value void fraction scaling parameter
$\mathcal{F}$	Fourier transform

G	void fraction scaling parameter
I	number of counts
L	light output
M	magnification
N	number of particles per unit volume
p	projection value, for resolution calcs: pixel resolution value
P	probability distribution
$\boldsymbol{r}$	point vector
R	rotation matrix
s	line segment length, for resolution calcs: source spot size value
S	sinogram matrix
t	for image projection: detector coordinate, for scanning optimization: scan time
T	transmission
U	unsharpness or resolution
W	inverse magnification
$\boldsymbol{x}$	image vector
X	crosstalk fraction
x, y, z	spatial coordinates, for resolution calculation: x is source size to detector size ratio

Greek letters

α	void fraction, for scattering interactions: mass ratio of target and incident particle
σ	microscopic neutron cross section, for error analysis it represents the error
Σ	Macroscopic neutron cross section
θ	angle
δ	delta function
μ	attenuation coefficient
ρ	density
ϵ	efficiency

Subscripts

0	Flat field
avg	average
d	detector
el	elastic neutron scattering
f	fission reaction
f	liquid
$inel$	inelastic scattering
phi	two-phase
rc	radiative capture
RMS	root mean square
s	spot
T	transmitted
$theta$	angular dependence
tot	total
v	vapour

Abbreviations

ASIC	Application Specific Integrated Circuit
BWR	Boiling Water Reactor
CANDU	CANadian Deuterium Uranium reactor
CFD	Computational Fluid Dynamics
CHF	Critical Heat Flux
CNN	Convolutional Neural Network
CT	Computed Tompgraphy
D-D	deuterium-deuterium reaction
DO	Dryout
DRA	Double Ring Assembly
D-T	deuterium-tritium reaction

ESF	edge-spread function
FBP	Filtered Back-Projection
FNCTS	Fast Neutron Computed Tomography System
FPGA	Field Programmable Gate Array
GCT	Gamma-ray Computed Tomography
GUI	Graphical User Interface
ML	Machine Learning
NEA	Nuclear Energy Agency
NRC	Nuclear Regulatory Commission
OECD	Organisation for Economic Co-operation and Development
PLA	PolyLactic Acid
PSF	point-spread function
PWR	Pressurized Water Reactor
SA	Suspension Assembly
SiPM	Silicon PhotoMultiplier
VIPS	Very Intense Point Source
WMS	Wire Mesh Sensor
XCT	X-ray Computed Tomography

Declaration of Academic Achievement

The contribution of this work was accomplished by the author with assistance from the committee and an undergraduate research assistant.

The design and assembly of the gantry used in the imaging system was done by P. Pastolero as part of an undergraduate research position under the author's supervision. Preliminary design was done by J. Goguen.

The supervisory committee members, Dr. D. R. Novog, Dr. J-M Le Corre, Dr. L. K. Leung, and Dr. J. S. Cotton provided technical feedback for the project and editorial feedback for this document.

The design, simulation, modeling, and construction of the benchtop experimental imaging facility and all synthesis of the results were performed entirely by the author.

1 Background

You keep on learning and learning,
and pretty soon you learn
something no one has learned before.

Richard Feynman

1.1 Overview

This thesis presents the development of a portable fast neutron computed tomography (FNCT) imaging system for the measurement of time-averaged void fraction distributions in high-temperature and pressure multiphase flows within complex nuclear fuel bundle geometries. Specifically, the objective for developing the system is to measure phase distributions at/near critical heat flux (CHF) conditions in fuel bundle geometries to provide much-needed data in the field of thermalhydraulic analysis and code validation.

The motivation for this work is to improve the predictive capabilities of thermalhydraulics codes. Specifically, there is a large body of evidence in industry that while the predictions of dryout are acceptably accurate at or near the nominal conditions of a fuel bundle in a CANDU reactor, the codes' ability to accurately predict the impact of some geometrical variations (e.g., pressure tube creep or pin diameter changes) requires improvement. While a majority of the evidence supporting this motivation is contained in confidential sources, open tests results such as BFBT and PSBT (discussed later in this thesis) support the need for better measurements. A key step in improving these codes would be better measurements of the void distribution at relevant conditions.

In this thesis, models and methods were developed to assess the FNCT system capabilities, including the impact of the dominant noise sources on the reconstruction quality and void fraction prediction. Void fraction prediction simulations of the McMaster FNCT system show that a minimum scan time of ~ 7.5 minutes can be achieved. The simulations were also used to derive an in-situ measurement technique to ensure that a void underprediction bias that was prevalent at low per-projection scan times can be avoided.

Benchtop tests were done at two facilities – McMaster and Ontario Tech – to generate data to validate the models and quantify the system performance. The McMaster system resolution was measured and agreed with the expected resolution and the final system is therefore estimated to have a resolution of ~1.7 mm to 1.9 mm.

A machine learning model was trained using simulated phantoms that applied the noise models developed in this thesis. The trained machine learning model was applied to measured images with significant noise and provided remarkable improvement. While the full system could not be tested due to a catastrophic neutron generator failure, the final system analysis using the models developed in this thesis shows very promising performance.

This chapter provides the background information relevant to this study. The following chapters are organized as follows:

Literature review and motivation: an outline of existing technique for void fraction measurements with highlight of benefits and need for the study.

Neutron tomographic imaging: the necessary background for neutron imaging and an outline of the equipment requirements.

<u>Simulation and system qualification/quantification</u>: the simulations of the performance of the proposed system design and the resolution and capability of void fraction prediction.

<u>System and experimental apparatus design</u>: description of the equipment used in the final design and benchtop testing.

<u>Experimental measurements</u>: presentation of data obtained from the imaging system and quantification of the void fraction prediction accuracy and resolution of the system.

<u>Conclusions and future work</u>: a summary and the necessary next steps for the fast neutron imaging system.

1.2 Nuclear power

Nuclear power provides around 10% of the world's [1] and about 15% of Canada's [2] electricity and represents one of the non-carbon emitting power sources available to help in solving the climate crisis. There are many reactor types: the boiling water reactor (BWR), pressurized water reactor (PWR), and pressurized heavy water reactor (PHWR), for example. To operate a reactor safely and maintain fuel integrity, the heat transport system must maintain efficient heat transfer from the fuel to the coolant. Power limits are imposed on a per-channel and per-bundle level to ensure adequate cooling of the fuel. The power limits imposed on the fuel bundle are based on a phenomenon referred to as the critical heat flux (CHF), which is the heat transfer limit where the liquid coolant ceases to contact the fuel sheath and thereby reduces the rate of heat-transfer from fuel to coolant. This is referred to as departure from nucleate boiling (DNB) in the case of PWR, or dryout (DO) in the case of the BWR and PHWR. The CHF condition is characterized by a sharp increase in sheath temperature with a small increase in heat flux (Figure 1.2.1 depicts an example of the large temperature increase of the sheath wall). The large increase in fuel sheath temperature can cause the sheath and fuel to fail, compromising the fuel integrity.

Such data is collected at full-scale thermalhydraulic test facilities, such as Stern Laboratories [3], using electrical heaters to simulate fuel heating in bundles. The data obtained from these experiments are used to develop correlations or create models which are used in computer codes to predict safety limits, such as CHF. To assess the progression and location of the CHF condition in a bundle geometry, computer code models must implement the correct flow and heat transfer physics. An important parameter for determining the two-phase flow and heat transfer physics within a bundle geometry is the void fraction.

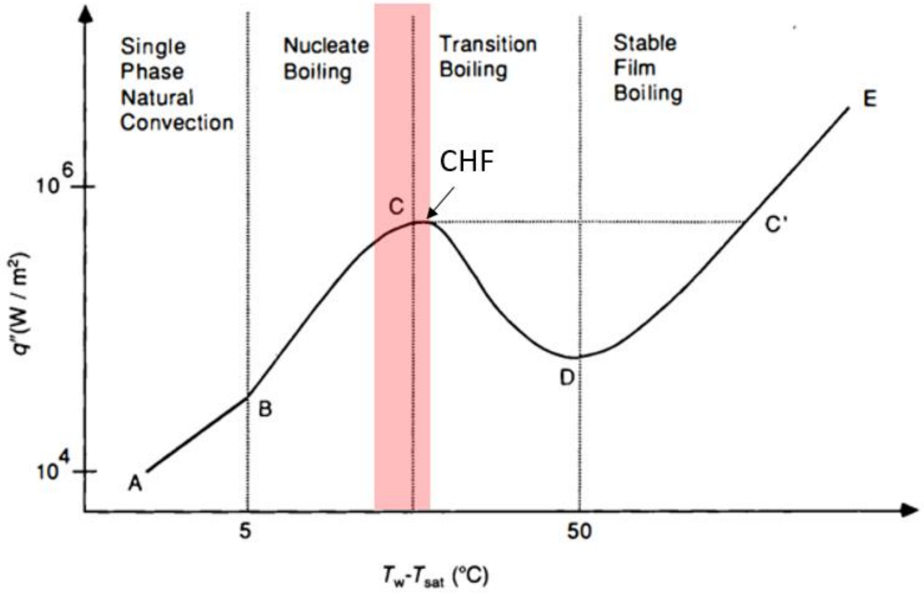

Figure 1.2.1: Pool boiling curve. Reprinted from Todreas and Kazimi [4]**. Note the large temperature excursions from the CHF point, C, to C'.**

1.3 Void fraction

The phases in the boiling process are distributed throughout a geometry depending on many factors such as flow rates, pressure, and how much of the vapour phase has been generated. The volume fraction of vapour is known as the *void fraction* and it is an important two-phase flow parameter as it affects neutron moderation, pressure drop, heat transfer, and flow distribution. The void fraction can be represented in different geometrical ways:

- Local: point-wise volume or area taken up by the vapour phase. For example, a pixel-wise computed tomography approach where void fraction is a measure of the amount of void within an individual point volume (in this example it would be a pixel).
- Linear: fraction of a line section through a domain that intersects the vapour phase. Such is the method used in radiation transmission methods including densitometry.
- Cross-sectional: fraction of the total area taken up by the vapour phase. This is used when calculating the subchannel void fraction average for example, or when using multi-beam densitometry.
- Volumetric: fraction of a volume taken up by the vapour phase. A simple example is using a quick-closing valve method on two ends of a test section length to capture the liquid-vapour mixture in a given volume. The void fraction is determined through geometry and mass.

If the instantaneous value of the void fraction is averaged over a period time, a time averaged void fraction is realized. This time averaging approach assumes that the effect of averaging is linear (e.g., adding up the residence time intervals of the vapour phase and dividing it by the total time interval). However in non-linear measurement processes such as radiation imaging or densitometry, the time averaging of fluctuating void fraction can give rise to a systematic error known as dynamic bias if the averaging time is greater than the void fluctuation time [5]. The effect of dynamic bias will be described in more detail later.

In a heated system, the void fraction will increase in the direction of flow which will change the distribution of phases, and hence the flow regime. As the vapour distribution changes with increasing void fraction, the characteristics of heat transfer will change and will ultimately determines how efficient the heat transfer process is. In Figure 1.3.1 it is apparent that if the amount of vapour in a geometry becomes too high the liquid may not be able to contact the surface (as seen in the transition from annular flow to drop flow), causing the temperature of wall to increase dramatically, which is the condition of CHF (dryout in this instance) described earlier.

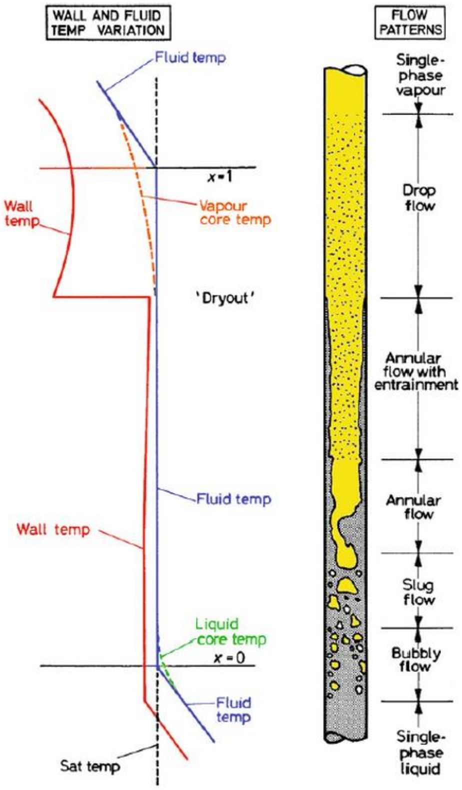

Figure 1.3.1: depiction of flow regime changes with axial position. The dryout point is indicated on the left plot of temperature. Reprinted from [6]

Bundle geometries, such as CANDU (Figure 1.3.2), are much more complex than a simple tube, with a combination of complex fixtures such as endplates, spacers and bearing pads, that disturb the flow. Each internal flow path within the bundle, called a subchannel (Figure 1.3.3), are similarly complex, with differently sized flow geometries that contribute to complex void migration phenomena, such as void drift, where the void tends to gravitate toward the more open channels [7], in addition to the existing flow turbulence and buoyancy induced void mixing effects between subchannels. Different power generation in fuel rods further complicate the physics by introducing enthalpy imbalances, causing different void generation rates in the subchannels [8].

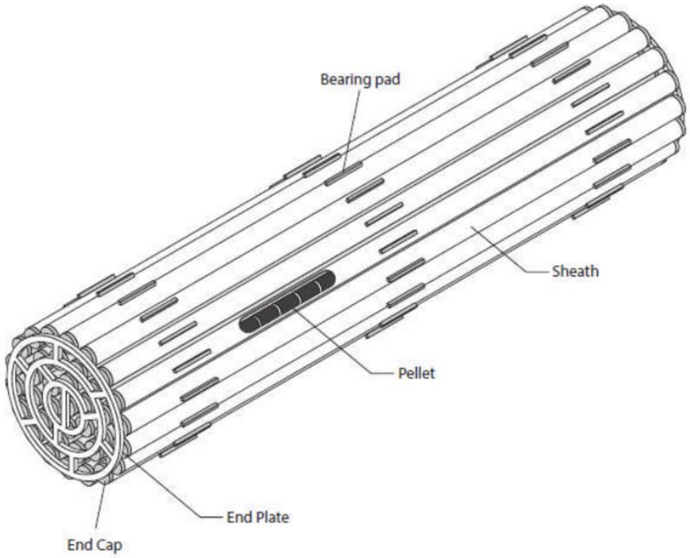

Figure 1.3.2: example CANDU fuel bundle. Reprinted from [9]

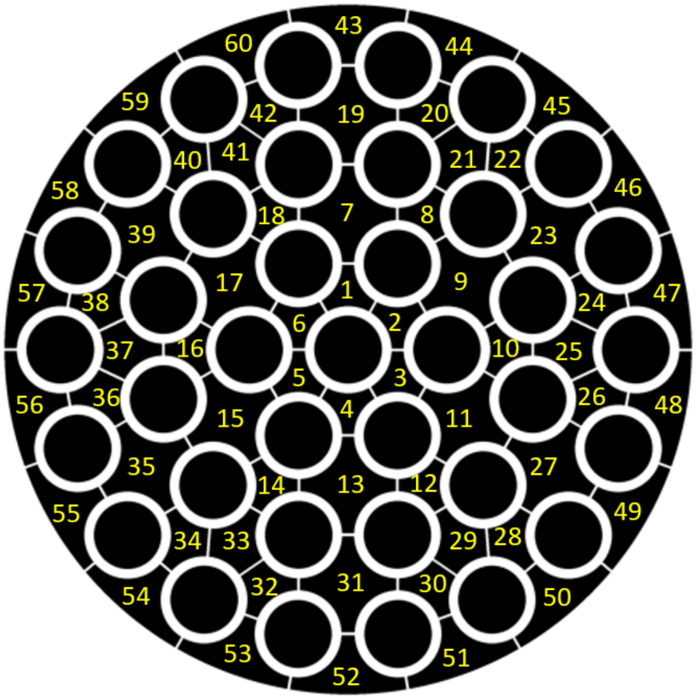

Figure 1.3.3: subchannel outline of the CANDU bundle.

1.4 Importance of void measurement

Due to the complex physics involved in two-phase flows in bundle geometries, empirical correlations are typically used to predict the CHF based on macroscopic parameters (P, G, x for example); however, these are subject to the specific conditions and geometries under which they were developed. The correlations are developed either through separate effects testing, with small tube geometries under different pressure and/or fluid conditions, specific full-scale testing, which is costly and not transferrable to other bundle designs outside of that experiment, or correction factors for existing correlations for simpler geometries, such as tubes.

Conditions within bundle geometries are complex to model and the prediction of the magnitude and location of CHF using subchannel codes is dependent on the accurate modelling of the flow and heat transfer physics within each subchannel.

The CHF is determined using correlations that are only applicable to the geometry and conditions that were used in the development. However, since bundle designs can vary significantly, enhanced knowledge of the flow physics (void migration, flow distribution) is imperative to understanding and developing more accurate models to better predict such parameters as CHF. The difficulty of CHF location prediction is exemplified in the BFBT [10] and PSBT [11] benchmark studies where the prediction of CHF location by computer codes was quite poor. Computer code models require detailed validation data to ensure proper modelling of the complex flow and heat transfer physics within bundle geometries, and thus improve their prediction accuracy. The difficulty in this validation is that the detailed phenomena in the interior of the bundle are difficult to measure. The vapour phase distribution (void fraction) within a bundle determines the subchannel flow distribution and therefore the flow regimes, which have a direct impact on the heat transfer characteristics within each subchannel. The onset and location of CHF in fuel bundle geometries is strongly dependent on the flow distribution, which is dependent on the void fraction distribution. Therefore, measurements of void fraction distribution within a bundle are fundamental for the validation and improvement of two-phase flow and heat transfer models implemented in subchannel codes, and for improved prediction of the location of CHF within bundle geometries.

A major impediment to these efforts is the lack of two-phase void fraction distribution measurements, especially near the CHF location, as the typical CHF measurement techniques employed in full-scale experiments only involve local wall temperature measurements and, at best, intrusive point measurement at select locations within the complex bundle geometry or full cross-sectional averaged void fraction. New measurement techniques capable of measuring void fraction distribution at full-scale test facilities are therefore needed to provide the required data. Such measurement techniques provide valuable information for the improvements in modelling, understanding, and prediction of full-scale two-phase flow phenomena. Many techniques for measuring the void fraction distribution have been used over decades and these are discussed in the next section. Afterward the motivation for the study will be outlined.

2 Literature Review

> *The only difference between screwing around and science is writing it down.*
> Adam Savage

For void fraction measurement instrumentation there are certain circumstances and desired parameters – whether it be cost, size, availability, or accuracy – that will promote one method over another. Therefore, several measurement techniques have been employed to provide better two-phase validation data for computer codes and phenomenological modelling under different conditions and with different geometries. The timeline presented at the end of this section in Table 1 indicates that until the mid-to-late 1980's, differential pressure sensors and optical methods were typically used to characterize the two-phase flow in bundles. More advanced techniques, such as X-ray, gamma-ray, and neutron measurements techniques were used largely during the 1990's with the wire-mesh sensor and conductivity probes becoming more prominent in bundle measurements in the mid 2000's. Contemporary measurement techniques contain a broad mix of these devices, however the majority of use cases are with air-water systems. This section will highlight some important measurement systems, and review their applicability, followed by an overview of the motivation for this thesis. The section concludes with a summary table at the end of the section providing a comprehensive list of bundle void fraction measurement systems used throughout the decades.

2.1 Point-based measurements

Intrusive methods such as optical and conductivity point probes and wire mesh sensors have been applied in many bundle measurement systems. Point-based methods take advantage of the property differences between fluids: optical properties, in the case of the optical point probe, and dielectric properties in the case of conductivity probes and WMS. Such point-based methods have been applied in several low-pressure gas-liquid systems, refrigerant systems, as well as in high temperature and pressure systems to obtain time-resolved point void fractions and bubble distribution and velocity measurements.

Since the point probes are limited to measuring single points within a subchannel, some point probe applications to bundle designs have implemented traverse systems (e.g., linear translation stages) to scan across specific cross sections of the bundle geometry to measure more pointwise data and therefore collect more void fraction information. For example, traversable conductivity probes inserted from the side of a bundle have been used to gather information on the void fraction profile within and between subchannels in various BWR bundle configurations [12]–[14] as well as study the effect of spacer grids on void distribution and bubble break-up [15]. Optical probe traversal systems were applied in a similar fashion [16], [17]. Methods inserted probes in the top of an open channel to provide more room for traversal system equipment in order to sample a greater number of points within a subchannel [18]. Such traversal systems are usually limited to low-pressure air-water systems, due to the necessity of protruding and traversal through the high-pressure flow boundary. There have been some notable applications of point probe void fraction measurement techniques to full-scale (or full-scale fluid-to-fluid scaled), although these are limited to three applications as described below.

The first example of a system using optical probes is the void fraction distribution measurements for a 37-element CANDU bundle [19] using refrigerant coolant at 1.5 MPa. A total of 23 stationary probes were placed in the center of various subchannels, with 3 probes that spanning a distance within the subchannel, along with one traversable probe that spanned the central vertical axis (Figure 2.1.1). The void fraction profiles were measured at different power fractions up to 80% of dryout power and showed the progression of void increase as the power is increased. Notably, corrections for the central void fraction readings to subchannel averages was necessary to obtain the subchannel void distribution since void fractions only at the center of each channel are gathered; using only the central point could overestimate void fraction if the void profile is peaked in the central core region of the subchannel, leading to a potential overestimation in the void fraction dataset if there is significant liquid film content that is not accounted for.

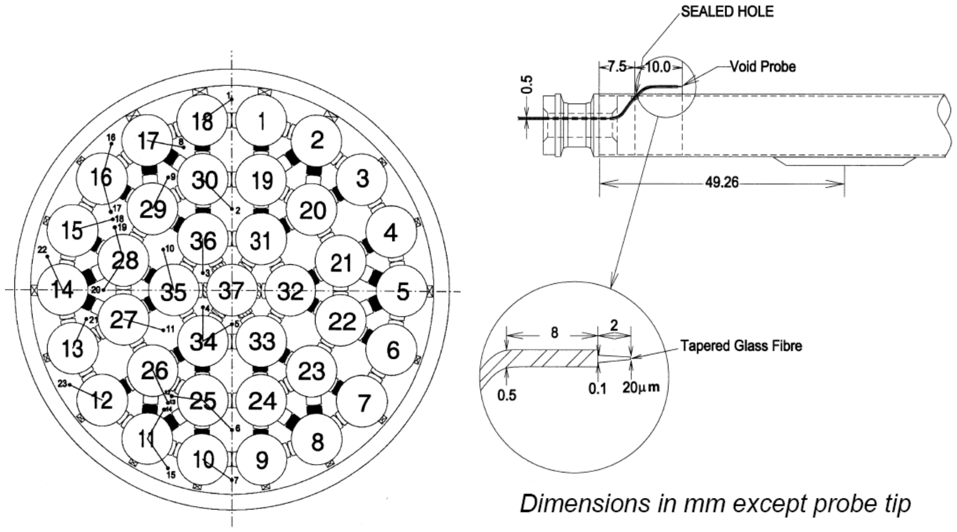

Dimensions in mm except probe tip

Figure 2.1.1: CANDU optical probe placement and installation. Reprinted from [19]

More recently, optical probe sensors and pitot tubes were installed at the end of heated length of a partial Triton11 bundle at the Westinghouse FRIGG facility under BWR operating conditions to validate the VIPRE-W void drift model [20]. The probes were placed in different subchannels to assess the void drift phenomenon, with one located in an open channel above a part-length rod, and the other located in a central, closed channel (Figure 2.1.2). Void and velocity data for these subchannels were collected over a range of power conditions that spanned from normal operation up until critical power. The measurements showed that the void in the open region above the part-length rod was greater than the closed central channel, even though the open region had a much lower power-to-flow ratio thus confirming a strong void drift phenomenon.

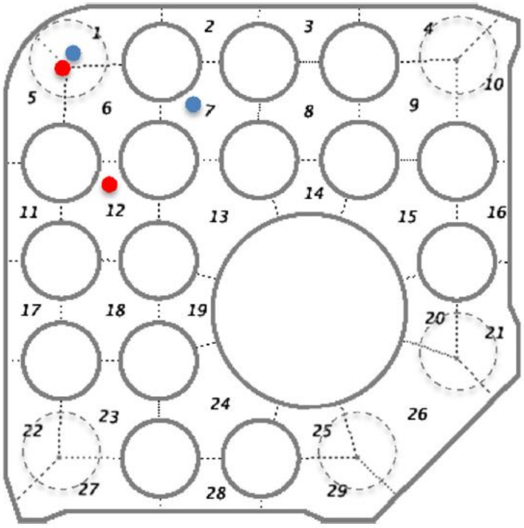

Figure 2.1.2: Frigg test facility (red: Optical probes, blue: pitot tubes). Reprinted from [20]

The same optical probe and pitot tube method was used in a full Triton11 bundle at the Westinghouse FRIGG facility under BWR operating conditions to measure local two-phase parameters and the structure of two-phase flow [21]. Measurements indicated differences between the flow regimes of high-pressure steam water flow and typical air-water flow. The high-pressure steam-water tests did not possess the same sharp flow regime transition traits that air-water flow studies have shown, and instead had a more gradual transition between the bubbly and annular flow regimes. The differences in flow regime transition highlight a potential limitation of air-water models to high-pressure boiling systems [21].

The Wire Mesh Sensor (WMS) captures point measurements across an entire cross-section without the need of a probe traverse system. The contemporary conductivity WMS for two-phase flow measurement was first developed by Prasser et al. [22], based on a similar design [23]. A full outline and explanation of the WMS operation principle have been described [22], [24] or [25].

The WMS was first applied to a bundle geometry by Ylönen et al [26] to study the single-phase mixing characteristics within a 4x4 rod bundle and later extended to study the bubbly flow distribution and the effect of spacer grids on the void distribution [27]. Since the first application, similar systems have been developed for two-phase flow measurements in rod bundles. Liu et al. [28] designed a straightforward extension of the WMS implemented by Ylönen et al. [26], [27], but with a finer mesh spacing within subchannels. The void fraction was measured at various combinations of liquid and air flow rates to determine the void distribution. These measurements were used to develop a new void fraction correlation for rod bundles. The systems designed by Ylönen et al. [26] and Liu et al. [28] were limited to air-water as the working fluid combination for two-phase investigations, and thus the extension to full-scale bundles is not apparent based upon the issues mentioned by Pietruske and Prasser [29].

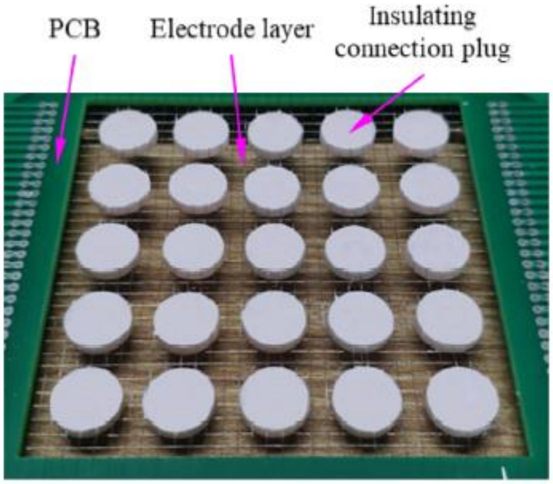

Figure 2.1.3: WMS for air-water bundle applications. Reprinted from Liu et al. [28]**.**

An interesting design is that of Arai et al. [30]: instead of using only a grid wire-mesh sensor the rods of the rod bundle were used as transmitters as well, called the subchannel void sensor (SCVS). This feature allowed the sensors to measure the void fraction near the wall of the rods, as well as in subchannel gaps effectively. The full working principle of this sensor can be found in [30]–[32] and an image of the system is shown in Figure 2.1.4. The first iteration of the design measured the air-water flow characteristics under the effect of spacer grids in a 10x10 rod bundle [30] and was later extended to low-pressure heated conditions [31].

The design by Arai et al. [30] was further improved to measure gas velocity and void fraction in a 5x5 square bundle design extending up to high temperature and pressure BWR operating conditions. The previous design [30], [31] was altered using the design outlined by Pietruske and Prasser [29]. The results were compared to CTF (COolant Boiling in Rod Arrays – Two Fluid) simulations of the geometry as well as to their previous X-ray measurements [33] taken of the same geometry and at the same conditions. However, the SCVS measurement provides a higher value of void fraction compared to the X-ray results above void fractions of 60%, which was attributed to liquid structures passing through the WMS without detection. The effect was also attributed to local transitions to annular flow, which present fine droplets that can go undetected. However, it may also be that by measuring only the center of the subchannel and only using specific points on the tube surface to represent whole fractions of the tube surface is not accounting for important phase content such as liquid film fluctuations in these regions. Nonetheless, the subchannel averaged void fraction results agreed with the X-ray data and CTF simulations to within 20%.

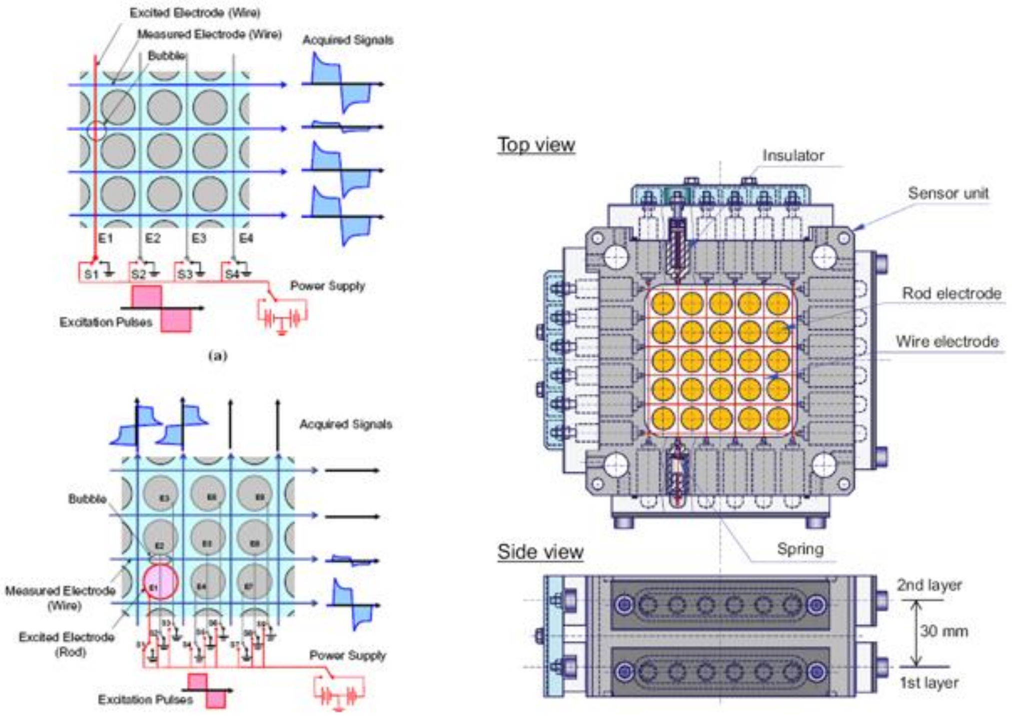

Figure 2.1.4: SCVS working principle (left) and the SCVS unit (right). Reprinted from Arai et al [30] **and Arai et al** [32] **respectively.**

The works using WMS indicated that the application to high pressure and temperature rod bundle geometry systems is possible and ongoing [32], and future research could provide some exciting developments and results given that it has only been just over a decade since the first application to rod bundle measurements.

Currently, however, the application to accident and safety conditions – where flow regimes such as annular flow are present – remain to be explored with this technology. This has been noted by [34] explaining that measurements for annular flow conditions are difficult to obtain, owing to the fact that the WMS pitch is required to be on the order of the smallest feature size (e.g., the liquid film thickness or droplet diameter). However the SCVS developed by [32] could provide a solution to this problem with their unique rod transmitter method.

A significant benefit of these intrusive methods is the ability to provide a broad number of two-phase flow characteristics, such as bubble dynamics and size as well as void fraction, which are useful in validating computational fluid dynamics (CFD), three-field, two equation, and drift flux models. However, point-based sensors can only be applied at specific axial locations within the geometry and are intrusive to the flow field. There are some notable techniques that have used conductivity sensors attached to bundle rods to measure void fraction distributions [35] or liquid film thicknesses [36] that reduce the intrusiveness of the measurement technique, albeit only for air-water flows. The most recent high-pressure and temperature probe-based bundle implementation used stationary optical probes to successfully gather subchannel void information [20]. However, a direct comparison of the results to the code-predicted subchannel average was not possible, and some approximations were made to convert the code subchannel average to a central core void fraction. To obtain a direct comparison in such circumstances, multiple probe locations or traversal methods can be used, however these methods become prohibitively expensive and are significantly more complex at high pressures and temperatures. The SCVS of Arai et al. [32] showed a promising approach at these conditions as well, but the current results indicate the measurements overestimate at high void fractions, which may be due to the inaccuracies caused by annular flow characteristics.

2.2 Radiation-based measurement

Non-intrusive techniques using radiation-based methods such as gamma-ray densitometry and X-ray (XCT), gamma-ray (GCT) and neutron (NT) tomography have all been used to gather multi-phase flow data. Radiation-based methods provide a non-intrusive way of measuring two-phase flows within rod bundle geometries. The method works by measuring the amount of attenuation due to an object in between the source and detector and uses that information to infer the distribution of phases within an object. Traditionally X- and gamma-rays have been used in portable systems, but more recently neutrons have also become an enticing option for portable imaging systems.

2.2.1 Photon-based sources

X-ray systems were first applied in medicine in 1973 and have since been applied to various industrial two-phase flow imaging campaigns, including rod bundle measurements. Such industrial systems often focus on time-averaged void fraction distribution measurement. The earliest industrial XCT system applied to rod bundles was that of Mitsutake et al. and Morooka et al. [37], [38] in which the time-averaged void distribution within a 4x4 BWR partial lattice (at a pressure of 1 MPa) was measured. The system used a translate-rotate tomography system to measure the void fraction distribution and measured the side, corner, and central sub channel void fractions specifically. These authors showed that the central subchannels tended to have a higher void fraction than the side or corner subchannels, which is evidence of the void drift phenomenon described by Lahey et al. [7].

The system was later updated to a fan-beam configuration (Figure 2.2.1) and used to verify void fraction prediction methods for a 8x8 BWR partial lattice at pressures up to 7.2 MPa [39]. This new test campaign added unheated rods in the central region of the bundle (up to 3x3 unheated rods) to explore the effect on the void distribution and provide void fraction data to quantify the prediction accuracy of subchannel codes at the time. An interesting phenomenon was measured in their 2 unheated central rods case: the central region containing the 2 unheated rods had a lower power density but tended to have a higher void fraction than the adjacent region with a higher power density [39]. The results generated in this campaign provided the foundation for the OECD/NEA BFBT benchmark a decade later [10].

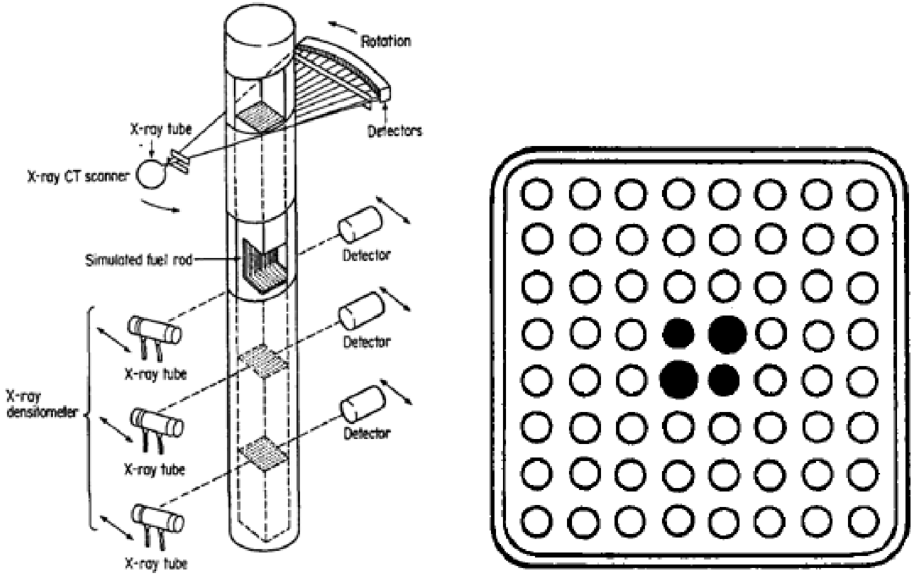

Figure 2.2.1: XCT scanner for BWR void distribution measurement (left) and example bundle with unheated rods in black (right). Reprinted from Inoue et al. [39]**.**

Since that time, system developments would focus on improving the framerate of acquisition to accurately measure transient two-phase flow phenomena and provide more time-resolved measurements of two-phase flows. Hori et al. [40] developed a system using 60 X-ray sources (Figure 2.2.2), improved from their previous 18 X-ray source system [41], to measure the time-resolved void distribution of air-water flow through a 3x3 PWR lattice with and without spacer vanes [42]. The system improved the acquisition rate to 2000 fps by actuating each source in series, meaning that many angles could be acquired without translating bulky equipment.

This was the fastest scanner at the time, and as of this writing the system has not been used for further bundle measurements; however, a similar conceptual design to the 18 source system [41] was used and compared to WMS two-phase flow data for a simple tube geometry [43].

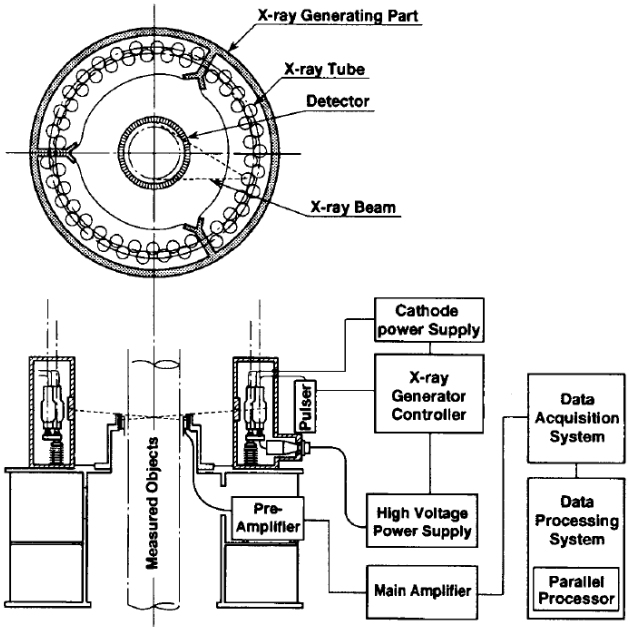

Figure 2.2.2: Fast scanning XCT system using multiple X-ray sources. Reprinted from Hori et al. [42]

Contemporary efforts to improve the temporal resolution have opted to use different X-ray source strategies. A fast electron beam scanner was developed by [44] using a linear scanning technique to obtain images of phantoms at a reduced number of viewing angles and a framerate of up to 2500 fps [45]–[47]. The system was later used to compare measurements of a WMS [47], although the XCT system was not capable at imaging at the same speeds as the WMS, which limits the velocities and transient phenomena that can be measured with such a system.

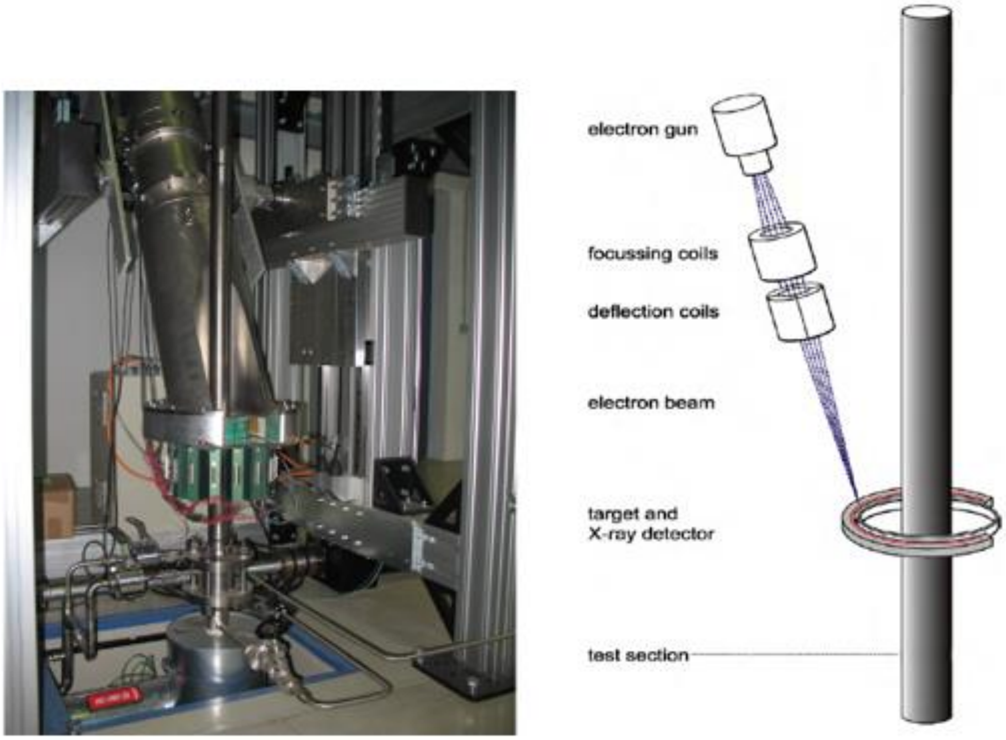

Figure 2.2.3: Ultra-fast XCT scanner beam scanning method. Reprinted from Fischer et al. [48]**.**

The electron beam scanning concept was further developed to image even faster than the linear beam scanning method. Using a similar fast electron beam scanning technique, [49] were able to obtain 8000 fps scans by scanning the electron beam in a horseshoe trajectory around a small test section (Figure 2.2.3). The system has been used to measure void structures in various air-water flow campaigns [49], [50] and velocity by implementing a dual plane system [51]. Although the scanner is not planned for use on bundle tests and has not been used in full-scale testing, it represents the current state-of the art in terms of tomographic scan times.

Contemporary bundle and subchannel measurement XCT systems have focussed largely on implementing similar systems to Inoue et al. [39] with updated detector and source technology; for example a 3D XCT scanner was developed to measure the air-water flow in a 5x5 bundle [52], [53]. An XCT system was implemented to study the liquid film distribution in a single-subchannel geometry using chloroform as the coolant (to increase attenuation, and hence contrast, of the fluid) [54]–[56] and extended this to study the film distribution before and after dryout conditions [56]. The system implemented by Arai et al. [33], [57] represents the only contemporary XCT system applied to high-pressure bundle void fraction measurements.

The high spatial and temporal resolution capabilities of X-ray void imaging systems make them an enticing option for two-phase flow imaging. Furthermore, XCT systems represent the only transmission CT imaging modality with temporal resolutions that can capture transient two-phase flow features [49]. However, extending the use of X-rays to nuclear assembly integral testing is challenging due to the large amount of high Z materials (i.e., metals) used as pressure boundaries and heater rods. Materials such as titanium are often used to reduce the thickness of the pressure boundary, which increases the cost of the test section. The lack of contemporary published work for high-pressure and temperature bundle measurements highlights the difficulty in applying XCT at such conditions, with the exception being the study presented by Arai et al., although the measurements were limited to heat fluxes far below CHF [33], [57]. The most successful XCT bundle measurement data continue to be the 1995 measurement campaign of Inoue et al. [39] which were used as part of the OECD/NEA BFBT benchmark [10] and continue to be used to benchmark subchannel analysis codes [20], [58].

Gamma-ray imaging systems are much like X-ray systems in that they use photon sources. However, gamma-ray sources often provide higher energy radiation and thus have increased penetration power for the same materials as compared to X-rays[1]. Additionally, gamma-ray sources can be made small by using sources with high-specific activity providing moderate gamma-ray fluence rates (albeit lower

---

[1] This is *usually* true, since most gamma-ray sources used in imaging are much higher energy than X-ray sources, such as a Cs-137 source, for example.

than their X-ray counterpart, in general). As such gamma-ray systems have provided a suitable method of multi-phase flow measurement for decades, since the source sizes can be made small, and provide moderate radiation penetration power and radiation output. In fact, gamma-ray measurements have been used in rod bundle studies as early as the late 1960's when Nylund et al. applied gamma ray densitometry to develop a radial void fraction map of a 36 pin fuel bundle geometry [59]. The applications of gamma-ray systems after that time were largely applied in simple densitometry and CT systems for small-scale geometries up until the early 1990's.

In the early 1990's, a GCT system was developed by Hori et al. to measure single PWR subchannel geometries [60]–[62] and apply the measurements to an experimental study of a high temperature and pressure PWR 5x5 bundle array under steady-state and transient conditions. The end application of the CT measurements is unique when compared to traditional bundle void distribution measurement methods. To obtain the bundle void fraction only two views were used (Figure 2.2.5), allowing the measurement technique to be used in transient scenarios. Detailed subchannel void fraction information was supplemented using CT measurements for individual separate effects tests of different subchannel geometries [60], [61]. From these measurements, a correlation of densitometry measurements of the individual subchannel to the cross-sectional void fraction was obtained [62]. The data obtained from this unique system was used as a foundation over a decade later as part of the OECD/NRC PSBT benchmark [63].

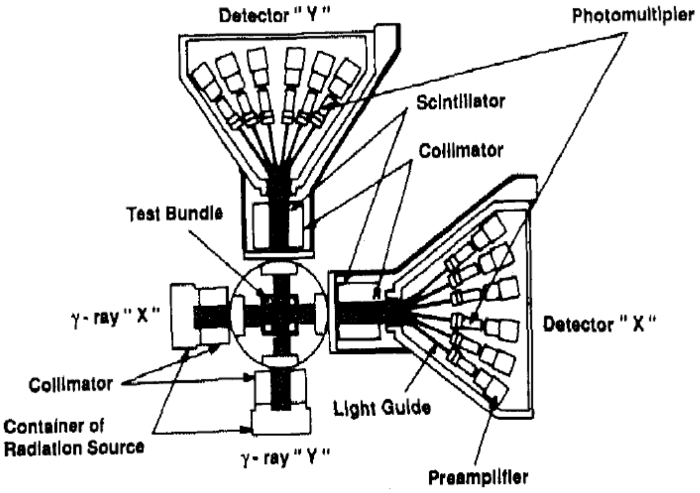

Figure 2.2.4: Gamma densitometer bundle void fraction measurement system. Reprinted from Hori et al. [60]**.**

A more traditional tomographic scanner for BWR partial bundle measurements was used by Windecker and Anglart [64]. The system was used to measure the void fraction of a heated 5x5 BWR lattice and determined a dependence of the spatial distribution of phases in a subchannel on pin power fraction. The subchannel average phase distribution showed differences in the distribution based upon pin power fractions and were in good agreement with their two-phase CFD simulation results. This system has not been used recently, but efforts have been made to update the post-processing of the data to obtain better image quality and analysis through new methods of image reconstruction [65].

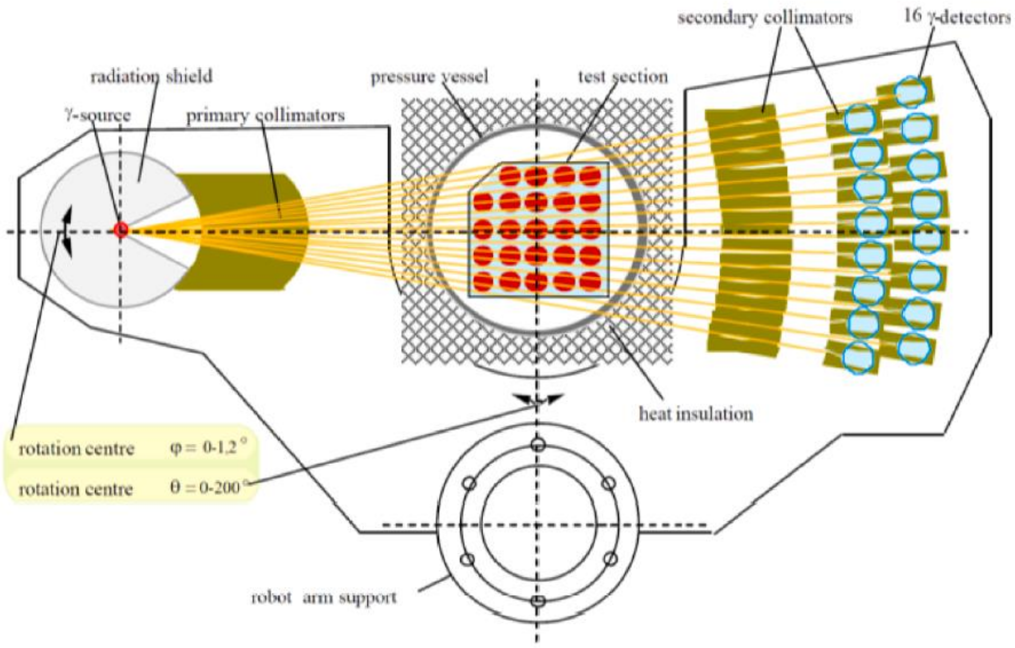

Figure 2.2.5: Gamma-ray CT measurement system for BWR void fraction distribution measurement. Reprinted from Le Corre [65]**.**

Contemporary GCT systems have largely adopted the standard fan-beam CT system layout over the more unique method of Hori et al. [60]. The improvements focussed largely on obtaining finer resolutions through the use of updated detector technologies such as SiPMs and APDs [66]–[68]. Bieberle et al. [66] implemented a similar system design to [64] with updated APD detector technology. Although the goal of the system was the measurement of two-phase flow bundle studies, only the stagnant density distribution in a BWR lattice structure with water and other fluids such as hexane have been done [66].

Adams et al. developed a compact system using SiPM detectors [67]. This has the highest spatial accuracy currently for any current industrial gamma imaging system at 1 mm or less, owing to the small radiation emitting spot size and detector pixel size. The system has been tested on phantom geometries to determine system resolution as well as simulated small-scale rod bundle structures with plastic simulating water [69], [70]. The system has not yet been applied to full-scale tests, although the system is slated to be used in air-water flow visualization tests in the near future (~2023) [71].

Gamma-ray imaging techniques provide higher penetrating power but suffer from other inconveniences. For example, gamma-ray sources require higher shielding requirements than X-ray systems as they do not have the flexibility of controlled emission. Additionally, the imaging technique suffers from reduced phase contrast as the energy of the source increases, i.e., the water attenuation coefficient decreases monotonically with gamma-ray energy which causes decreased sensitivity to water content as source energy increases. This effect is exemplified by Adams et al. where they compared the contrast of gamma-ray and fast-neutron acquired images [72]. The most successful gamma-ray based bundle measurement data is from the 1990's campaign of Akiyama et al. [60]–[62] which provided the data for the OECD/NRC PSBT benchmark [63]. The data has also been used in more recent studies to benchmark subchannel analysis codes [73].

2.2.2 Neutron imaging systems

Neutron radiation has low interaction probability with metallic materials, providing a good option for imaging through thick metallic pressure boundaries, while having a large sensitivity to hydrogenous materials such as water. The energy of the neutron radiation has a large impact on the applicability of a measurement system to a given geometry and these neutron energies are broadly divided into three categories for imaging: thermal, cold, and fast neutrons.

Thermal neutron imaging has been used extensively in two-phase flow imaging due to its interaction efficiency with water. This interaction efficiency allows for high-resolution measurements of small liquid structures such as liquid films, which exist at conditions of dryout, making it an ideal candidate for a non-intrusive high resolution measurement system. There have been many void fraction measurement studies for simple geometries [74]–[77], and the application has extended to bundle geometries as well.

Thermal neutron radiography measurements with air-water fluid have been made by Lim et al. [78] for axial void fraction measurements and by Harvel et al. [79] to visualize stratified waves in a CANDU bundle geometry. Takenaka et al. used radiography and tomography methods for fuel bundle void measurements [80], [81]. A detailed application of thermal neutron tomography for bundle void fraction measurement is the collection of work by Kureta et al. [82]–[84]. In the work, they successfully performed detailed 3D thermal neutron computed tomography measurements and examined 3D void distribution in advanced BWR tight-lattice bundle designs for advanced BWR applications.

Cold neutrons provide even higher sensitivity to liquid films due to their lower energies and have been particularly useful in this field of measurement. Zboray et al. has demonstrated high fidelity measurements of the liquid film thickness in single and double subchannel geometries [85]–[88]. Their measurements explored the effect of spacer geometries on the redistribution of the liquid film pre- and post-spacer grid. Although the information does not report on the void fraction directly, the cold neutron tomography system is able to provide valuable information on spacer grid influence on flow redistribution of the liquid film. Such information is instrumental to inform CFD as well as phenomenological models toward the improvement of our mechanistic understanding.

Cold and thermal neutron systems have the potential to provide highly detailed phase distribution information (down to the micrometer level). However, the primary difficulties in applying thermal and cold neutron tomography to full-scale bundle testing are:

- the necessity of rotating the test section when using reactor or spallation sources.

- Applying full-scale testing at beamlines, due to the inability to install the permanent power supply infrastructure around the beamlines.
- Using portable sources require moderation which removes too many neutrons due to thermalization and collimation to be practically useful.

This is a consequence of requiring access to excessively large neutron sources, such as research reactors or spallation beamlines, which immediately preclude their transport to existing industrial test facilities. There are methods of downsizing thermal neutron sources to make them more portable, as demonstrated in [89] using a high output D-D neutron generator, which are promising. However, such a system is still bulky and expensive and has yet to be applied in any two-phase flow research.

Fast neutron bundle measurement techniques have used reactor-based sources [80] for void distribution measurements and isotope-based sources for cross-sectional void fraction scatterometry measurements [90]. Although some early void measurement designs had proposed the use of monoenergetic, portable neutron generators in the 1980's [91] they were not implemented at the time, likely due to the size and cost of such specialized sources. However, portable neutron generators have recently emerged as a cost-effective, fast neutron source that provides benefits in terms of size and mobility, due in large part to United States homeland security applications.

Contemporary fast neutron imaging system development for bundle void fraction measurement is sparse and consists of two main development efforts. The first system is that of Andersson et al. using a DT neutron generator [92]–[94] which measured a symmetric tube with a plastic film. The second system is that of Adams et al. which used a DD neutron generator to measure several plastic test objects [72]. Although these systems demonstrated imaging resolution capabilities, the accuracy of the void fraction prediction has not been quantified; in addition, even with updated source technology such systems have typically required longer scan times compared to the reactor or spallation-based systems due to lower neutron output, with scans on the order of 4 hours due to the difficulty of detecting fast neutrons [72], [94].

To date, the only tested applications for fast neutron imaging of bundle void fraction have been:

- Buell et al. [90] using a Cf-252 source to perform scatterometry to obtain the transient cross sectional averaged void fraction in a test section channel.
- Takenaka et al. [80] using a reactor-based source to measure the void fraction distribution in a 4x4 bundle in air-water flow.

Notably, only the system used by Buell et al. [90] was portable enough to be transported to, and constructed at, the facility in which it was applied.

The pioneering work for portable FNCT techniques for void fraction measurement in past literature [72], [94], [95] are clear evidence of the potential of such systems. However, the systems were never applied, and the void fraction prediction accuracy was not quantified. The systems also required scan times on the order of 4 hours due to the difficulty of detecting fast neutrons. Such scan times are far greater than the allotted time for thermalhydraulic testing campaigns at a given condition, such as at or near CHF.

Given the recent increases in output of portable generators by several orders of magnitude in the past half-decade, these imaging times can be significantly reduced by increasing the neutron source output. A typical generator output in 2022 is on the order of 10^8-10^{10} n/s for a D-D source compared to the source output in 2015 when the maximum generator output was about 10^6-10^7 n/s [96]. Additionally, recent improvements in target design could increase the neutron output by another 4 times [97], thus reducing scan times even further.

2.3 Motivation

There is a clear need for void fraction information at full-scale conditions in rod bundle geometries for both code development and phenomenological understanding of flow distributions in complex bundle designs. This is highlighted by the fact that only datasets from almost 30 years ago [10], [63] are available for validation campaigns. If there is to be continued data collection to develop more accurate two-phase models and improve nuclear safety codes, updated tools that can measure phase distributions as well as two-phase phenomena around complex bundle geometry features at boiling conditions are required.

Void fraction distribution data are sorely lacking, especially for CANDU geometries. This fact is highlighted in a study by Abbasian et al. in which they used a CFD model to predict the void distribution in a channel with 37-element CANDU bundles [98] and noted that there was no void fraction data for comparison, and for a more accurate evaluation of their model void distribution data is needed.

Given that it is not feasible to build full-scale testing geometries and infrastructure for every single testing campaign a solution that can be transported and deployed at existing full-scale testing facilities without disruption is crucial. The intrusive techniques, such as probes and WMS, are precluded as they require that the geometry be altered (for each bundle design, if there are multiple). Photon-based, non-intrusive methods are affected by the presence of high-Z material present in full-scale experimental geometries, which reduces the contrast of the internal structures. Cold and thermal neutrons are precluded when large thicknesses of water are involved and obviously cannot be transported to existing facilities. Portable fast neutron sources are desirable since they can penetrate thick pressure boundaries and maintain sensitivity to the internal phase structure within the bundle geometry. The portable fast neutron source provides the flexibility to image bulky objects consisting of a wide range of materials and the ease of transport to measure on-site with no structural disruption.

This thesis presents the design, assembly, and evaluation of a new portable fast neutron computed tomography system that can provide this much-needed void fraction data. There are only two such efforts to develop such a system for two-phase flow measurements, and this system represents the first in Canada. The system design uses a modern fast-neutron D-D generator (capable of 10^8 - 10^9 n/s) with a spot size of ~2 mm, coupled with silicon photomultiplier (SiPM) detectors and plastic scintillators.

Table 1: Bundle void measurement literature.

Citation	**date**	**Reactor model**	**Working fluids**	**Pressure (MPa)**	**Rod diameter (mm)**	**Pitch (mm)**	**Arrangement**	**Method**
Nylund et al. [59]	1968	BHWR	steam-water	5	13.8	21-21.6	36	GD
Williams and Peterson [147]	1978	**	steam-water	2.76 - 13.8	6.35	8.64	1x4	VO
Venkateswararao et al. [148]	1982	PWR	air-water	0.101	12.7	17.5	24	DP
Anklam and Miller [149]	1983	PWR	steam-water	4 - 8.1	9.5 - 10.2	12.7	8x8	DP
Morooka et al (1989) **Mitsutake et al (1990)** [37], [38]	1989	BWR	steam-water	0.49, 0.98	12.3	16.2	4x4	XCT
Hori et al. [60]	1993	PWR	steam-water	4.9 - 16.6	9.6	12.6	single subchannel	GD, GCT
Kumumaru et al. [150]	1994	PWR	steam-water	3.0 - 12.0	9.5	12.6	24 heated 8 unheated rods	DP, GD, OP

Akiyama et al. [62]	1995	PWR	steam-water	4.9-16.6	**	**	5x5, single subchannel	GD, GCT, DP
Hori et al. [61]	1995	PWR	steam-water	4.9-16.6	9.5	12.6	single inner subchannel	GD, GCT
Inoue et al. [39]	1995	BWR	steam-water	7.2	12.3	16.2	8x8	XD, XCT, DP
Harvel et al. [79]	1999	CANDU	air-water	0.101	12.7	14.5 - 14.7	37	RTNR
Takenaka et al. [80], [151]	1999	**	air-water	0.101	10	13	4x4	TNCT, FNCT
Hori et al. [42]	2000	PWR	air-water	0.101	9.5	12.6	3x3	XCT
Kok et al. [152]	2001	BWR	freon	1.1	6.4	8.8	6x6	GCT
Windecker and Anglart [64]	2001	BWR	steam-water	7.0	9.6	12.7	24	GCT
Senaratne and Leung [19]	2005	CANDU	R-134a	1.5	12.7	14.5 - 14.7	37	OP
Buell et al. [90]	2005	CANDU	steam-water	10	7.62	14.45	7	FNS
Hampel et al. [68]	2007	BWR	air-water, silicone oil	0.101	10.0	13	10x10	GCT

Kureta [82], [83], [153]	2007	BWR	steam-water	0.101	12	13	7	TNCT
Yun et al. [12]	2008	BWR	steam-water	0.101	8.2	16.6	3x3	CP, HSC
Paranjape et al. [13]	2010	BWR	air-water	0.101	12.7	16.7	8x8	CP
Damsohn and Prasser [36]	2010	BWR	air-water	0.101	20.0	26.5	2x3	LF sensor
Bieberle et al. [66]	2011	BWR	air-water, hexane	0.101	10.0	13	10x10	GCT
Arai et al. [30]	2012	BWR	air-water	0.101	10.0	13	10x10	SCVS
Yang et al. [14]	2013	BWR	air-water	0.101	10.3	16.7	8x8	CP
Zboray and Prasser [87]	2013	BWR	air-water	0.101	20.0	26.5	2x3	CNCT
Arai et al. [31]	2014	BWR	steam-water	0.101	10.0	13	5x5	SCVS
Hosokawa et al. [18]	2014	BWR	air-water	0.101	10	12.5	4x4	CP, LDV
Andersson et al. [92]–[94]	2014	BWR	plastic-air	0.101	*	*	Tube	FNCT
Katono et al, Nukaga et al. [52], [53]	2015	BWR	air-water	0.101	10.3	13	5x5	XCT, WMS, DP
Adams et al. [72]	2016		plastic-air	0.101	*	*	Square block	FNCT

Ren et al. [15]	2018	BWR	air-water	0.101	9.5	12.6	5x5	CP
Arai et al. [33]	2019	BWR	steam-water	0.1-7.2	10.0	13	5x5	XR, XCT
Shen et al. [17]	2019	BWR	air-water	0.101	10.0	16.7	6x6	OP, DP
Han et al. [16]	2019	BWR	air-water	0.101	10.0	16.7	6x6	OP
Le Corre [20]	2019	BWR	steam-water	7.0	**	**	5x5 (Triton)	OP
Le Corre [21]	2020	BWR	steam-water	7.0	**	**	Triton11	OP
Chen et al. [35]	2020	BWR	air-water	0.101	11.5	15.4	3x3	Cond Sensor, HSC, DP
Adams et al. [69], [70]	2021	*	plastic-air	0.101	16	21.1	4x4	GCT
Zboray et al., Bolesch et al., Robers et al. [54]–[56]	2021	BWR	chloroform	0.115	10.3	13.4	Single central subchannel	XCT, CNCT
Arai et al. [32]	2022	BWR	steam-water	1-7.2	10.0	13	5x5	SCVS
Arai et al. [54]	2023	BWR	steam-water	7.2	10.0	13	5x5	SCVS

**: not given

*: not applicable

XD, XR, XCT	X-ray: Densitometry, Radiography, Computed Tomography
GD, GCT	Gamma-ray: Densitometry, Computed Tomography
RTNR, TNCT, CNCT, FNCT	Real Time Neutron Radiography, Thermal Neutron, Cold Neutron, Fast Neutron Computed Tomography
VO, HSC, DP	Visual Observation, High-Speed Camera, Differential Pressure
CP, OP	Conductivity Probe, Optical Probe
SCVS	SubChannel Void Sensor

3 Fast Neutron Computed Tomography

Insane theories, one;
regular theories, a billion.
Philip J. Fry

As outlined in the literature review, there is a strong need for void fraction distribution measurements in rod bundle geometries at operating conditions, particularly for CANDU geometries, for the validation and development of computer code models such as those in CFD and subchannel analysis codes. To that end, a portable fast neutron system is designed, developed, built, and tested. This section outlines the necessary background information for tomography that is required for the development of the fast neutron tomography system for use in void fraction imaging.

3.1 Neutron Computed Tomography

Radiation tomographic imaging is a completely non-intrusive measurement method useful in measuring the contents within complex geometries. Industrial imaging is performed using three different types of radiation:

X-rays: typically used when high energies are not necessary to penetrate thick pressure boundaries [49], or when purpose built test sections are built to reduce beam starvation [37].

Gamma-rays: used in cases where higher energies are required to penetrate thicker pressure boundaries than any X-rays can handle [60], [66].

Neutrons: useful for penetrating thick pressure boundaries, and can be used as cold [85], thermal [99], or fast [72] neutrons depending on the desired measurement.

The application of these radiation types will depend on the specific goals of the measurement. This thesis is primarily concerned with neutron systems, and thus this section will focus on the sources, interaction, and detection of neutron radiation. For information on other radiation sources, see [100]–[102].

3.1.1 Neutron interaction and attenuation

The strength of the reaction between a neutron and a nucleus is quantified using what is called microscopic nuclear cross-sections, represented by σ. This can be viewed as an effective cross-sectional area of a nucleus that the neutron interacts with [103]. The are several ways that a neutron can interact with the nuclei of atoms:

- **Elastic scatter (σ_{el}):** the neutron interacts with the nucleus of an atom, without absorption or excitation of the target nucleus. The neutron continues at a lower energy and altered direction. The target nucleus can also move after the collision with an energy equal to the difference in incident neutron energy and scattered neutron energy and is referred to as a recoil nucleus.

- **Radiative capture (σ_{rc}):** the neutron is absorbed by the nucleus, increases its energy level and becomes a new isotope. The excess energy of the new isotope is released as gamma-radiation.

- **Inelastic scatter (σ_{inel}):** the neutron collides with the nucleus of the atom and transfers some energy to the nucleus which leaves it in an excited state.

- **Fission ($\boldsymbol{\sigma_f}$):** a neutron collides with a nucleus and can cause the nucleus to split apart into fragments, releasing a large amount of energy in the process.
- Charged particle or neutron producing interactions: the neutron is absorbed by the nucleus and neutrons or charged particles are emitted based on the type of nucleus involved.

These cross-sections can be combined into the overall nuclear cross-section:

$$\sigma_{tot} = \sigma_{el} + \sigma_{inel} + \sigma_{rc} + \sum^{x} \sigma_x \qquad (3.1.1)$$

Where $\sum^{x} \sigma_x$ is the summation of other absorption cross sections. The total cross-section (σ_{tot}) can be summarized as a combination of total scattering (σ_s) and total absorption (σ_a) cross-sections:

$$\sigma_s = \sigma_{el} + \sigma_{inel}$$

$$\sigma_a = \sigma_{rc} + \sum^{x} \sigma_x$$

$$\sigma_{tot} = \sigma_s + \sigma_a$$

The interactions of interest for fast neutron imaging of objects are elastic and inelastic scattering. Elastic scatter reactions are the primary reaction type for fast neutrons for neutron energies below the first excited state of a given nucleus; above this energy, the nucleus can also undergo inelastic collisions. Inelastic collisions are important in scintillation counting as it will alter the analysis and output response of the detection system, as seen in the work of Andersson [94] where a high-energy D-T neutron source is used. In this thesis, a D-D generator is used, and thus inelastic collisions are not possible in the scintillator nuclei of H-1 and C-12 or in the representative phantoms, which are composed of metal, water, and plastics. The elastic collision physics in scintillators are discussed later in this section and the attenuation of neutrons within objects of interest is discussed here.

The attenuation measurement properties for a given material are a function of the attenuation coefficient and the path length of the radiation through the material. The attenuation coefficient in the case of neutrons is given by:

$$\Sigma_{\mathrm{tot}}(E) = N\sigma_{tot}(E) \tag{3.1.2}$$

Where $\Sigma_{\mathrm{tot}}(E)$ is the energy dependent macroscopic cross-section and N is the atomic density of the material. In the case of fast neutrons, the total cross-section is dominated by the elastic scattering component, such that

$$\Sigma_s(E) \cong \Sigma_{tot}(E)$$

The quantity of neutrons attenuated by a given material is given by the Beer-Lambert law (sometimes referred to as Beer's law or Lambert's law). The polyenergetic version of the law is given by:

$$I = \int_E I_0(E)\exp\left(-\int_{\boldsymbol{r}} \Sigma(x, y, E)ds\right)dE \tag{3.1.3}$$

Where I is the number of counts after attenuation, I_0 is the unattenuated incident radiation counts, ds is the differential length through the material, and E is the energy. Equation 3.1.3 outlines the dependence of the radiation attenuation on the spatial coordinates as well as energy. For the D-D neutron generator, which is monoenergetic, the energy dependence is removed, and the expression simplifies to:

$$I = I_0 \exp\left(-\int_0^d \Sigma(x,y)ds\right) \tag{3.1.4}$$

And represents the one-dimensional attenuation along a line through a given material, depicted in Figure 3.1.1. The expression of equation 3.1.4 is the foundation of tomographic imaging.

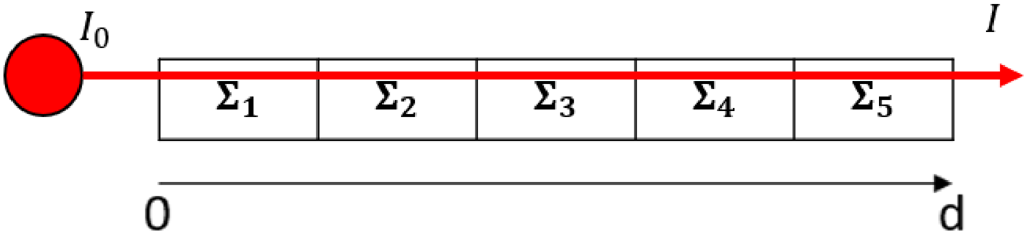

Figure 3.1.1: Radiation attenuation and spatial dependence of attenuation coefficient.

3.1.2 Tomography system geometries

The principle of tomography is to take the basic attenuation principles for a single and take multiple beam paths along the cross-section of an object at many different viewing angles to obtain enough information about that object's density, or attenuation coefficient. The detectors can be set up in different geometrical configurations, the so-called 1st, 2nd, and 3rd generation systems are most common in industrial CT:

1st generation (Figure 3.1.2): A single detector and single source is used and translated along the cross section of the object to obtain transmission data. After the desired number of translations are completed, the system then rotates and repeats until all angles are gathered. This is not often used in contemporary systems, but has been used in industrial systems due to its simplicity [37], [38].

2nd generation (Figure 3.1.2): Multiple detectors are used to improve scan times, but like the 1st generation scanner the source-detector system needs to be translated along the cross section of the object to obtain transmission data at each angle.

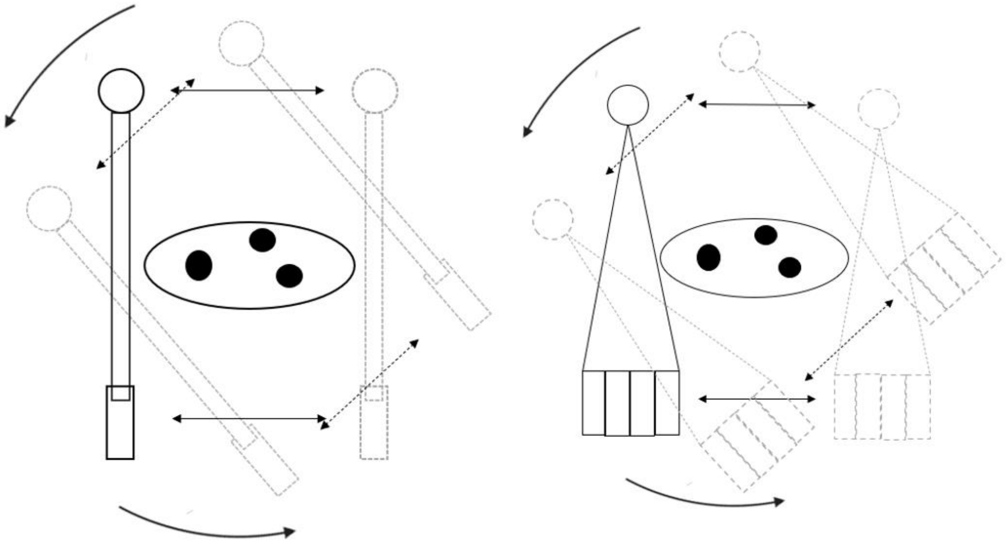

Figure 3.1.2: 1st generation (left) and 2nd generation (right) scanner configurations.

3rd generation (Figure 3.1.3): the number of detectors is enough to cover the entire object cross section, and only rotation of the source-detector system is required. The configuration can be in parallel or fan-beam (flat or arc detector) format. An arc fan beam scanning configuration is the system configuration often used in contemporary industrial CT with portable sources [70], [72], although systems with large collimated beam ports will use the parallel beam configuration [87].

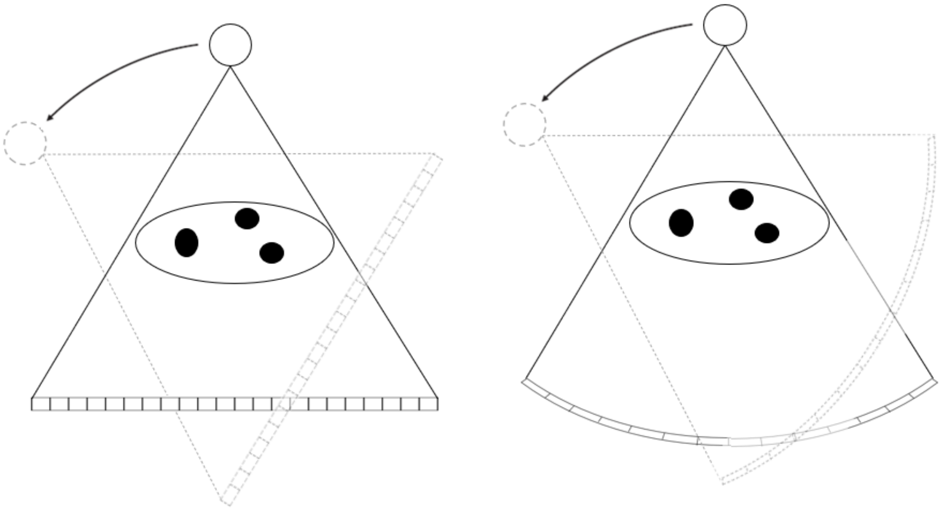

Figure 3.1.3: 3rd generation fan beam with flat (left) and arc (right) configurations.

Other scanning geometries are possible, such as 4th generation, where the detectors surround the entire object and only the source rotates (a variation of this is done by Hori et al. [42] and helical scanning methods). The method used in this thesis is the 3rd generation fan-arc configuration.

3.1.3 Projection

The CT system measurement data provides a set of information about the object’s cross-sectional composition that can be used to reconstruct the cross-sectional slice of that object. This is done in two primary steps:

1. obtain the attenuation measurement data for each detector at each desired viewing angle.
2. reconstruct the original object cross-section from this data.

This section outlines the basic measurement methodology of computed tomography and describes the two primary categories of reconstruction methods.

It is instructive to use the parallel beam geometry as an example to highlight the measurement process. Firstly, line integrals through the domain are measured by detector units. This process is represented by Beer's law:

$$\boldsymbol{P}_m = \begin{cases} p_i = \int_0^d \Sigma(x,y)ds = -\ln\left(\frac{I_i}{I_0}\right) \\ \vdots \\ p_n = \int_0^d \Sigma(x,y)ds = -\ln\left(\frac{I_n}{I_0}\right) \end{cases} \tag{3.1.5}$$

The equation represents the collection of line integrals for each ray line through the domain. Each of the n detectors, represented by the index i, has its own line integral, p_i. For a given angle index, m, the measurement data is an array of values, $\boldsymbol{P}_m$, with length equal to the number of detectors that are in the system. As the system is rotated through a total of M angles a matrix $\boldsymbol{S}$ is formed:

$$\boldsymbol{S} = \begin{pmatrix} p_{1,1} & \cdots & p_{1,N} \\ \vdots & \ddots & \vdots \\ p_{M,1} & \cdots & p_{M,N} \end{pmatrix}$$

The $\boldsymbol{S}$ matrix, with M representing the number of angles and N representing the number of detectors, is known as a sinogram (Figure 3.1.4). Each value in the sinogram matrix is the magnitude of the attenuation along the radiation path for a given angle and detector contains the information required to reconstruct the object attenuation distribution.

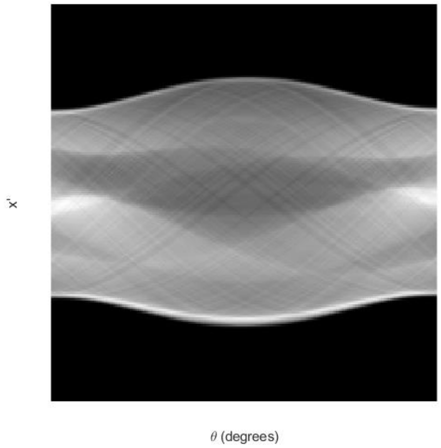

Figure 3.1.4: Example sinogram

To obtain a sinogram measurement, the rotation must be performed with a gantry with the source and detector mounted to it, or by rotating the object while holding the source-detector system stationary. Mathematically, this corresponds to rotating a coordinate system around a fixed origin point. The rotation of the coordinate system is described via the 2-D passive counterclockwise rotation matrix, **R**, which maps the coordinates (x, y) to coordinates (t, s):

$$\boldsymbol{R} = \begin{pmatrix} \cos\theta & \sin\theta \\ -\sin\theta & \cos\theta \end{pmatrix}$$

The rotation is depicted in Figure 3.1.5, where the (x, y) coordinate system represents the reference coordinates of the image domain and the (t, s) coordinates represent the frame rotated by and angle, θ.

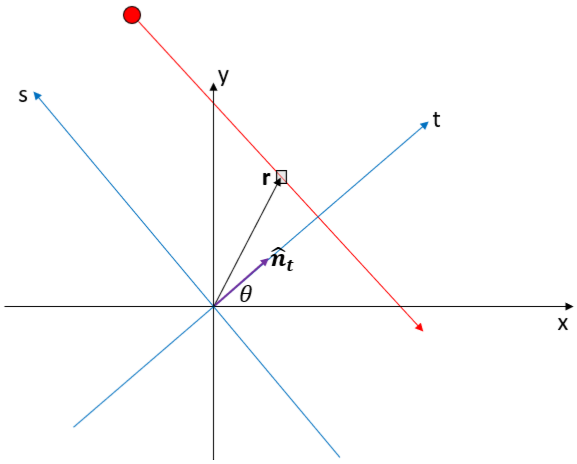

Figure 3.1.5: Coordinate rotation system.

To obtain the projections, the detector that each line integral corresponds to must be identified. In other words, the (x, y) coordinates that intersect the line going from source to detector. The value of t represents the location of a detector sampling position, and hence a detector number. To find the value of t corresponding to a vector $\boldsymbol{r}$ $(x, y$ coordinates), each point (x, y) must be expressed in terms of the t coordinate in the (t, s) coordinate system. This can be done by taking the inner product between the $\boldsymbol{r}$ vector and the normal vector of the t coordinate system ($\hat{\boldsymbol{n}}_t$), since both sets of coordinate systems have basis vectors that are mutually orthogonal.

$$\boldsymbol{r} = \begin{pmatrix} x \\ y \end{pmatrix}$$

$$\hat{\boldsymbol{n}}_t = \begin{pmatrix} \cos\theta \\ \sin\theta \end{pmatrix}$$

$$t = \boldsymbol{r}^{\boldsymbol{T}} \hat{\boldsymbol{n}}_t = x\cos\theta + y\sin\theta$$

And the projection at a given angle, for a given detector is:

$$p_\theta(t) = \int \Sigma(\boldsymbol{r})\delta(\boldsymbol{r}^{\boldsymbol{T}}\widehat{\boldsymbol{n}}_{\boldsymbol{t}} - t)d^2\boldsymbol{r}$$

Or, equivalently,

$$p_\theta(t) = \int\int \Sigma(x,y)\delta(x\cos\theta + y\sin\theta - t)dxdy \qquad (3.1.6)$$

which is known as the Radon transform. The Radon transform relates the entire set of line integrals obtained at all viewing angles around an object to a 2D function of values in Radon space (t,θ).

3.1.4 Reconstruction

The goal of reconstruction is to take the measured sinogram and reconstruct the distribution of object linear attenuation coefficients. Several reconstruction algorithms can be used to reconstruct the image domain which include iterative methods, such as the algebraic reconstruction technique (ART) methods, conjugate gradient methods (CG), and maximum likelihood methods (ML) as well as analytic methods such as filtered back-projection (FBP). An excellent primer on these algorithms is given by Bruyant [104]. The FBP and ART methods are described in this section as these methods highlight the fundamental basis behind the two methodologies. It is instructive to introduce the reconstruction concepts using parallel beam formations, with the understanding that these concepts can be extrapolated to other imaging geometries, such as fan- and cone-beam using suitable alterations to the formulas.

3.1.4.1 Filtered back projection

This thesis uses the iterative algorithms within the AIRTools II toolbox [105] to reconstruct objects, but a brief outline of the FBP method is included here as it highlights fundamental concepts in tomography such as the Fourier slice theorem (FST). The FBP algorithm has difficulty incorporating geometry and detector irregularities and prior information about the geometry or noise. However, the algorithm was used for years due to the quick reconstruction times.

A simple back-projection image can be obtained by projecting the sinogram data back over the image domain:

$$f(x, y) = \int_0^{\pi} \int_{-\infty}^{\infty} \mathrm{p}_{\theta}(t)\, \delta(x\cos\theta + y\sin\theta - t)\, dt\, d\theta \qquad (3.1.7)$$

This is however a convolution of the actual image with a blur of $1/r$ leading to a significant bright and blurry reconstructions as shown in [106]. The correct implementation of the back-projection operation is derived using the Fourier slice theorem (FST), which is summarized as:

The 1-D Fourier transform of a projection view ($P_{\theta}(w)$) at a given angle is equivalent to a line through the origin of the 2D Fourier transform of the image ($F(u, v)$) along a line at that viewing angle, θ.

A depiction of the FST is shown in Figure 3.1.6, and is mathematically described as:

$$P_{\theta}(w) = F(w cos\theta, w sin\theta) = F(w, \theta) \qquad (3.1.8)$$

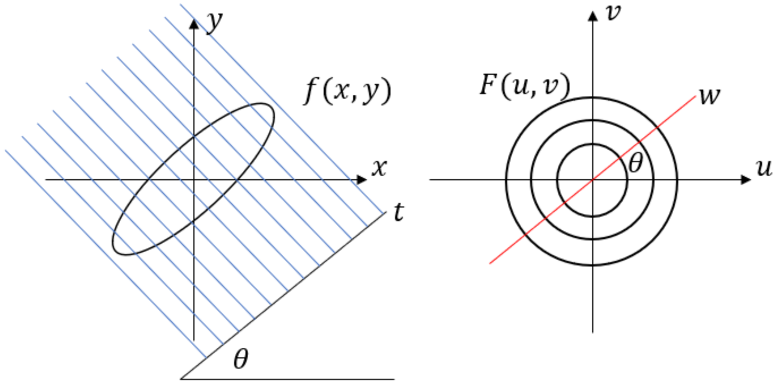

Figure 3.1.6: Depiction of the Fourier slice theorem showing the projection at a given angle (left) and the Fourier transform location along a line (red) in the frequency domain (right).

To obtain the FBP formula, the image and its Fourier transform are related through the inverse Fourier transform and converted to polar coordinates:

$$f(x,y) = \mathcal{F}_{2D}^{-1}\{F(u,v)\}$$

$$f(x,y) = \int_0^{2\pi}\int_0^{\infty} F(w,\theta)\exp\big(2\pi j w(x cos\theta + y sin\theta)\big)\, w\, dw\, d\theta$$

And by using the FST:

$$f(x,y) = \int_0^{2\pi}\int_0^{\infty} P_\theta(w)\exp\big(2\pi j w(x cos\theta + y sin\theta)\big)\, w\, dw\, d\theta$$

Which becomes:

$$f(x,y) = \int_0^{\pi} \int_{-\infty}^{\infty} |w|\, P_\theta(w) \exp\big(2\pi j w (x cos\theta + y sin\theta)\big)\ dw\, d\theta$$

$$f(x,y) = \int_0^{\pi} \left[\int_{-\infty}^{\infty} |w|\, P_\theta(w) \exp(2\pi j w t)\, dw \right]_{t = x cos\theta + y sin\theta} d\theta$$

Where the term in square brackets is a filtered 1D Fourier transform; this is the filtered back-projection formula. The addition of the filtering operation therefore leads to a correct reconstruction:

$$p_\theta^* = \mathcal{F}_{1D}^{-1}\{\mathcal{F}_{1D}\{p_\theta(t)\}|w|\}$$

$$f(x,y) = \int_0^{\pi} \int_{-\infty}^{\infty} \mathrm{p}_\theta^*(t)\ \delta(x\cos\theta + y\sin\theta - t)\ dt\, d\theta \qquad (3.1.9)$$

Which acts to filter out the artifacts introduced in simple back-projection. Note that several different weighted filter functions can be used in filtered back-projection depending on the requirements on noise and image sharpness. The methods for fan-flat, fan-arc, and cone-beam back-projection formulations can be derived using this same formulation and trigonometry.

3.1.4.2 Iterative techniques

Iterative reconstruction methods use a fundamentally different approach by converting the entire acquisition process into a system of equations, considering the discrete nature of the imaging problem. This provides some benefits over the FBP method in that detector responses, and irregular spacing, can be accounted for in the system of equations as well as source statistics and geometry and system noise properties as highlighted in [107].

A simple image acquisition example is shown in Figure 3.1.7 to illustrate the system generation.

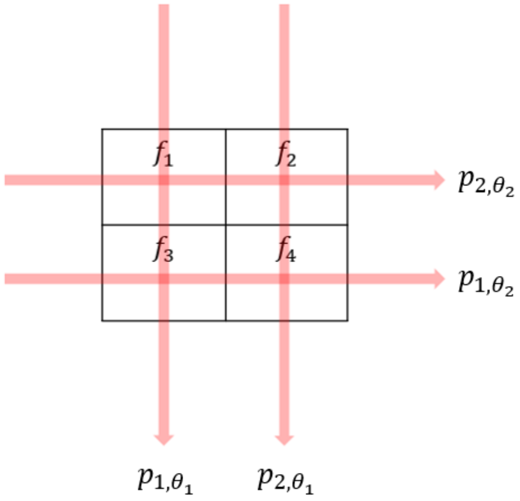

Figure 3.1.7: Example of simple projection acquisition through an image domain.

With the projection system of equations:

$$a_{11}f_1 + a_{13}f_3 = p_{1,\theta_1}$$

$$a_{22}f_2 + a_{24}f_4 = p_{2,\theta_1}$$

$$a_{31}f_1 + a_{32}f_2 = p_{2,\theta_2}$$

$$a_{43}f_3 + a_{44}f_4 = p_{1,\theta_2}$$

Where a_{ij} represents the length fraction of the ray of projection ray i through the domain pixel j. The system of equations can be represented in matrix form:

$$\boldsymbol{p} = \boldsymbol{Ax} \tag{3.1.10}$$

$$\begin{pmatrix} p_{1,\theta_1} \\ p_{2,\theta_1} \\ p_{2,\theta_2} \\ p_{1,\theta_2} \end{pmatrix} = \begin{pmatrix} a_{11} & a_{12} & a_{13} & a_{14} \\ a_{21} & a_{22} & a_{23} & a_{24} \\ a_{31} & a_{32} & a_{33} & a_{34} \\ a_{41} & a_{42} & a_{43} & a_{44} \end{pmatrix} \begin{pmatrix} f_1 \\ f_2 \\ f_3 \\ f_4 \end{pmatrix}$$

Where $\boldsymbol{x}$ is the image vector, $\boldsymbol{p}$ is the flattened sinogram data vector, and $\boldsymbol{A}$ is called the imaging system matrix. The system matrix is generated using ray-tracing algorithms of varying complexity, either calculating the intersection of lines or areas for 2D and generating the system matrix coefficients. Notably the system matrix contains information about the type of scanner geometry, whether it is and arc or flat detector, or parallel beam. For this simple case, the system matrix is small and has data without noise and thus can be solved for via direct methods such as the least squares minimum norm solution. However, this is usually not the case in practice, as the number of projection data and pixels create a large sparse matrix, making it too computational expensive. Additionally with measurement noise present, direct inversion is not possible even for small systems [106]. Thus, the primary solution method for the system of equations uses iterative solution methods, such as ART, which will be described next.

The ART algorithm uses a ray-by-ray update scheme of the image space to obtain a solution to equation $3.1.11$. The general algorithm begins with an image estimate, often set to the zero vector. A correction equation can be derived (see [108]):

$$\boldsymbol{x}^{(i)} = \boldsymbol{x}^{(i-1)} - \frac{\left(\boldsymbol{a}_i \boldsymbol{x}^{(i-1)} - \boldsymbol{p}^{(i)}\right)}{\boldsymbol{a}_i \boldsymbol{a}_i^T} \boldsymbol{a}_i^T \qquad (3.1.12)$$

And for each iteration the image pixels that the ray-line intersects is updated by the correction term:

$$\Delta x = \frac{\left(\boldsymbol{a}_i \boldsymbol{x}^{(i-1)} - \boldsymbol{p}^{(i)}\right)}{\boldsymbol{a}_i \boldsymbol{a}_i^T}$$

Where $\boldsymbol{a}_i \boldsymbol{f}^{(i-1)}$ represents the forward projection of the current image estimate. A full iteration of ART is complete when all ray sums, i, have been used in the correction.

The ART algorithm introduced here is a ray-by-ray correction scheme, meaning that it updates after each ray equation. Other iterative methods improve upon ART using simultaneous update techniques. Examples include the SIRT method which updates after all ray-line information has been used, and the pixels are updated using the average of the correction factors calculated for the pixels. The SART algorithm applies corrections for given sets of rays in a viewing angle and is a combination of the ART and SIRT methods [106]. Both methods are an extension of ART and the same matrix formulations discussed in this section are used in those algorithms. SART is claimed to provide the benefits of the SIRT and ART methods [106], providing good image quality with noisy and limited data, and has been shown to provide good quality reconstruction in the literature [65], [72]. Thus this thesis uses the SART algorithm within the AIRTools II toolbox [105] and the equation is shown in section 9.1.4.

3.1.5 Application considerations

3.1.5.1 Image resolution

The image resolution can be quantified based on the point-spread function (PSF) of the imaging system. The PSF is the impulse response of the imaging system and represents the amount of blurring incurred by a delta function point in the imaging domain. More commonly the PSF is measured using the edge-spread function (ESF) which is the measurement of a sharp edge in the image domain, a much simpler measurement. If the PSF is assumed to be isotropic, then it is related to the ESF:

$$PSF(x,y) = PSF(x) = \frac{d}{dx}ESF(x)$$

The resolution can be considered as the degree of blurring in the system and is therefore described by the full width at half maximum of the PSFs of different components of the measurement system, such as the source and detector. In an ideal imaging system, the source and detector dimensions are infinitely small, leading to minimal image blur. However, in a real system the source and detector have finite dimensions. The PSF functions of each of the source and detector are assumed Gaussian distributed in this analysis, with the source and detector size represented by the full width FWHM of the distribution (which is referred to as blur from now on). To obtain the amount of blurring in image, the contribution of the finite source dimension must be projected into the image plane.

The source and detector blur in the object plane is determined by the magnification, M:

$$M = \frac{sd}{so}$$

Which is determined by the system geometry (Figure 3.1.8).

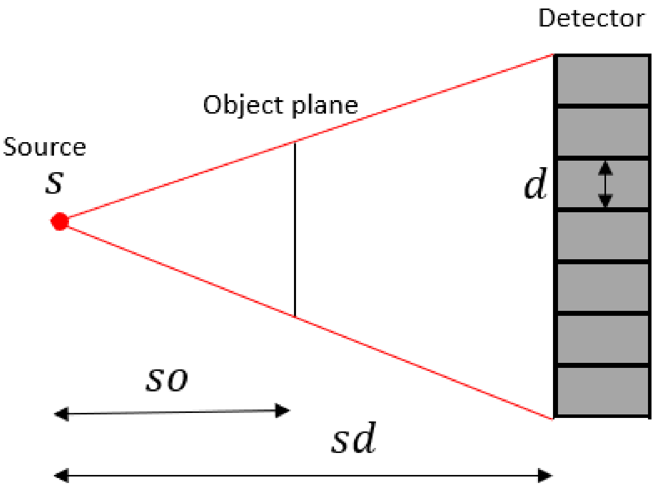

Figure 3.1.8: geometric magnification of an object plane onto a detector.

Where sd is the source to detector distance and so is the source to object distance. By projecting the source contribution into the object plane, the source blur becomes (Figure 3.1.9):

$$f = \frac{(M-1)}{M} s$$

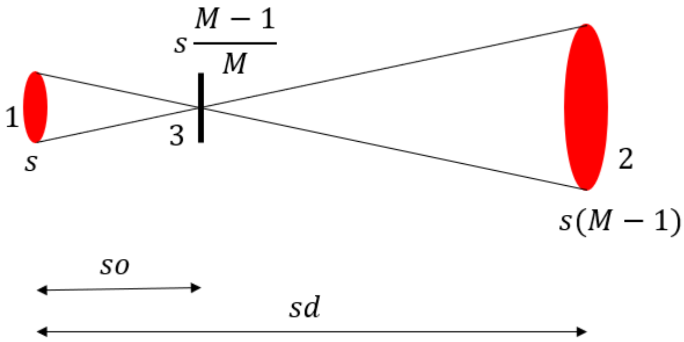

Figure 3.1.9: example of projecting the source blur into the image plane. Steps: 1) source size, 2) magnify the source size onto the detector plane, and 3) de-magnify the source image onto the object plane.

And the detector blur can be simply de-magnified into the image domain as:

$$p = \frac{d}{M}$$

Where s is the source spot size, f is the blurring caused by the source, d is the detector size, and p is the blurring caused by the detector. The blurring can be described by the detector and source PSFs, and combined via convolution to determine the overall response function:

$$PSF_{tot} = PSF_s * PSF_d$$

Since the PSF functions are considered Gaussian distributed, the total FWHM is related to the quadrature sum of the FWHM of the spot and detector PSF functions. In other words, the total blur is proportional to the quadrature sum of the blurring caused by the source and detector in the image plane:

$$U = \sqrt{f^2 + p^2}$$

$$U = \frac{1}{M}\sqrt{(M-1)^2 s^2 + d^2} \qquad (3.1.13)$$

This equation can be used to determine the optimum value of magnification necessary to maximize resolution for a given source and object geometry. An interesting method of non-dimensional expression of equation 3.1.13 can be made with respect to detector size, which is developed in [109]::

$$D(W,x) = \sqrt{(1-W)^2 x^2 + W^2} \qquad (3.1.14)$$

$$D = \frac{U}{d}, W = \frac{1}{M}, x = \frac{s}{d}$$

This equation is shown in Figure 3.1.10 and provides an excellent method of assessing image quality for every different source and detector configuration and geometry. Each curve represents a source-detector ratio, which can be identified as the intercept of the ordinate. For example, the top curve represents the source-detector ratio, $x = 2$. This curve highlights the trade-off between the source and detector blurring quantities, with the source becoming more dominant at higher magnifications ($W \rightarrow 0$) and the detector having higher influence at lower magnifications ($W \rightarrow 1$). The optimum operating point is changed depending on the source-detector ratio, x. For source spot sizes smaller than the detector pixel size ($x < 1$), the optimum resolution occurs at a higher magnification (lower source-object distance, closer to source: source-dominated) and for detector pixel sizes smaller than the source spot size ($x > 1$) the optimum shifts to lower magnifications (higher source-object distances, closer to detector: detector dominated).

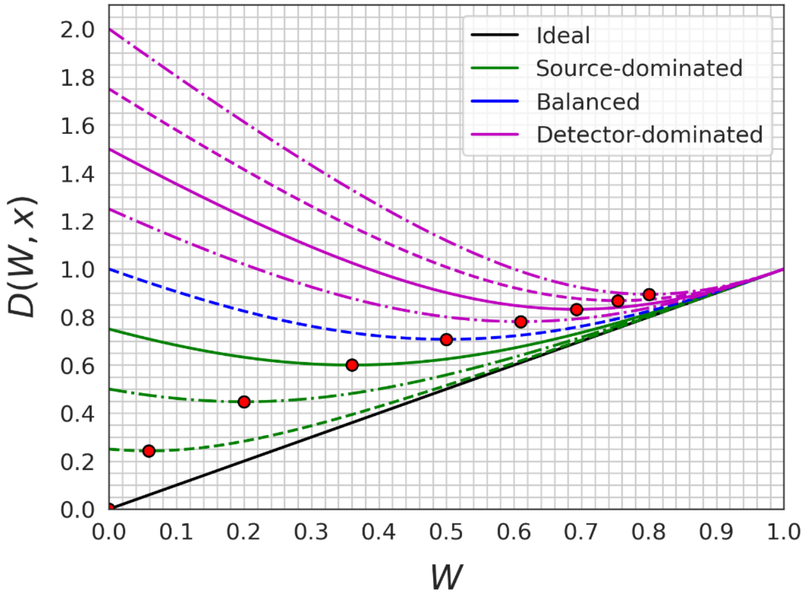

Figure 3.1.10: non-dimensional resolution curves. Note that the ordinate intercept value represents the source-pixel size ratio, x**. Red: optimum resolution design points.**

3.1.5.2 Void fraction imaging

The void fraction can be calculated using tomographic image reconstructions of each of the phases present in the 2-phase image, namely steam alone, water alone, and the two-phase flow alone. The void fraction is calculated as:

$$\alpha = \frac{\mu_{\phi}^{lin} - \mu_{f}^{lin}}{\mu_{v}^{lin} - \mu_{f}^{lin}} \tag{3.1.15}$$

Where μ_{ϕ}^{lin} is the two-phase linear attenuation coefficient, μ_{v}^{lin} is the vapour phase linear attenuation coefficient, and μ_{f}^{lin} is the water linear attenuation coefficient. However, obtaining a high-pressure and high-temperature full-steam reference image is not possible in most circumstances. An air-water calibration can be applied using the derivation from [110] who used correction factors to account for the differences in reference attenuation values between the high pressure steam-water case and the room temperature air and water reference cases. The derivation of this expression can be found in section 9.1.1, and the equation becomes:

$$\alpha = F\left(\frac{\mu_{\phi}^{lin} - \mu_{f}^{lin}}{\mu_{\mathrm{a}}^{lin} - \mu_{f}^{lin}}\right) - G \tag{3.1.16}$$

$$F = \frac{\rho_f - \left(\frac{\mu_a}{\mu_f}\right)\rho_a}{\rho_f' - \rho_v'} \qquad G = \frac{\rho_f - \rho_f'}{\rho_f' - \rho_v'}$$

A void fraction image is created from equation $3.1.17$, where each pixel represents a void fraction in the pixel area. For example, if a pixel contains 50% liquid and 50% vapour then that pixel will have a 50% void fraction in the void image (Figure 3.1.11).

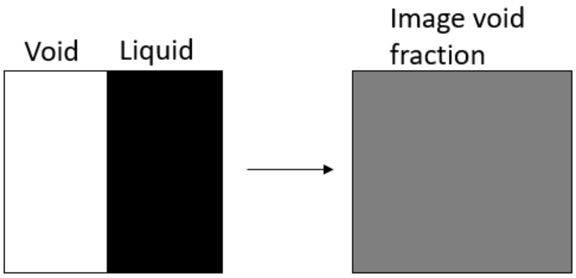

Figure 3.1.11: if an image domain pixel contains two phases (left) the pixel in the image will display the average void within that pixel (right).

The void fraction image can be displayed as a raw image with each individual pixel representing void fraction, averaged together in a subchannel, or averaged over the entire cross-section of the image. This thesis uses subchannel averaging, which averages all pixel void fraction values within a subchannel boundary to obtain a single representative void fraction for the subchannel (Figure 3.1.12).

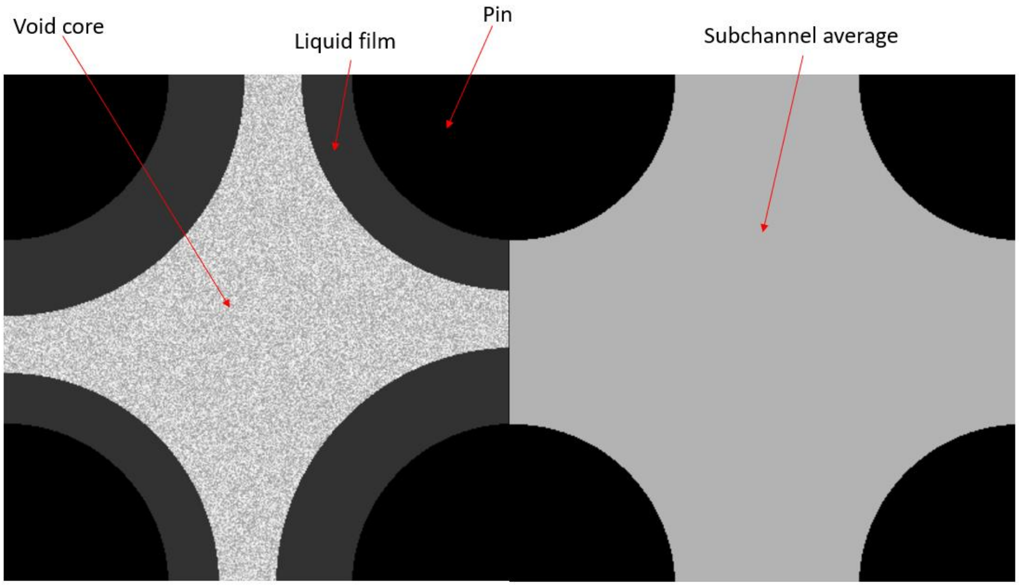

Figure 3.1.12: example distribution of void with liquid films and void core distribution (left) and the averaged representation (right).

The following sections provide related parameters that add complexity to two-phase flow imaging.

Scan time

Scan time influences the noise structure in the measured projection data and therefore the image reconstructions. In general, for a given line projection, the error depends primarily on the Poisson statistics of the source. It is therefore important to provide a high-output source coupled with high-efficiency detectors to improve counting statistics. A simple example error propagation is given along a ray-line as[2]:

$$\frac{\sigma_\alpha}{\alpha} = \frac{1}{\ln\left(\frac{I_\phi}{I_l}\right)}\sqrt{\frac{1}{tI_\phi}} \qquad (3.1.18)$$

Where I_ϕ is the count rate for the two-phase object, I_l is the count rate for the liquid phase object an t is the scan time. Equation 3.1.18 highlights that to improve statistics, the scan time or source output rate should be increased. It is noted that the reconstruction algorithm will influence the noise properties of the final image, but equation 3.1.18 shows that the optimal ways to improve measurement statistics for the system are to increase source output or scan time. For subchannel averaging of many pixels, the noise error for a subchannel averaged prediction is reduced compared to an individual pixel due to the ensemble averaging.

Flow fluctuations

Two-phase flows are always fluctuating in time and space, making it challenging to measure the time-varying void fraction precisely at every point in the domain. Tomographic measurements use time-averaged acquisitions to obtain void fraction in bundle geometries, although some systems designed for smaller tube geometries are capable of high time resolution [48]. Temporal averaging using radiation-based methods is more complex than direct temporal averaging using other methods since the void fraction attenuation measurement is not a linear function, but rather logarithmic. Hence when integrating the attenuation measurement over time, the average is such that the measured time averaged void fraction is greater than the true arithmetic average of the void fraction. The effect of temporal averaging on

---

[2] Full derivation in the section 9.1.2.

void fraction measurement has been a subject of study, albeit sparse, for several decades [5], [111]–[114], and has been referred to as the dynamic bias error.

The dynamic bias error is an error in the void fraction measurement introduced while using any radiation densitometry technique. Therefore, any system that would use a combination of such measurements, such as tomography, would be affected. In general, it has been shown that the void fraction error is primarily a function of the void profile fluctuations [111], and that for highly fluctuating flow regimes, such as slug or plug flow, the void measurement error is high (e.g., $\pm$ 20%) [112], [115]. On the other hand, the source fluctuations primarily affect the variance in the bias error [111]. In order to reduce the impact of the bias error, one can use a defined gating technique to reduce the measurement time window, however this also increases the amount of source stochastic error, and hence the random error of the bias error [111], [115].

Some methods have been developed to try and identify and correct for this effect, such as the correct averaging method [116] implementing an inverse solver method, and a simulation model to estimate and correct for the error for a simple tube [112]. More recently there was an effort to use the theoretical treatments developed by [5] to develop best practices and to correct real measured data by breaking down signals into simpler rectangular pulses [113]. It should be noted that for flows with small void fluctuations along an attenuation line (e.g., for bubbly, or high void fraction annular flows), the dynamic bias error has been shown to be small [5], [111], [115]. Notably this effect is complex even for tube geometries, and has not yet been studied for bundle void fraction tomographic measurements, but for high void fractions in a given subchannel when annular flow is present, these errors are estimated to be small based on the simple analysis by Harms and Laratta [5]. However, future research is required in this field to adequately account for the dynamic bias error in both simple geometries, as well as complex bundle geometries.

3.2 Fast Neutron Imaging System components

As outlined in the previous section, the important components governing the imaging system resolution performance are the source and detector. This section highlights the criteria of the neutron source for portable fast neutron tomography, and the detector requirements and operating principles.

3.2.1 Neutron source

A transmission imaging system relies on the measurement of radiation that has been emitted by a source and collected in some form by a detector. Neutron radiation can be created in several different ways, each with a characteristic spectrum of energies or in some cases a single energy. Neutron sources come in various forms, with different sizes, properties, and shielding requirements. The portable sources of neutrons are:

Spontaneous fission sources: isotopes that naturally, or spontaneously) fission to produce neutrons. The neutrons are emitted with a spectrum of energies characteristic of a standard prompt neutron energy spectrum. A popular isotopic source is Cf-252, which produces a fission spectrum of neutrons with a peak energy of approximately 0.5 MeV. Cf-252 provides a high neutron output of approximately $2 \text{ x } 10^{12}$ n/g or $4 \text{ x } 10^{9}$ n/Ci of Cf-252 and can be made small due to its high specific activity.

α-based emission sources: emit neutrons through the (α,n) reaction, typically using Be-9 as the target element to maximize the neutron output. To create the standalone source, an alpha emitter is alloyed with the Be-9. The alpha emitter is an actinide element that produces large alpha particle energies (~ 5 MeV). Some standard alpha emitters that are used are Am-249 and Pu-239, which output approximately 60 – 80 neutrons per 10^{6} primary α-particles.

Portable accelerator sources: sources that generally use the D-D or D-T fusion reaction to generate neutrons. These reactions are accomplished through the acceleration of deuterium ions toward a pre-loaded target containing either deuterium or tritium depending on the required neutron energy and output. Neutron outputs for commercial neutron generators for imaging are on the order of 10^8 n/s for D-D neutron generators and 10^{10} for D-T neutron generators.

Each of the sources listed above can be used in fast neutron imaging and measurement systems. α-based emitters have been used in laboratory tests in fast neutron imaging recently [117]. Spontaneous fission sources have been used successfully in both scatterometry void measurement systems measuring for transient flow measurement [90] as well as stationary object imaging systems that measure internal structures [118]. However, the use of such sources in a portable imaging system is accompanied by bulky shielding and uncontrolled emission of neutrons. Portable neutron generators have distinct benefits over other neutron sources since they are lightweight and portable with controlled emission (storage and shielding become easier) at high monoenergetic neutron output. This makes portable neutron generators ideal for a transportable imaging solution. Of the two accelerator options, the D-D neutron generator is selected for this work due to the increased neutron detection efficiency.

3.2.1.1 Fast neutron generator

The neutron generator produces neutrons through the fusion reactions:

$$ {}_{1}^{2}H + {}_{1}^{2}H \rightarrow {}_{2}^{3}He + {}_{0}^{1}n + 3.29\ \text{MeV} \tag{DD}$$

$$ {}_{1}^{2}H + {}_{1}^{3}H \rightarrow {}_{2}^{4}He + {}_{0}^{1}n + 17.6\ \text{MeV} \tag{DT}$$

These fusion reactions are accomplished by accelerating an ion beam at a target containing either deuterium or tritium. The ion beam is created by generating a plasma through the creation of free electrons via thermionic emission (heating a cathode filament), or by applying an alternating electric field using RF antennas. The free electrons cause ionization of the inert gas, generating a plasma, which is directed toward a target by applying a potential difference, typically 100-200 keV. The deuterium ions react with the loaded target (either deuterium or tritium) and produce 2 – 3 MeV neutrons for deuterated targets, or upwards of 14 MeV neutrons for tritiated targets. A simplified schematic of the overall process is shown in Figure 3.2.1.

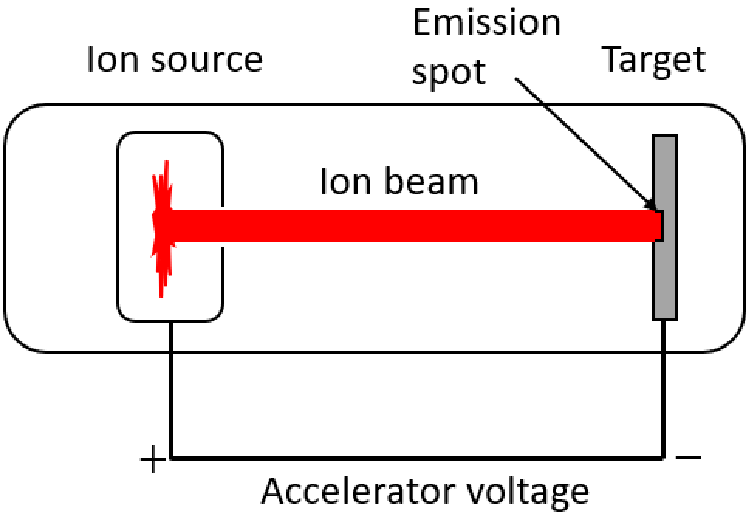

Figure 3.2.1: Neutron generator simplified schematic.

The neutron output yield for the fusion reactions has an angular dependence but can be considered monoenergetic if small angular measurement ranges are used. An example of the output from a D-D neutron source is shown in Figure 3.2.2. Notably, the neutron emission in the forward direction (emission angle of 0°) of a D-D neutron generator produces the highest fluence and is approximately 2 times the average fluence rate [96], [119] which can improve imaging scan times if that direction is used.

In addition to neutron output, another critical parameter for imaging is the neutron emission spot size. Measures to minimize the spot size while increasing the neutron output to improve scan times is a significant challenge due to lack of effective target cooling. The smallest spot size achieved for reasonable neutron outputs has been approximately 2 mm. However new target cooling designs are being developed that may increase the output further while not compromising spot size, and therefore image quality [120].

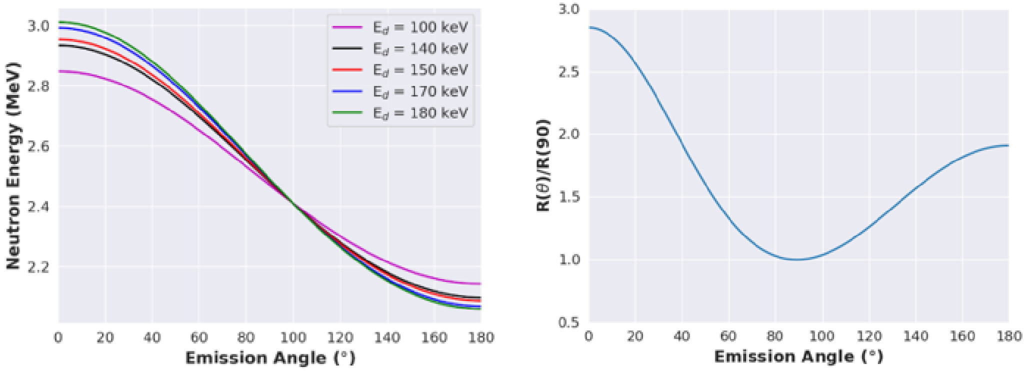

Figure 3.2.2: ***Left: Emission energy of D-D generator and right: neutron yield normalized to the 90° emission at E_d = 200 keV. Based on data from Csikai*** [119]**.**

3.2.2 Fast neutron detection

The neutron transmission measurement requires some form of conversion material and a sensor to transform the converted output into a measurable electrical signal. In some cases, the conversion material and sensor are the same (in the case of some gamma and X-ray systems that use CdTe detectors), but for fast neutron detection systems they are traditionally separated into a scintillator for radiation to light conversion and a detector for light to electrical signal conversion. This section will focus on plastic scintillators as the conversion material and the silicon photomultiplier (SiPM) as the electronic readout device.

3.2.2.1 Scintillator

A scintillator is made of a material such that when struck by radiation will produce a light output signal corresponding to the energy deposition of the interacting particle. The light output from the scintillator is measured by a light-sensitive sensor which generates a current pulse that is measured by the pulse processing electronics. This section will focus on fast neutron sensitive solid organic scintillators, and the interested reader can find a comprehensive overview of the physics and applications of many other organic and inorganic scintillators in [102].

The function of the plastic scintillator material is to convert the kinetic energy of the neutron into readily detectable light signals. For organic scintillator materials, the energy transitions happen in the energy level structure of a molecule. The energy levels responsible for fluorescence are referred to as singlet states, which are comprised of ground states and their associated vibrational states. The energy level structure is represented in the Jablonski diagram in Figure 3.2.3.

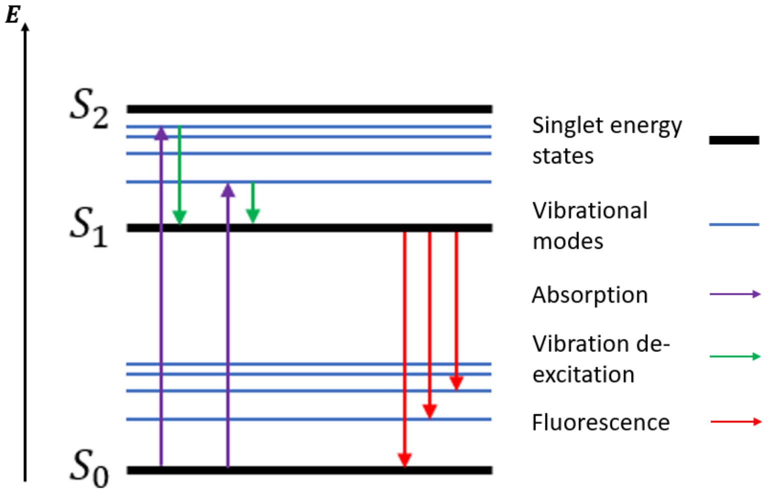

Figure 3.2.3: Example Jablonski diagram of organic scintillator energy levels.

The absorption is due to the transfer of kinetic energy of a charged particle and is represented by the upward arrows in Figure 3.2.3; the excitation can bring the molecule either into a ground state or a vibrational state. This vibrational state will lose its excess energy and move into the thermal equilibrium state of the excited state (green arrows). The higher excited states will de-excite through internal conversion to lower excited states, until the energy is that of the first excited state [102] and therefore the energy of the first excited state is responsible for the scintillator fluorescence spectrum (red arrows). The fluorescence light output is emitted with a fast decay time on the order of a few nanoseconds, which provides high count rate capability.

The magnitude of the light emission (number of photons) of the plastic scintillator depends on the energy and type of incident radiation. In general, light emission is linear with energy for radiation that produces recoil electrons (photon-based sources), and non-linear for radiation that produces heavy charged recoil particles (e.g., recoil protons). The light emission for the BC400 plastic scintillator is shown in Figure 3.2.4 (note that the light emission from heavy charged particles is always less in magnitude than that for electrons). The BC400 scintillator is used in neutron detection due to its high hydrogen content.

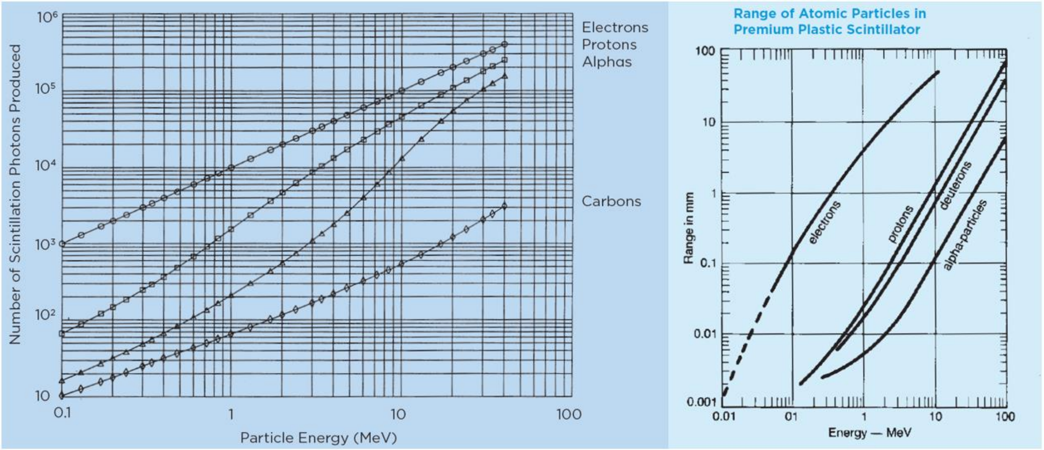

Figure 3.2.4: Left: light output of Saint Gobain BC400 scintillator and right: the range of various charged particles [121].

The light emission response, in combination with the neutron interaction energy spectrum produces the expected measured output spectrum from the scintillator. Therefore, to determine the expected detector output spectrum it is necessary to begin with the basic interaction of a neutron with the scintillator, namely an elastic collision. In an elastic collision the neutron collides with a hydrogen atom and transfers part of its energy and momentum. The neutron loses some of its energy in the collision and changes trajectory, while the target hydrogen atom will become a recoil proton and travel with its own trajectory and energy.

The collision physics between the recoil particle and neutron can be described using simple conservation of momentum and energy analysis, and the interested reader can find the full derivation in [122]–[124]. In the case of hydrogen-rich scintillators the final neutron energy distribution is uniform from 0 up to the maximum incident neutron energy [102], [125]. The full derivation of the expression for the scattered neutron probability distribution for scatter from an initial to a final energy can be seen in [124], and is expressed as

$$P(E_i \rightarrow E_f) = \begin{cases} \frac{1}{E_i}, & 0 \leq E_f \leq E_i \\ 0\,, & else \end{cases} \tag{3.2.1}$$

And the recoil proton distribution can be shown to follow the same uniform distribution (Figure 3.2.5)

$$P(0 \rightarrow E_p) = \begin{cases} \frac{1}{E_i}, & 0 \leq E_p \leq E_i \\ 0\,, & else \end{cases} \tag{3.2.2}$$

The flat shape of this distribution simplifies analysis and has important consequences for parameters such as efficiency, the light output response, and ultimately the final detector measured response. For example, the flat recoil distribution complicates the choice of discrimination level for the rejection of scattered neutrons since neutrons produce recoil protons at all energies with equal probability (i.e., the discrimination level will remove both the scattered contribution as well as a portion of the direct contribution).

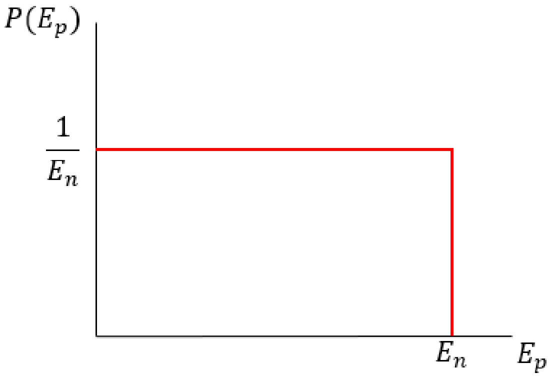

Figure 3.2.5: Theoretical proton recoil distribution.

To obtain the light output spectrum of the scintillator, the flat recoil proton response (the differential count spectrum) is combined with the light output spectrum from the scintillator. The light output response would be the same as the recoil energy spectrum if the light output from the scintillator is linear, as in recoil electron interactions. However, the light output is non-linear for recoil protons and modifies the detector output response. The light output spectrum (L) for organic scintillators, such as the Saint Gobain BC400 scintillator, follows a roughly $E^{3/2}$ trend and will be used here to derive an expected output response. Therefore, following the derivations in [102], [125],

$$L = CE^{\frac{3}{2}} \quad \frac{dN}{dE} = \frac{1}{E_n} = \text{const}$$

$$\frac{dN}{dL} = \frac{\frac{dN}{dE}}{\frac{dL}{dE}} = \frac{const}{C\left(\frac{3}{2}\right)E^{\frac{1}{2}}} = C'L^{-\frac{1}{3}}$$

Where L is the light output response of the scintillator, dN/dE is the differential energy spectrum, E_n is the maximum neutron energy, C and C' are arbitrary constants, and dN/dL is the measured differential light output spectrum. Although the derivation is an approximation, the exercise highlights the general trend that the non-linearity of the scintillator light output causes the output response to increase at lower light yields (Figure 3.2.6).

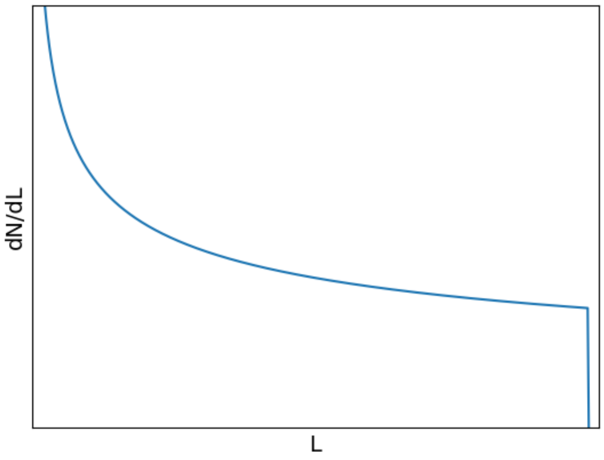

Figure 3.2.6: Light output response of a plastic scintillator due to fast neutrons.

Thus far, the scintillator analysis has only considered hydrogen in the scintillator. However, organic plastic scintillators contain some Carbon atoms that produce competing effects for recoil proton generation, thus thresholding the maximum possible efficiency. The carbon interaction does not provide significant light output, due to minimal scintillation light emission for recoil carbon nuclei (Figure 3.2.4) and therefore acts to eliminate some of the measurable hydrogen scatter interactions. For neutron energies of 2.8 MeV, the intrinsic efficiency is limited to about 60%:

$$\epsilon_H = \frac{N_H \sigma_H}{N_H \sigma_H + N_C \sigma_C}$$

Where N_H is the atom density of hydrogen, N_C is the atom density of Carbon, σ_H is the microscopic cross section of hydrogen, and σ_C is the microscopic cross section of carbon. This maximum efficiency is dependent on scintillator depth (z):

$$\epsilon_H = \frac{N_H \sigma_H}{N_H \sigma_H + N_C \sigma_C} (1 - \exp(-(N_H \sigma_H + N_C \sigma_C) z)) \qquad (3.2.3)$$

Thresholding is a process used to eliminate unwanted counts or events below a specified energy. The thresholding process alters the interaction efficiency of the scintillator due to the flat recoil spectrum (i.e., the threshold removes some direct counts). The threshold further reduces the efficiency value by a factor of $(1 - E_{thresh}/E_n)$ due to the flat neutron interaction distribution, and thus optimization with noise counts is required. An important secondary effect involves the energy of the recoil protons. This is a function of scintillator width, which is a deciding factor for the achievable resolution in any imaging system. In this case, the minimum pixel size is desired to improve resolution. However, if a scintillator is too small, it is possible that the recoil proton exceeds the range within the material and exits the scintillator before complete energy deposition (proton bleed), thus biasing toward lower energies (Figure 3.2.7). The range for D-D neutrons in the BC400 scintillator is ~ 0.1 mm and for small scintillator sizes used with D-D generators on this order ($< 1\ \mathrm{mm}^2$), the effect proton bleed effect can be appreciable [126]. In this thesis a pixel size of 3 mm is used and therefore the proton bleed effect is not significant.

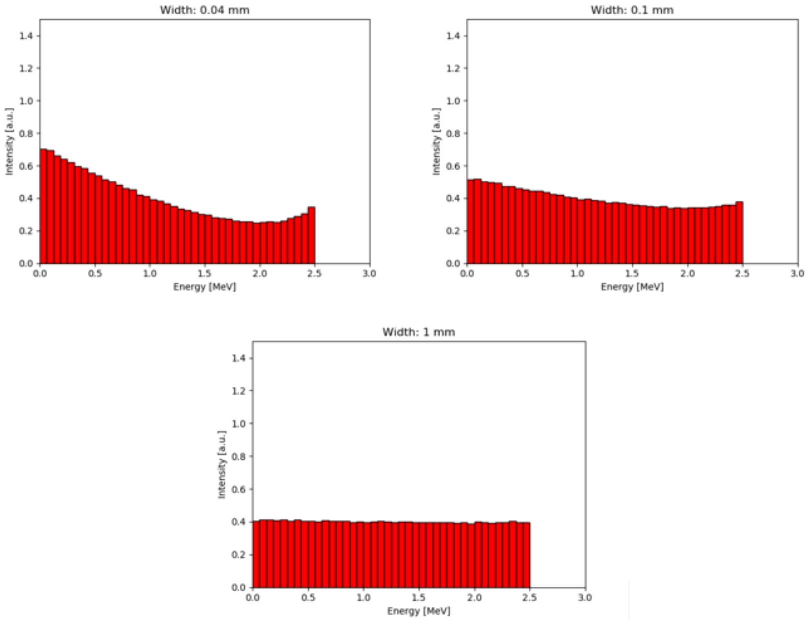

Figure 3.2.7: recoil proton spectra for different pixel sizes. Data based on the research by Andersson et al. [126].

3.2.2.2 Light detection

The light sensors need a small form factor and robust nature to be used in a portable system. The silicon photomultiplier (SiPM) fits this need and is a small, lightweight, solid-state light sensor with a high gain like a photomultiplier tube, but are much smaller, robust, and lower cost than traditional photomultiplier tubes. Additionally, the SiPM structure provides a simple way to create arrays of sensors (i.e., pixels) suitable for radiation imaging. A synopsis of the design and operation of SiPMs is given in [102], [127], [128] and is summarized here.

Each SiPM is composed of many (often thousands) individual single-photon avalanche photodiodes (SPADs) connected in parallel. The number of cells firing is therefore proportional to the incident photons on the sensor. Each SPAD on the SiPM is in an active region known as Geiger mode when a reverse bias voltage above the breakdown voltage (known as the overvoltage) is applied. This mode of operation facilitates avalanche multiplication which generates many charge carriers from a single photon interaction leading to a large signal gain for each SPAD connected in parallel. The total output of the parallel SPADs is an analog signal whose amplitude is proportional to number of photons hitting the cell.

In addition to signal gain, other factors dictate the output signal of the SiPM:

<u>PDE:</u> The light sensor photon detection efficiency (PDE) must be closely matched to the output light spectrum of the scintillator material to maximize light collection efficiency. The dimensions of the sensor (or multiple sensors) must fit within the scintillator in which it is coupled. Effectively the minimum scintillator width is dictated by the SiPM minimum pixel size.

<u>Noise:</u> These are known as crosstalk and dark noise. The crosstalk noise occurs when an avalanche triggers in one cell and causes another to trigger through light emission due to photons emitted during the avalanche process. The dark noise is caused via thermal excitation of a charge carrier causing an avalanche process with no incident light present. In scintillation counting where large numbers of photons are measured, these noise sources can be reduced via an adequate threshold. There is a strong dependence of noise, as well as PDE, and gain, on the bias voltage and temperature of the SiPM. This dependence can be managed through monitoring temperature and maintaining a constant overvoltage.

It is desirable to maximize dynamic range and gain, while minimizing noise, however this is a function of overvoltage and microcell size. Notably, as outlined in [128]:

- For a constant overvoltage, as the microcell size decreases for a given active area to increase the dynamic range the gain and PDE of the SiPM will decrease, along with the crosstalk noise.
- As the overvoltage increases, the gain, PDE, crosstalk noise and dark noise all increase.

And care must be taken to select the operating point and size of the SiPM for optimal light collection and noise characteristics for the desired application.

3.2.3 Summary

This section outlined the basic principles of tomography and the application to void fraction imaging. The operating principles and selection criteria for the neutron source and detector equipment have been outlined:

Source size: the source spot size determines the maximum achievable resolution and is a function of neutron generator technology and should be minimized. However, the minimum spot size is determined by the level of cooling available to the target and therefore is a function of current neutron generator technology (~2 mm diameter spot).

Detector size: the scintillator and light sensor size also determine the maximum resolution of the system and should be minimized. The scintillator size is limited to approximately 1 mm^2 due to the proton bleed effect. The SiPM footprint needs to match the output light characteristics and footprint of the scintillator, and the minimum size is also set to 1 mm^2.

These constraints and some additional constraints are introduced in the next section, and a simulation study to explore the noise effects and void fraction prediction capabilities of the imaging system is presented.

4 System characterization simulations

> *You must expect great*
> *things of yourself*
> *before you can do them*
> Michael Jordan

The primary parameters used to quantify the performance of the imaging system are the resolution and contrast which are affected by quantum noise, stochastic decay, as well as scattering effects (i.e., crosstalk and background scatter). Simulations were done to quantify these noise properties, as well as the effect the noise has on the system resolution and void measurement capabilities of the FNCTS. Background count simulations were done for each of the three test facilities: McMaster, Ontario Tech, and Stern Laboratories. The information from these simulations was used to determine the subchannel averaged void fraction prediction capabilities for a case study of a CANDU phantom.

There are several constraints on the system based on facility application as well as equipment limitations as outlined in the previous section. The constraints are as follows:

Facility dimensions: constrains the source-object distance to a minimum of 20 cm since this is the closest that the neutron source can be placed to the test section; placing the object as close as possible maximizes the useable solid angle and therefore the number of neutrons available for imaging. Additionally, the source-detector distance is set at a maximum of 60 cm due to required clearance in the final testing facility. Note that these distances can be altered if necessary to facilitate the application to other test section geometries but were selected to allow for the system to be installed in the existing Stern Laboratories CHF facility.

Detector pixel dimension: The pixel size should be as small as possible to minimize the detector blur and optimize resolution. As the size of pixels (such as 1 mm) decreases, the number of pixels required to span a given area also increases, thus increasing the cost. However, shrinking the pixels causes potential crosstalk issues within the scintillator resulting from recoil protons travelling into adjacent pixels more frequently [126]. Therefore, the smallest pixel size available with both cost and resolution in mind is 3 mm. Additionally, to provide a foundation for later 3D imaging, the detector array was chosen to be in 8x8 flat array (64 total pixels) format to facilitate cone-beam imaging, as well as fan beam imaging.

Number of detectors: the minimum number of detectors is the number of pixels required to span the internal structure of the test section. Using 3 mm pixels in an 8x8 format means that the minimum number of arrays is 13 to span the final application CANDU geometry diameter. The number of arrays is determined using the diameter of the inner channel of 10 cm and magnification of 3 from which the arc length of the required detector array (about 30 cm) can be calculated. This length corresponds to 12.5 detector arrays of 8 pixels, which is rounded up to 13 to give the final number of detector units required. However, given that the processing circuitry connects to 2 8x8 SiPM arrays per processing board, the number of detector arrays is rounded up to 14 and the final number of pixels in the entire array is therefore 896 (112 pixels spanning the cross section and 8 pixels in the axial direction).

Scintillator thickness: The scintillator thickness is chosen to be 5 cm since this is the mean free path through the plastic scintillator material for neutrons between 2.5 MeV and 2.8 MeV. This method is the same as Andersson [94] in which the mean free path provides a general applicability to a variety of geometry and room configurations while maintaining a high interaction efficiency without increasing background counts excessively. This thickness is used in the crosstalk and background count simulations to calculate the interaction efficiencies, crosstalk percentages, and background counts.

Source spot size: The most up-to-date neutron generator technology provides 2 mm as the smallest possible spot size. Interestingly if the generator can be oriented perpendicular to the imaging plane, a smaller spot size can theoretically be obtained – potentially down to 0.2-0.5 mm [92]; this has not been tested extensively in other systems. However, using the side emission also provides less neutron yield, and therefore creates a trade-off between scan time and resolution.

Using equation 3.1.14 with the above constraints for the spot size, detector pixel size, and system spacing dimensions provide a theoretical resolution of:

$$x = \frac{s}{d} = \frac{2\text{ mm}}{3\text{ mm}} = 0.67$$

$$W = \frac{1}{M} = \frac{so}{sd} = \frac{1}{3}$$

$$D(W,x) = \left(\sqrt{(1-W)^2x^2 + W^2}\right) \cong 0.6$$

$$U = dD(W,x) \cong \mathbf{1.7\ mm}$$

Shown in (Figure 3.2.8), which is close to the optimum value for this source to pixel ratio, x. The calculated resolution value is used as a blurring filter in the high-throughput MATLAB simulations to create the measured attenuation profiles.

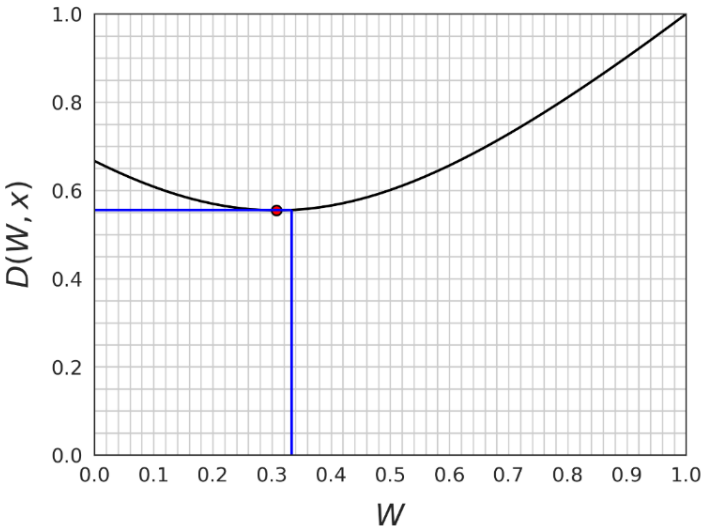

Figure 3.2.8: Resolution plot indicating the optimum for the FNCTS.

An important point concerning the resolution capabilities of this system is that it is not fine enough to measure the resolved structure of small liquid films or other structures that occur at or near CHF. However, for the current system small features such as liquid films and disturbance waves are reconstructed as pixel averaged attenuations in the image (see Figure 3.1.11). For example, thin liquid films are detected with the same pixel thickness as thicker films in the image, but with a lower liquid fraction within a pixel (Figure 3.2.9). Thus, while liquid films or interfacial waves are not structurally resolved, the films are part of a pixel average that can be used in subchannel averaging, rather than a direct liquid film feature measurement. However, by inferring a liquid/vapour separated flow in the pixel region adjacent to the pin, a liquid height can also be inferred based on the image pixel void fraction despite the system resolution of ∼1.7 mm.

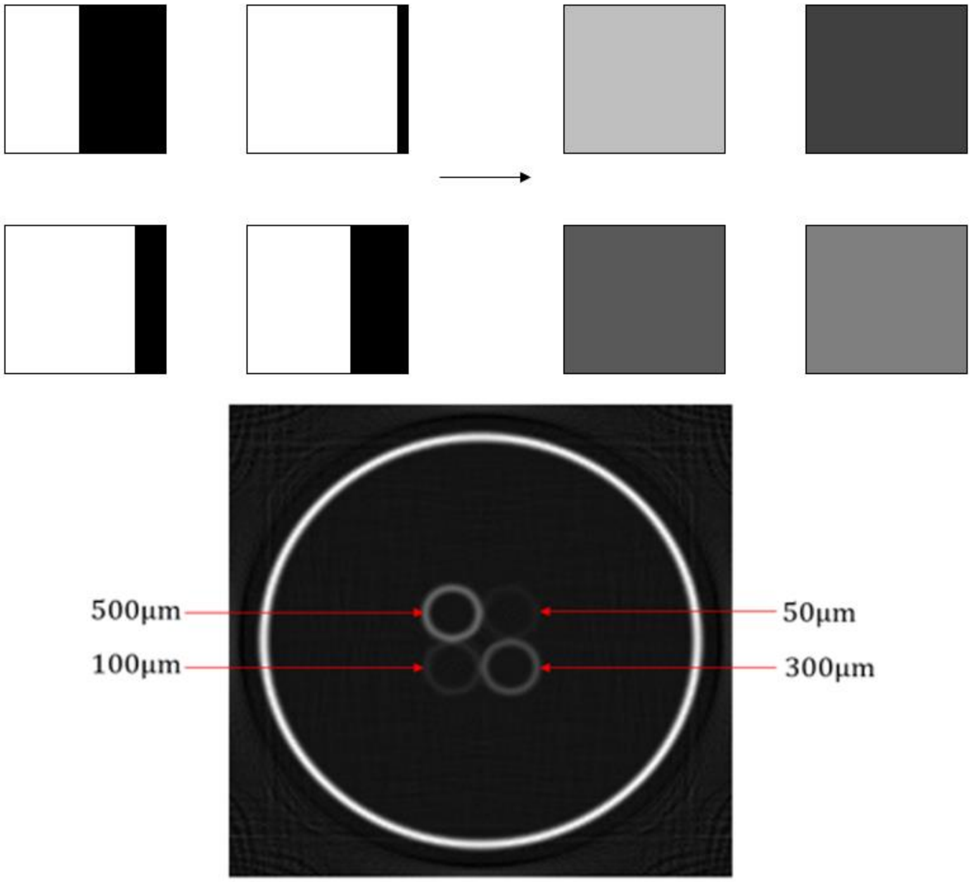

Figure 3.2.9: Liquid film thicknesses impact on pixel average void fraction near a pin. Top left: the liquid film in black and void in white take up space in the pixel with varying thicknesses. Top right: the representation of the void within the image domain is uniform but varies in image grey value. Bottom: An example representation of the liquid films in the image domain. Notice that the films appear the same size but vary in a grey value which varies as a function of film thickness.

4.1 Indirect counting effects on the attenuation profile

With the resolution quantified, a detailed analysis of indirect counting effects on the attenuation profile is conducted. These indirect counting effects are caused by neutrons scattered into a pixel and not coming directly from the source. Examples include scattered neutrons from shielding, the test object, and from adjacent pixels. The measured number of counts at a detector with indirect counts included is a function of multiple variables:

$$I = I_0 \exp(-\mu s) + BI_0 + B_{obj} I_0 + XI_0 \qquad (4.1.1)$$

Where B is the background fraction due to surrounding materials (i.e., shielding, walls, floor, etc.), B_{obj} is the background fraction due to scattering from the object, and X is the crosstalk count fraction due to a neutron scattering from one scintillator element and interacting in another. The physical depiction of these noise sources is shown in Figure 4.1.1.

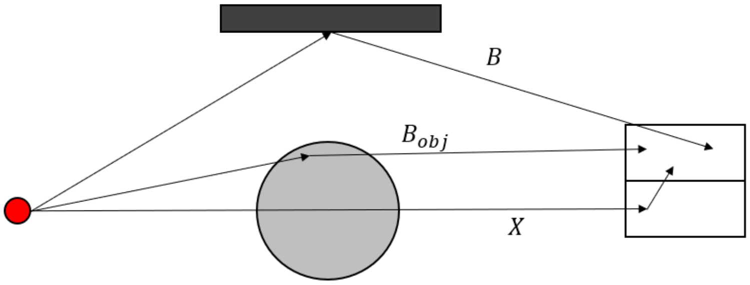

Figure 4.1.1: Scattering mechanisms.

The effect that these variables have on the attenuation profile is complex and geometry dependent, especially for fast neutrons since there is no peak in the energy spectrum that can be identified to eliminate scatter counts.

The next sections explore the effect of the background and crosstalk counts on the attenuation profile, beginning with the background and object scatter fractions and concluding with the crosstalk simulations. This information provides the foundation for a simulation study to quantify the void fraction prediction capabilities of the imaging system.

4.1.1 Background scatter

The background count rate is an important parameter to quantify as it reduces the effective attenuation that an imaging system can measure. This is easily explained for a single transmission acquisition: for a given transmission measurement more counts would reach the detector due to surrounding in-scatter, which indicates less material since more counts indicate a higher transmission (lower attenuation). However, the background counts affect the flat field and object field equally, and so the effect is more nuanced when calculating attenuation values for sinograms. An expression for the background counts can be derived by examining the simplified physical scenario in Figure 4.1.2.

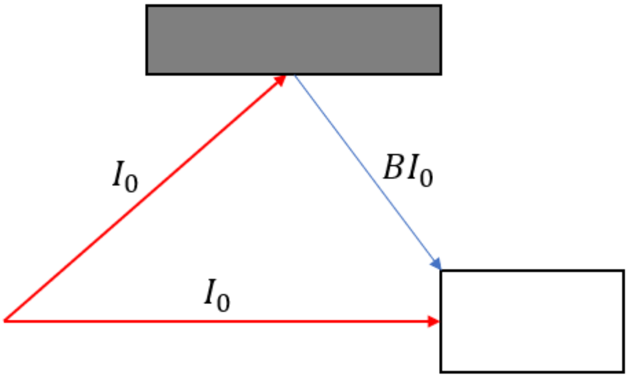

Figure 4.1.2: Physical mechanism of background scattering.

To calculate the attenuation along a ray-line, the flat-field (I_{0B}) and object-field (I_{TB}) measurements are required:

$$I_{0B} = I_0 + BI_0 \qquad \text{(flat)}$$

$$I_{TB} = TI_0 + BI_0 \qquad \text{(object)}$$

In the ideal case, B is equal to 0, and thus

$$A_{ideal} = -\ln\left(\frac{I_{TB}}{I_{0B}}\right) = -\ln\,(T)$$

Whereas with $B \neq 0$

$$A_B = -\ln(T) - \ln\left(\frac{1 + \frac{B}{T}}{1 + B}\right)$$

and the attenuation error due to background counts is therefore:

$$A_{err} = \ln\left(\frac{1 + \frac{B}{T}}{1 + B}\right)$$

Which is always positive, since $0 \leq T \leq 1$, leading to a systematic underprediction of attenuation in all cases that $B > 0$. The error in attenuation is plotted as a function of T and B in Figure 4.1.3 and clearly shows the necessity to minimize background fraction to reduce underprediction error in predicted attenuation value for a given transmission characteristic. Notably, in the limit as $B \rightarrow \infty$ the attenuation value would approach 0. Fortunately it is possible to measure and correct for the background fraction experimentally (outlined in [72]), as well as simulate and determine correction factors. The next section provides background count correction factors derived from simulation that can be used on experimental data to obtain correct attenuation values.

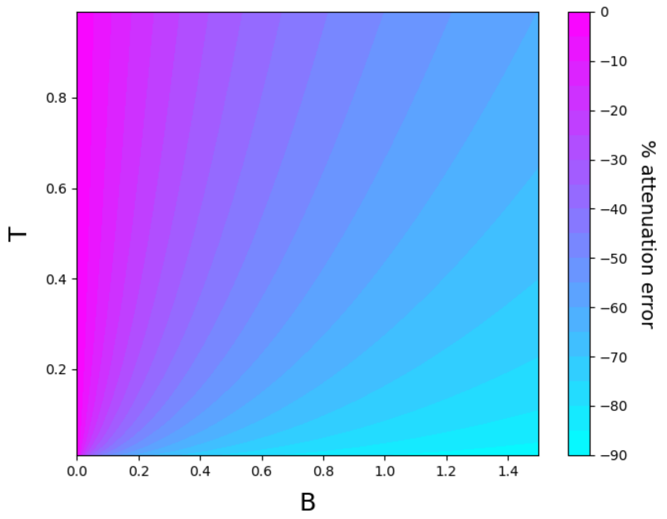

Figure 4.1.3: Attenuation error as a function of transmission fraction and background scatter fraction.

4.1.1.1 Environmental background simulation

The background scatter energy spectrum provides a means to determine a detector energy threshold to eliminate as many background noise counts as possible and provide a correction factor for a given threshold. The scatter fraction data were simulated and measured using the F5 point detector tally in MCNP6, which gathers information on the fluence energy spectrum at a specific point in space. Through this tally the reaction rates are calculated for various detector energy thresholds and post-processed in a custom Python script. The overall data processing flow is shown in Figure 4.1.4.

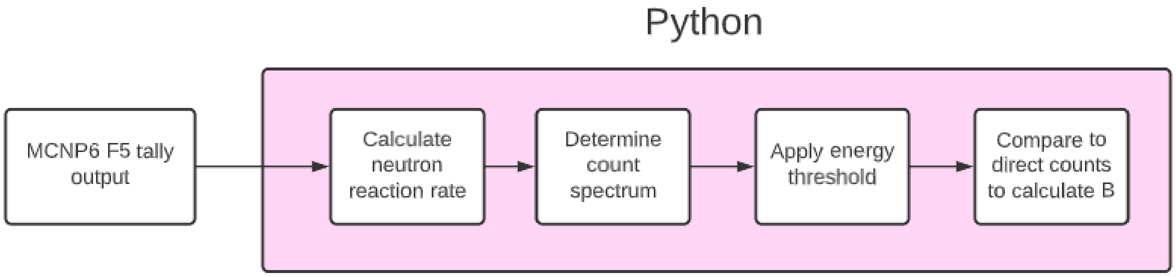

Figure 4.1.4: Background simulation process flow.

Two different benchtop testing environments are simulated:

- McMaster accelerator beam hall, the primary benchtop testing facility.
- Ontario Tech laboratory environment, the secondary testing facility.

As well as the final application environment at Stern Laboratories. In each of the environments the structures nearby the measurement system were included. The source-detector distance was set at 60 cm based on the constraints noted in the previous section. However, this distance is reduced to 40 cm for the Ontario Tech setup to account for changes in geometry due to the smaller source output.

McMaster Laboratory

The McMaster laboratory simulation is composed of a plastic detector box unit, two wooden tables, an aluminum alignment beam, and the concrete floor and adjacent wall (Figure 4.1.5). The other walls and ceiling were not considered as they are over 3.5 m away from the system and hence provide negligible contributions to the scatter fraction. The scatter fraction across the angular span of the detector array is shown in Figure 4.1.6. The measurement positions are chosen as the angular span of the detector array since the object is rotated in this setup (i.e., the detector position does not change during the acquisition). The indirect fraction is approximately constant over the angular span of the array and the fraction decreases with increasing energy threshold. The difference on one side of the detector array is due to the close wall on one side of the array.

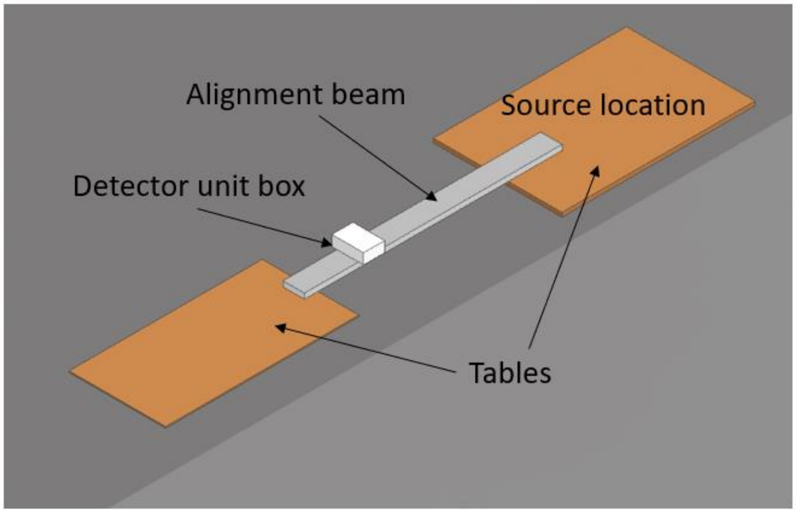

Figure 4.1.5: McMaster University lab facility simulation design.

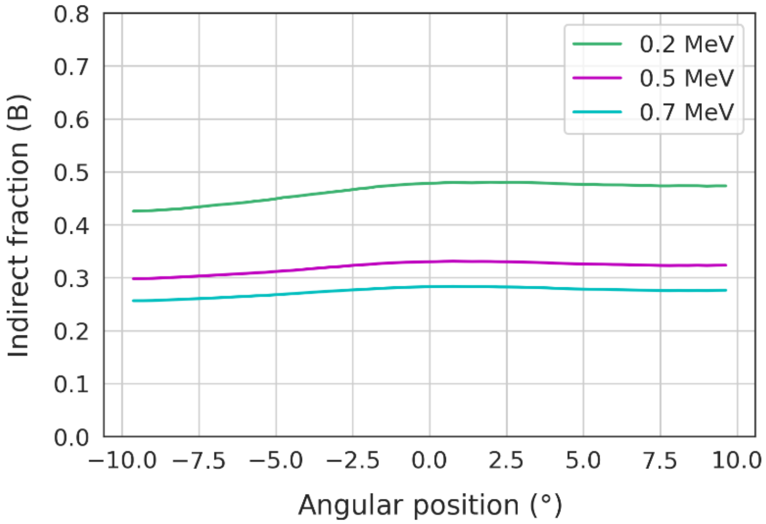

Figure 4.1.6: Detector array scatter fraction with different detector energy thresholds at different detector pixel position at McMaster University.

Ontario tech laboratory

The Ontario Tech facility is shown in Figure 4.1.7. The simulation includes the aluminum alignment beams, table and the generator alignment beam as well as the concrete flooring and walls. The scatter fraction is shown across the full detector array and is noticeably flat, owing to the symmetric room structure.

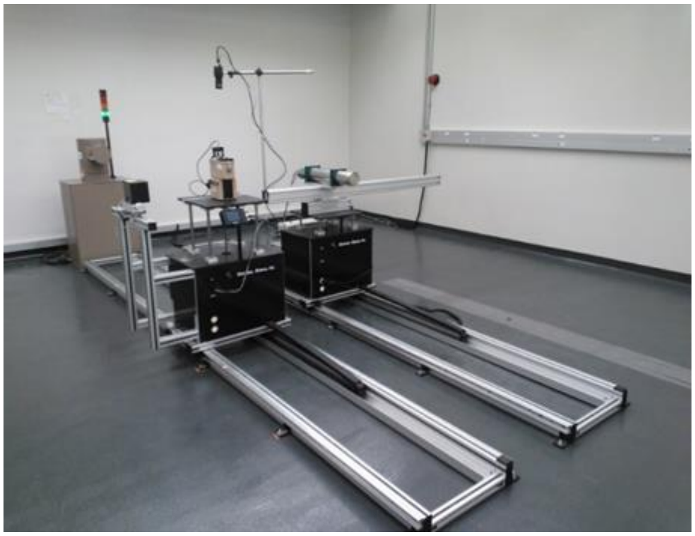

Figure 4.1.7: Ontario Tech neutron generator facility.

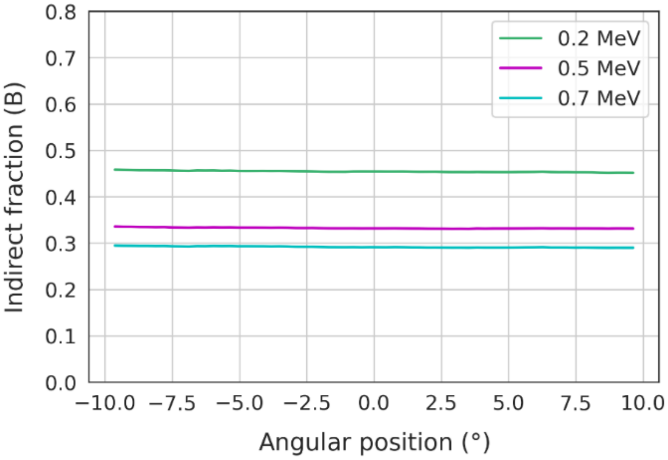

Figure 4.1.8: Detector array scatter fraction with different detector energy thresholds at different detector pixel position at Ontario Tech.

Stern Laboratories

The Stern lab facility involved the I-beam structures as well as the concrete flooring and walls. A more detailed simulation is necessary to improve performance since the equipment placement as well as object composition around the test section is not definitively known at the time of writing. The plot shows the angular dependence over a full 360° since the detector rotates around the test object in this case. The scatter fraction of the room shows a scanning angle dependence (Figure 4.1.9), owing to the concrete flooring placed at the bottom of the I-beam.

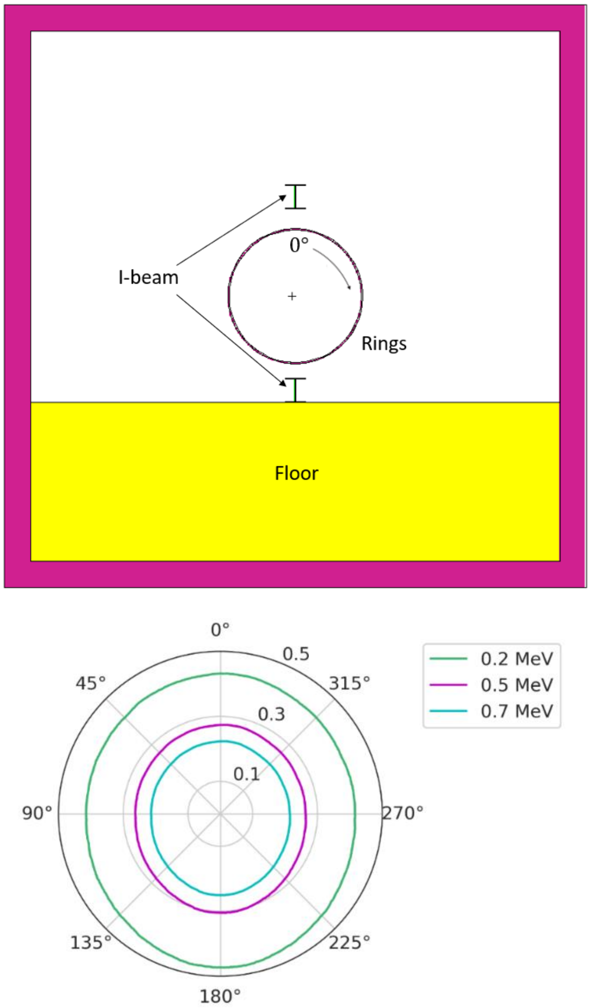

Figure 4.1.9: Stern Laboratories simulation room (top) and the scatter fraction angular dependence (bottom)

The simulation results highlight the necessity of measuring the background fraction for different measurement locations as each case presents a different background fraction distribution and magnitude. This is highlighted by comparing the McMaster laboratory, which has a lop-sided background distribution due to a nearby wall (Figure 4.1.6), and the Ontario Tech laboratory which has a more uniform distribution (Figure 4.1.7). Based on the three laboratory configurations the background fraction, B, can be filtered to $\sim 0.25 - 0.3$ using a threshold of 0.7 MeV in each laboratory environment, although the threshold can be adjusted to further reduce background fraction as needed. However, since the Stern Laboratories background fraction varies continuously around the object, there is no easily definable threshold.

4.1.1.2 Object scattering

Object scattering has the same effect as background scattering in that the attenuation values are reduced. However, the effect is only present in the object field of measurement, meaning that it is difficult to experimentally measure. Following a similar logic to background scatter events, the effect of object background counts can be quantified:

$$A_{B_{obj}} = -\ln(T) - \ln\left(1 + \frac{B_{obj}}{T}\right)$$

and the attenuation error due to background counts is therefore:

$$A_{B_{obj}err} = \ln\left(1 + \frac{B_{obj}}{T}\right)$$

Unlike the background fraction, in the limit as $B_{obj} \to \infty$ the attenuation value continuously decreases and becomes more and more negative, since the counts in the object case would become higher than counts corresponding to the flat field. The object background fraction, B_{obj}, is a function of object material and geometry, and cannot be measured in-situ. Additionally, every scanned object will create a different object scatter fraction, meaning that different corrections are required for different test objects and for different liquid/vapour fractions. Therefore, MCNP6 simulations (the same method as the background scatter simulations) for representative objects have been done to quantify the effect and develop correction factors. The first geometry is a tube array which is used in the Ontario Tech tests. The scatter fractions are shown in Figure 4.1.10 and show that the object scatter is a much smaller fraction compared to the background scatter fraction. The second object is the CANDU bundle for the final application at Stern Laboratories (Figure 4.1.11). A cross-sectional void fraction was simulated by altering the density of water within the bundle according to the mixture density equation:

$$\rho_m = (1-\alpha)\rho_l + \alpha\rho_g \qquad (4.1.2)$$

The plot is shown in Figure 4.1.11. Since the CANDU bundle is a constant geometry (for 37-element), a multi-variable fit to the CANDU object scatter fraction has been made as a function of cross-sectional void fraction and energy threshold using a TensorFlow optimizer. This curve can be used along with cross-sectional void average predictions (such an estimate can be obtained via differential pressure measurements) to determine an object scatter fraction correction to the final application measurements. The fit is expressed as:

$$B_{obj}(\alpha, E_{thresh}) = \begin{cases} 0.103 + 0.009\alpha - 0.074\ln(E_{thresh}), & E_{thresh} \leq 1.5\text{ MeV} \\ 0.106 + 0.005\alpha - 0.089\ln(E_{thresh}), & E_{thresh} > 1.5\text{ MeV} \end{cases}$$

The simulations indicate that the CANDU object background is a strong function of pressure boundary and insulator material and a weak function of void fraction and is roughly half of the value of the Stern Laboratories background fraction.

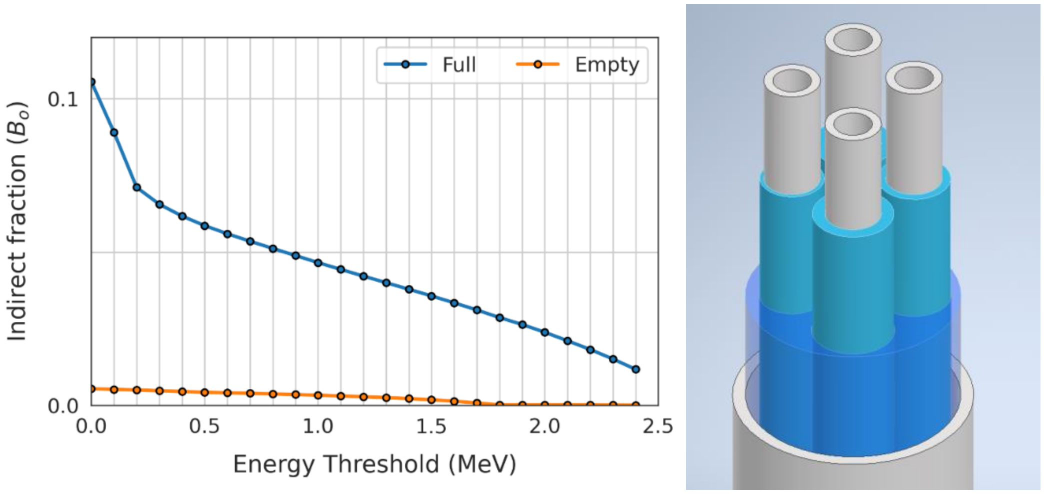

Figure 4.1.10: Scatter fraction (left) for tube array object(right). The transparent blue represents a variable void fraction insert, the solid blue is the plastic film, and the grey is steel.

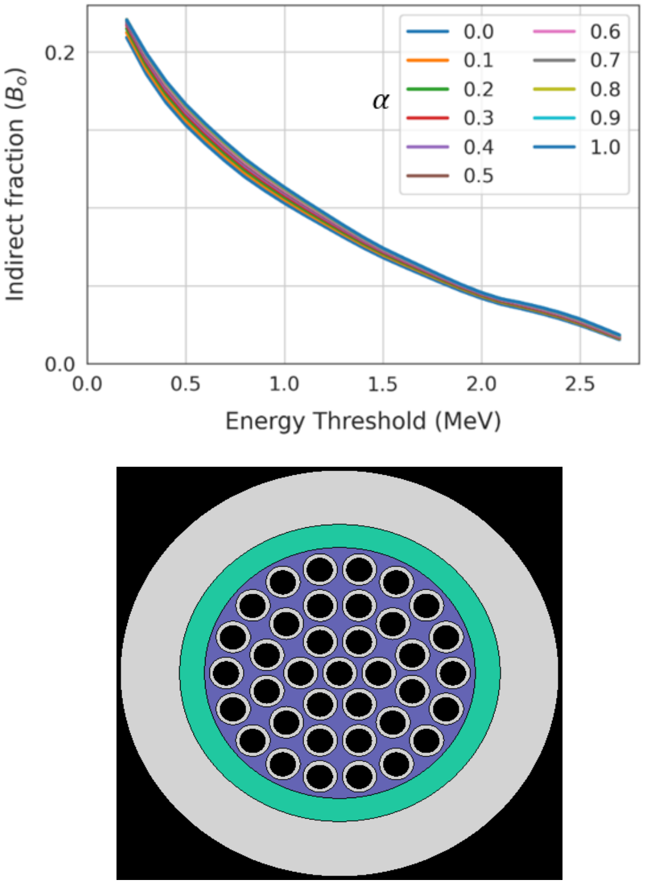

Figure 4.1.11: Scatter fraction (top) for CANDU 37-element bundle (bottom).

4.1.1.3 Energy threshold selection

To identify the magnitude of the scattering count correction an energy threshold must be selected. The simplest metric is to eliminate the Bremsstrahlung radiation generated by the accelerating deuterium ion beam, which can reach a maximum value of 160 – 180 keV. Since the plastic scintillator measures the Compton edge of photon radiation the light output of the Compton edge should be filtered out. The Compton edge for the 180 keV radiation is 74 keV which generates ~740 photons. This light emission is equivalent to a ~ 0.5 MeV neutron energy cut-off based on the light emission plot for the EJ200 (Figure 3.2.4). However it should be noted that a) this radiation spectrum will be peaked at a lower energy (as discussed in section

3.2.2.1) and b) the Bremsstrahlung radiation can be shielded with thin lead shielding, as was done by [129]. However, this initial selection of a lower energy cut-off of 0.5 MeV is chosen to eliminate all Bremsstrahlung radiation from contributing to the measurement signal. A threshold of 0.5 MeV for the primary testing facility at McMaster provides an ambient background scatter correction of 0.3 and the graphs provided in the previous section provide the object-dependent corrections.

4.1.2 Crosstalk

Crosstalk is caused by a neutron scattering from one scintillator element and interacting in another (Figure 4.1.12).

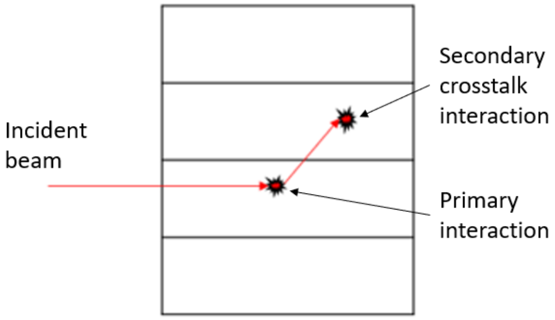

Figure 4.1.12: Crosstalk mechanism

The crosstalk count fraction is an important parameter to quantify since it spreads counts over multiple pixels, increasing the baseline count rates in the detectors. To explore the crosstalk fundamentals, three adjacent pixels are used as an example to understand the effect on the measured attenuation profile. In this example, the response of the central pixel (pixel 2) to crosstalk counts from adjacent pixels is analyzed (Figure 4.1.13).

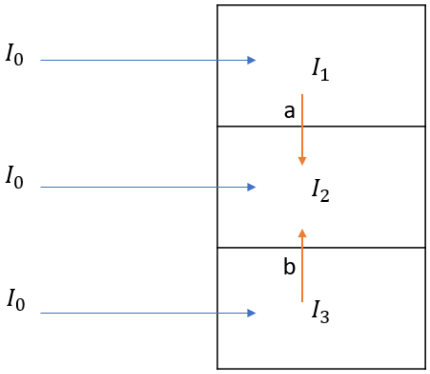

Figure 4.1.13: Example crosstalk scenario. Pixel 2 is labelled with the counts, I_2. The variables a and b represent fractions of counts leaving pixel 1 and pixel 3, respectively.

The expression for the number of counts in pixel 2 for the unattenuated and attenuated case is a summation of the counts from all pixels:

$$I_2 = I_0 + aI_0 + bI_0 \qquad \text{(flat)}$$

$$I_{2T} = T_2 I_0 + aT_1 I_0 + bT_3 I_0 \qquad \text{(object)}$$

With T_x representing the transmission fraction due to an object in between the source and detector for a given pixel, a and b representing the crosstalk fraction of pixels 1 and 3 into pixel 2, and I_2 and I_{2T} the total direct source and attenuated counts in pixel 2. The attenuation is given by the negative logarithm of the ratio of the attenuated counts to the flat field counts:

$$A_{ideal} = -\ln\left(\frac{I_{2T}}{I_2}\right)_{a=0,b=0} = -\ln\left(T_2\right)$$

$$A_{xtalk} = -\ln\left(\frac{I_{2T}}{I_2}\right) = -\ln(T_2) - \ln\left(\frac{1 + a\frac{T_1}{T_2} + b\frac{T_3}{T_2}}{1 + a + b}\right)$$

Therefore, the crosstalk acts to alter the attenuation value measured by the system and is dependent on surrounding transmission values as well as the crosstalk fractions. This simple example highlights some important points:

- Flat-field and object field counts are not influenced in the same way; the object-field crosstalk count rate is influenced by the object attenuation profile, since it is dependent on the number of counts entering adjacent pixels.
- In regions where transmission in adjacent pixels is similar, the crosstalk does not affect the attenuation measurement significantly. Such cases exist for materially uniform regions in test phantoms, such as the central region of a square or cylindrical water phantom.
- Since counts are shared amongst adjacent pixels, the crosstalk percentages act to “smudge” transmission differences over several pixels. In essence the crosstalk response is like a convolution-type operation on the detector count distribution for a given acquisition and tends to filter large attenuation differences and reduce large differences in transmission (attenuation).

Hence if the crosstalk percentage is large it will act to reduce the system contrast between transmission gradients. Therefore, the crosstalk is quantified in the next section via simulation to ensure that sharp attenuation gradients can be maintained. Since the detector size and material composition are already determined an energy threshold is the primary method of reducing crosstalk.

4.1.2.1 Crosstalk simulation

To determine the detector crosstalk percentages, an MCNP6 simulation of an 8x8 scintillator array was generated. The simulation uses a square plane neutron source approximately the size of a pixel as direct source of neutrons over a single pixel in the central region of the array (Figure 4.1.14).

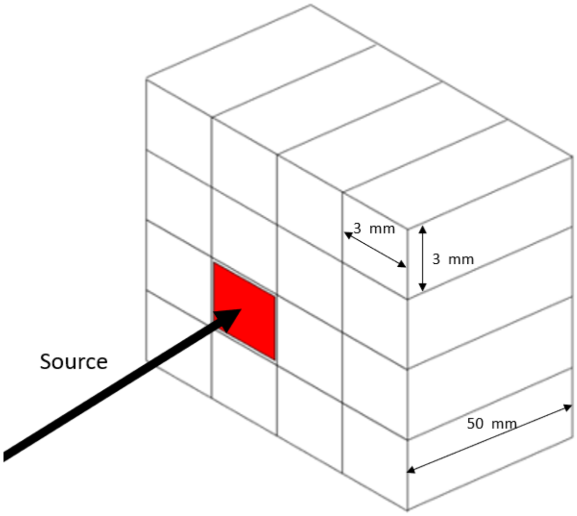

Figure 4.1.14: crosstalk model layout showing the crosstalk physics. A 4x4 array is shown as an example (the real array is 8x8).

This is analogous to the experimental procedure to determine the crosstalk for an X-ray system outlined in [130] in which all detectors except one are covered to determine the counts in adjacent detectors. The PTRAC method in MCNP6 provides particle trajectory tracking–location, energy loss, and direction changes–for each pixel of the scintillator. For more information, see the MCNP6 manual [131]. A custom Python data processing script was developed to process the interaction information for each particle trajectory and each pixel. The script tracks each particle lifetime in the output PTRAC file and adds a count for a given pixel if the interaction is within the pixel boundary and the deposited energy is above a selected threshold. After 10^6 direct particles, the number of counts in adjacent pixels was determined as a fraction of the direct pixel counts that occurred in the primary pixel. A process diagram is shown in Figure 4.1.15.

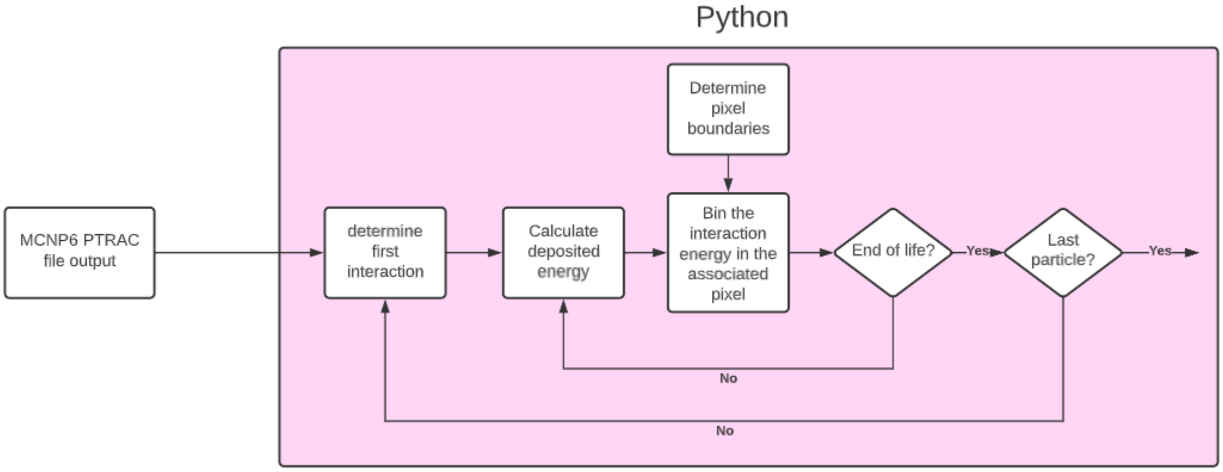

Figure 4.1.15: Crosstalk fraction calculation process flow.

The resulting heatmap (Figure 4.1.16) displays a highly symmetric distribution of crosstalk, which is expected due to the symmetric nature of the neutron-proton scatter reaction. A crosstalk response is determined for no threshold energy, as well as threshold energies of 0.5 MeV, 0.7 MeV, 1.5 MeV, and 2.0 MeV along a row as well as along a diagonal (Figure 4.1.17). As expected, the crosstalk fraction decreases with increasing energy threshold, but decreases at a slower rate as the threshold is increased.

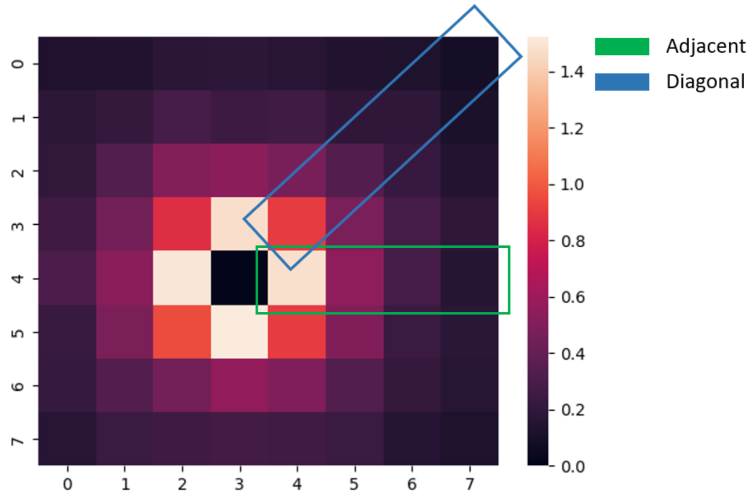

Figure 4.1.16: Crosstalk heatmap (percentages) for a 0.7 MeV energy cutoff.

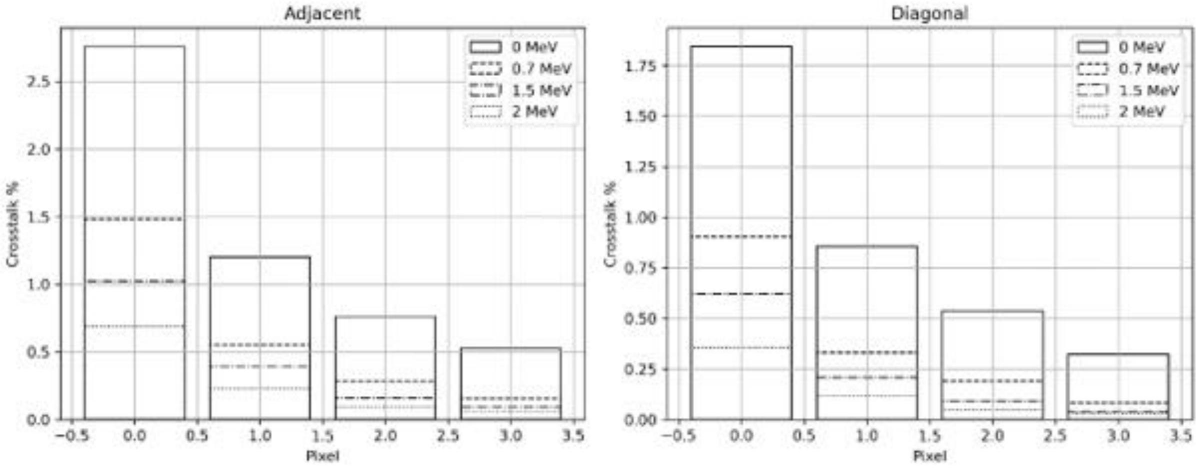

Figure 4.1.17: Crosstalk percentage at different cutoff energies.

A crosstalk convolutional kernel can be generated from the heatmap (Figure 4.1.18) and applied to ideal projection count data (for flat-field and object-field). This convolution operation updates each pixel count with contributions from adjacent pixels due to crosstalk from which the crosstalk version of the attenuation profile can be calculated.

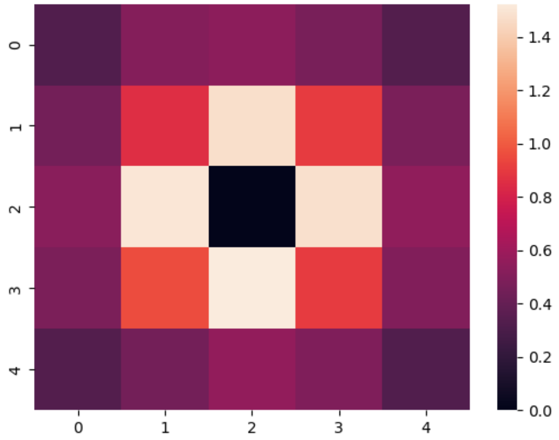

Figure 4.1.18: Crosstalk convolution kernel for simulation (0.7 MeV cutoff example). Heatmap in %.

Given the nature of crosstalk to distribute counts among adjacent pixels ("spreads out" the counts), it seems that it would have a similar effect to a convolution operation. Therefore, that the attenuation profile would be blurred to some degree and therefore the resolution may be impacted. This effect is explored using a representative block phantom and CANDU phantom attenuation profile and applying the crosstalk kernel to count distributions generated in MATLAB. The influence of crosstalk for these phantoms are shown in Figure 4.1.19 and Figure 4.1.20. The effect of crosstalk on the block attenuation profile is only apparent at the edges, which is expected given the crosstalk mechanism discussed at the beginning of this section. In essence the crosstalk effect is adding a minor blurring to the edges, and therefore some resolution degradation is expected in the reconstruction. The CANDU channel profile shows the effect that crosstalk has on high gradient regions. However, since the threshold is set to 0.5 MeV the effect is not large, and therefore it is expected that crosstalk will have a negligible influence on void prediction.

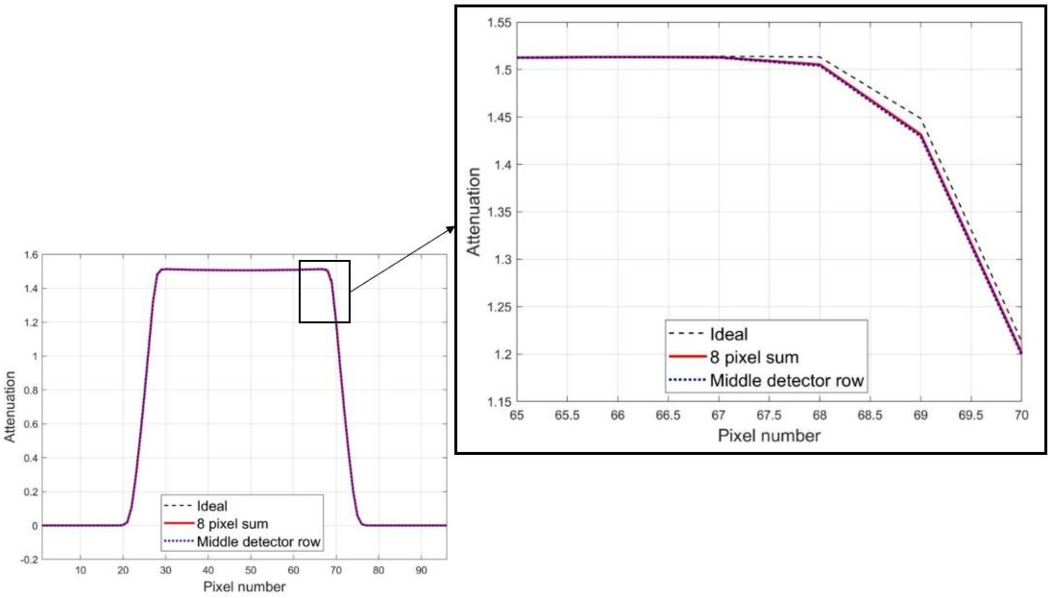

Figure 4.1.19: Crosstalk effect on simple block geometry attenuation profile.

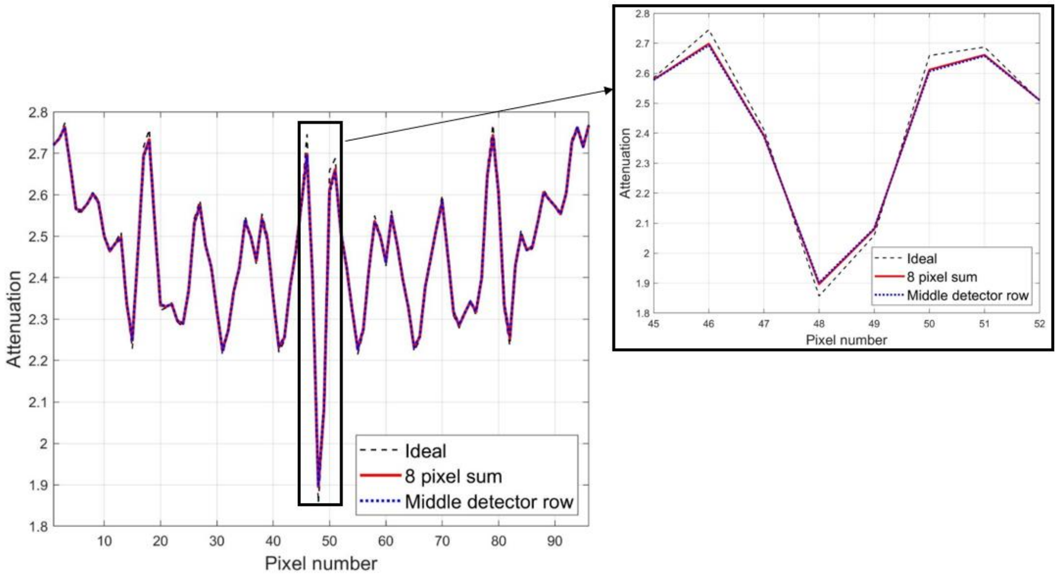

Figure 4.1.20: Crosstalk effect on 37-element CANDU bundle geometry attenuation profile.

However, the crosstalk fraction is object dependent and is difficult to measure in-situ for neutron systems and therefore the degradation of resolution cannot be determined easily in practice. The theoretical resolution was determined here using the ESF of the square block phantom under no-noise conditions. Multiple lines for each edge were taken and averaged to determine the resolution (Figure 4.1.21).

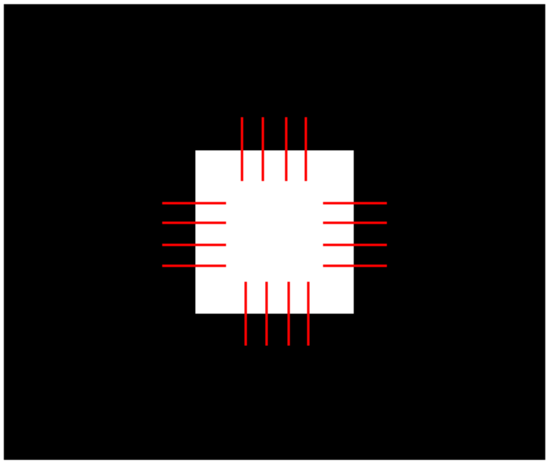

Figure 4.1.21: Example of ESF measurements. Example line segments are shown as red. All lines are averaged together to produce an average ESF function to evaluate the resolution.

Different levels of detector energy threshold were implemented, and the results show that the crosstalk fraction increases the resolution value by approximately 0.2 mm above the selected threshold of 0.5 MeV. Therefore, no significant impact on system performance is expected.

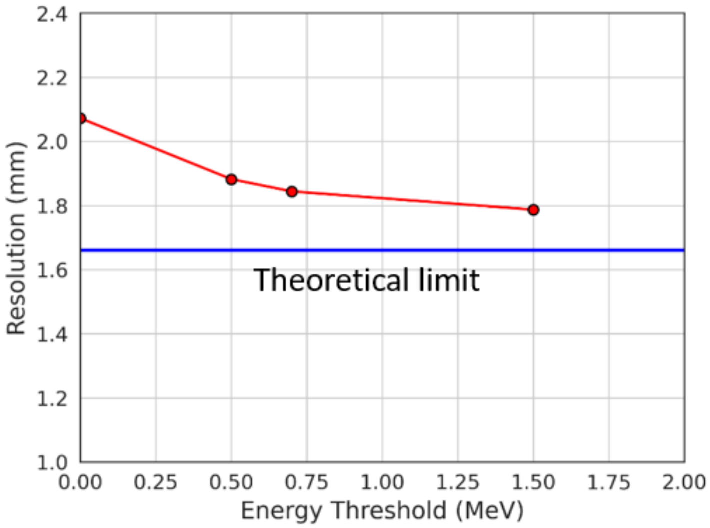

Figure 4.1.22: Resolution degradation caused by crosstalk.

4.1.2.2 Overall consequences of noise counts

The crosstalk acts to increase the blurring (reduce resolution) from 1.67 mm to about 1.87 mm. In addition to resolution impacts, high levels of crosstalk act to reduce contrast between transmission values due to the "smearing" of counts into adjacent pixels. Since the crosstalk fractions are based primarily on the scintillator material and geometry, the maximum crosstalk fraction for this system is defined by the energy cut-off[3]. For detector energy thresholds of concern here, the crosstalk effect is small.

The object background counts, B_{obj}, are a function of object material and geometry, and cannot be measured in-situ. As discussed, the object scatter parameter only impacts the object count rates, and the effect on the attenuation profile is to reduce contrast and, if the object background fraction is high enough, can even produce

---

[3] Crosstalk can also increase if different scintillator geometry is used, such as larger thickness or pixel dimensions or a different source energy is used.

negative attenuation values (Figure 4.1.23). The object scatter parameter must be calculated by simulation for a given test geometry and correction factors calculated.

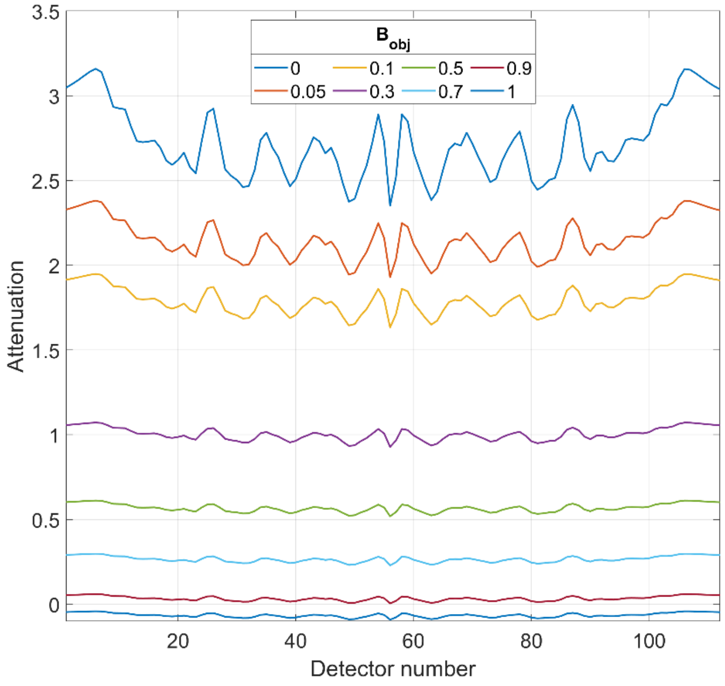

Figure 4.1.23: Effect of increasing object background fraction on attenuation distribution.

The background fraction acts to reduce the contrast between the object measurement and flat-field count, which in turn reduces contrast between adjacent detectors (Figure 4.1.24). As shown in Figure 4.1.24, even at low levels of $B = 0.05$, the background field will have a large impact on the sinogram if not corrected.

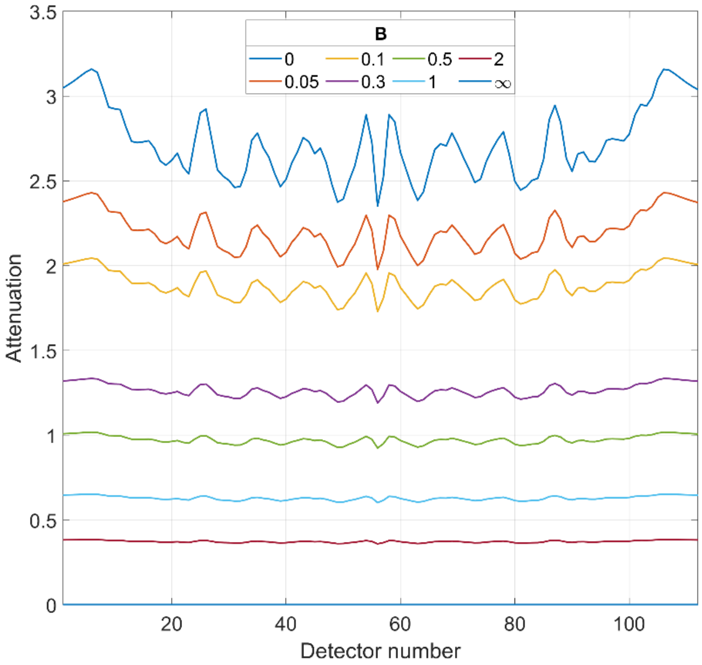

Figure 4.1.24: Effect of increasing background fraction on attenuation distribution.

The background fractions can reach up to a fraction of 0.3 of the direct counts for a detector energy threshold of 0.5 MeV for this system but can be calculated or measured and used to correct the count data to some degree using a flat field, as follows:

- Measure or simulate the background fraction and object background fraction for a given configuration
- Simulate the crosstalk for a flat-field measurement
- Use the background fraction and crosstalk fraction to get the true direct count rate I_0:

$$I_0 = \frac{I}{1 + B + X_0}$$

- Using this I_0, the corrected measured count TI_0 can be calculated from the measured count, I_T, giving the correct transmission signal:

$$TI_0 = I_T - BI_0 - B_{obj}I_0 - X_T I_0$$

The next section uses the crosstalk fraction derived in this section to determine the void fraction prediction capabilities of the system. A converged, or no-noise, case is highlighted to determine the ultimate prediction performance and afterward Poisson noise is added to show the effect of the stochastic nature of the source. The section concludes by providing some qualitative analysis on transient void prediction and the applicability of the system to short scan time scenarios.

4.1.3 Void fraction case study

The measurement of the subchannel void fraction distribution is the primary end-use application of the FNCTS. As such the ability to measure the void distribution accurately is imperative. Unfortunately, the driving force behind this thesis – *provide subchannel void information for code validation and improved mechanistic understanding of bundle void fraction distribution phenomena* – means that the high-resolution void fraction phase distribution (liquid films, gas core void fractions, etc.) measurements do not exist to provide a template for a realistic phase distribution within a bundle geometry. Therefore, a representative test case is used to quantify the expected functionality of the FNCTS and provide insight into the potential measurement limitations.

The void fraction measurement model was developed in MATLAB using the crosstalk model derived in the previous section with additive Poisson noise to account for stochastic effects. The process is as follows:

1. Object generation: The representative CANDU object of interest was chosen to include annular flow structural features. The profile consists of randomly

distributed void fractions within the core of each subchannel (void fractions of 0.5 – 1.0) and liquid films thicknesses that are chosen randomly for each of the pins and outer surface (Figure 4.1.25).

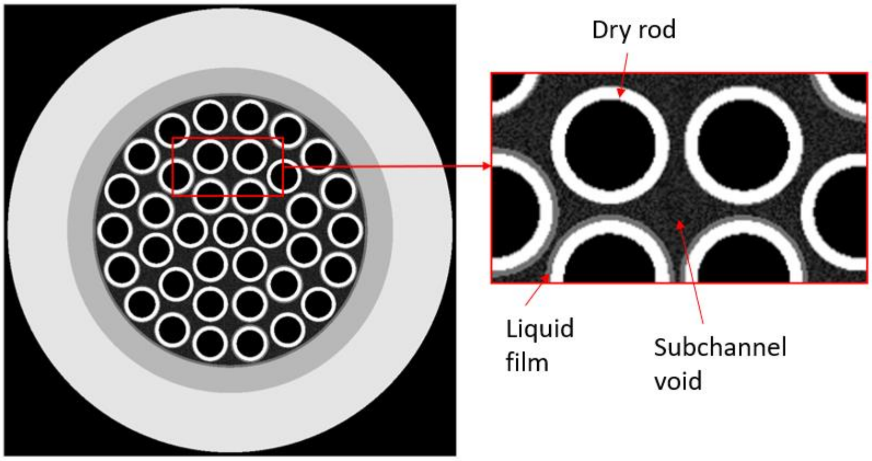

Figure 4.1.25: Representative test case (left) and zoom in on the subchannels showing the void fluctuation pattern within the central core regions.

2. <u>Sinogram generation</u>: Initial counts for each pixel were generated using a projection matrix developed as part of the AIRTools II toolbox [105]. The projection matrix is generated using a ray tracing algorithm that calculates the intersection of a ray-line from the source with each of the square pixels in the image domain. The fraction of the ray-line that intersects a discretized image domain pixel determines the fraction of attenuation caused by that location (see section 3.1.4.2).
3. <u>Application of Poisson and cross talk</u>: Poisson noise is added to the count distribution of the object attenuation and flat field counts. Afterward the crosstalk kernel is used to generate the crosstalk count distributions, and the noisy sinogram is obtained using equation 4.1.3.
4. <u>Reconstruct image:</u> the SART reconstruction algorithm is used to reconstruct the image using the noisy sinogram.

5. Subchannel void fraction calculation: The subchannel averaged void fraction is calculated for each subchannel by using a binary masking on the pin structures and outer boundaries of the subchannel (everything inside the pin was omitted from the subchannel void calculation). Due to the circular structure of the pins and the discretization of the image reconstruction domain, some pixel information may be omitted, leading to slight deviations in void prediction. An example of the circular masking is shown in Figure 4.1.26, showing the imperfect discretization of the binary mask on circular structures.
6. Repeat steps 3 – 5 100 times for a given image: This process is repeated for a given object 100 times to obtain the subchannel void fraction prediction and error spread due to the counting noise effect on the reconstruction process (every time a projection measurement is taken, it would provide a different number of counts in a detector due to stochastic noise). Each subchannel void fraction for a given ring (Figure 4.1.26) is calculated for each of the 100 reconstructions of the sample. All 100 samples are then averaged to determine the true mean estimate of the subchannel void average. The errors in the subchannel void fraction predictions are given by the standard deviation of the 100 data points and the rms and average errors of the subchannel void predictions are calculated to determine the accuracy of the ensemble average prediction (where α_i is the true mean estimate of the subchannel averaged void fraction and $\bar{\alpha}$ is the actual subchannel averaged void fraction value):

$$\alpha_{RMS} = \sqrt{\frac{1}{N}\sum^{N}(\alpha_i - \bar{\alpha})^2} \qquad (4.1.4)$$

$$\alpha_{avg} = \frac{1}{N}\sum^{N}(\alpha_i - \bar{\alpha}) \qquad (4.1.5)$$

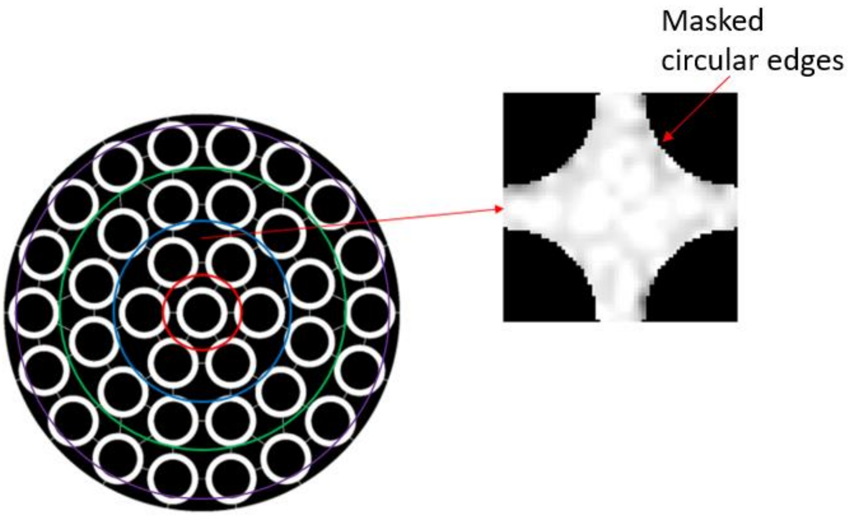

Figure 4.1.26: CANDU subchannel diagram with example subchannel. Rings colours indicate different subchannel rings.

This process is repeated for 10 random two-phase flow distributions, for a total of 600 data points (60 subchannel estimates multiplied by 10 samples). It is assumed in this analysis that the obtained counts are corrected for ambient and object scatter and that the baseline scans for an empty and full test section had long scan times and thus contributed negligible noise to the void fraction values. A flow diagram of the data processing is shown in Figure 4.1.27.

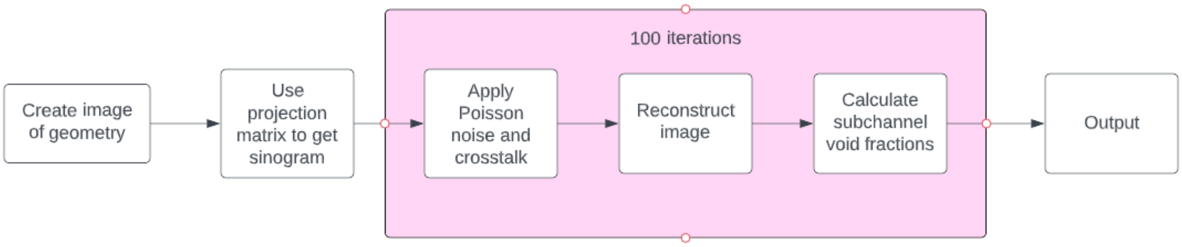

Figure 4.1.27: flow diagram for each void prediction simulation.

The ideal reconstruction case with no statistical noise (but with crosstalk) provides the achievable predictive capability of the current system in the limit of maximum scan time (Figure 4.1.28 and Figure 4.1.29). The prediction is not exact owing to cutting off pixels due to binary masking that uses square pixels (such that liquid film structures are left out of the void fraction calculation while masking the circular pins in the domain), as well as crosstalk effects. Such masking can be improved by using more adaptive meshes, such as the method used by Le Corre [65], but is beyond the scope of the work covered here. Nonetheless the ideal circumstance provides good prediction accuracy of the subchannel averaged void fraction.

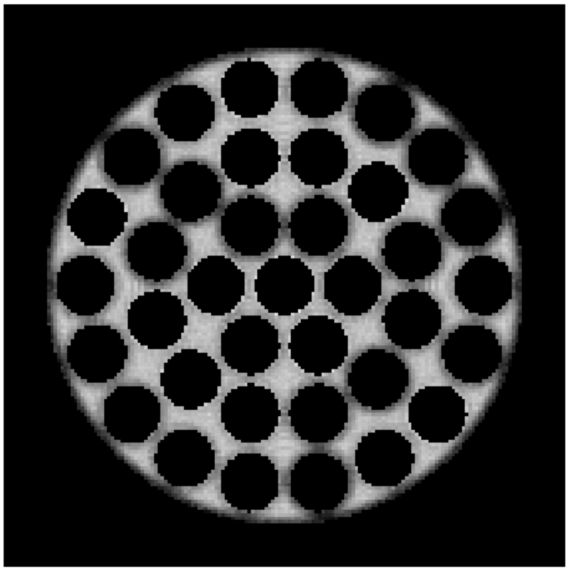

Figure 4.1.28: Ideal reconstruction.

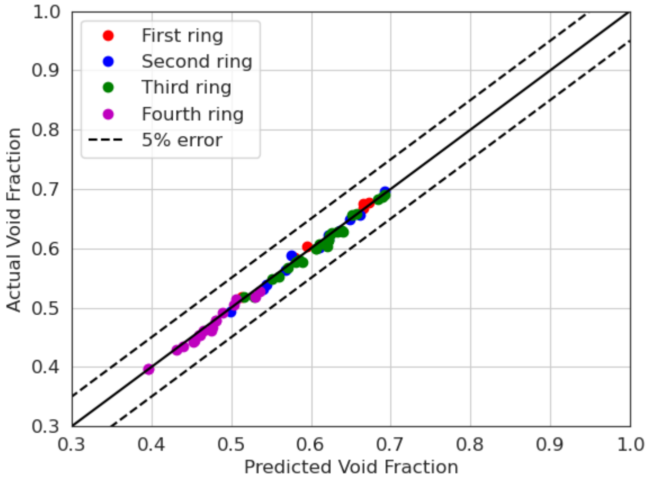

RMS error	0.007
Average error	0.003

Figure 4.1.29: Ideal reconstruction subchannel averaged void fraction prediction accuracy.

4.1.3.1 Scan Time

Ultimately the error propagation in tomography is a great deal more complex than a standard densitometry measurement since each pixel value estimate in a CT image reconstruction is necessarily correlated to another. However, the errors present in densitometry can be used to develop a simple method of reducing the noise level in CT reconstructions. Using the uncertainty expression of a densitometry measurement helps determine which factors minimize the errors in individual pixel measurements. The expression for the error for a densitometry void measurement – assuming that the full liquid and full gas calibration values are known with minimal uncertainty, i.e., long scan times – is reiterated here for convenience:

$$\frac{\sigma_\alpha}{\alpha} = \frac{1}{\ln\left(\frac{I_\phi}{I_l}\right)}\sqrt{\frac{1}{tI_\phi}} \tag{4.1.5}$$

This means that one would want to maximize the number of two-phase counts, which means getting a stronger source, scanning for a longer period, or using more efficient detectors. Unfortunately scanning 2-phase flow phenomena, particularly at or near CHF, imposes a significant time constraint for imaging (for practical reasons, such as holding a complex experiment steady, scan times of < 30 minutes are desired). The number of counts measured in each detector is given by:

$$N_d = t\frac{I_s}{4\pi}\frac{A_{\text{det}}}{r^2}\eta T \tag{4.1.6}$$

Where N_d is the number of detector counts, I_s is the total source emission in neutrons per second, A_{det} is the detector pixel area in mm^2, r is the source to detector distance in mm, η is the detector efficiency, and T is the fraction of neutrons transmitted through the object. Therefore, to increase counts within a fixed time interval for the existing 8x8 detector array, the pixels can be grouped together in the column-wise direction (axially along the test section) to provide an increased detector area (larger solid angle). While this grouping procedure collapses 3-dimensional information in the reconstruction, within the span of 8 pixels (8x3 mm = 24 mm) the expected void changes are expected to be small (except for areas near a spacer). Therefore, the grouping is expected to increase the count rates by a factor of 8. An additional improvement can also be realized by increasing the per-projection scan time by reducing the total number of projection angles with total scan time held constant, as outlined below.

Number of projection angles

Three angular intervals were tested over $360°$: 1°, 2°, and 4°, corresponding to 360, 180, and 90 total angles. Given that the scan time is fixed this represents an increase in per-projection scan time by a factor of 2 – 4 times. The minimum number of angles was limited to 90 (angular intervals of 4°) since it was found that the reconstructions generated with courser angular intervals started to develop significant artifacts and void measurements were therefore non-physical. The reconstruction domain information for each reconstruction is shown in Table 2. For each case the reconstruction domain pixel number was chosen based upon trial and error through a systematic process of lowering the reconstruction domain pixels until the masking effectiveness diminished. The reconstruction domain in the 90-angle reconstruction case was upscaled using a bilinear interpolation method to match the pixel resolution of the 180-angle case to improve the masking accuracy.

Table 2: reconstruction domain information

Number of angles	Reconstruction domain	Image pixel resolution	Projection scan time (s)
360	168x168	0.7 mm/pixel	5
180	120x120	1 mm/pixel	10
90	120x120 (original 90x90)	1 mm/pixel	20

A single random void distribution sample is chosen to highlight the comparison of the single pixel prediction test (shown in Figure 4.1.35) and the comparison for 8-pixel summation, or axial averaged, case (shown in Figure 4.1.38). These plots show that the 90-angle reconstructions can provide comparable subchannel averaged void fraction predictions in the 8-pixel summation case (Figure 4.1.38), and superior predictions in the single pixel case (Figure 4.1.35), due to the ability to use longer scan times per-projection which reduce the stochastic noise. This is evident when comparing the RMS errors in Figure 4.1.30 and Figure 4.1.31. However, in the single detector pixel acquisition, the 90-angle case has slightly higher relative standard deviation (Figure 4.1.32) leading to slightly larger measurement uncertainty, but does not exhibit the underprediction bias that is present in the 360 angle and 180 angle acquisitions.

The underprediction bias that appears in the 360 angle and 180 angle acquisitions in Figure 4.1.35 is a consequence of thresholding void fraction values to physically realistic values (between 0 and 1) with statistical noise variations present in the image. Figure 4.1.35 and Figure 4.1.38 seems to indicate that the onset of the bias may be a function of scan time since the effect disappears after a per projection scan time of 20 s in the 90 angle acquisition. An in-situ measurement metric to identify the minimum scan time necessary to avoid the void fraction prediction bias before a full measurement is taken would provide a simple and useful tool. A simulation procedure was used to develop a metric for in-situ analysis through the repeated measurement of a single projection. By taking multiple projection measurements at the same projection angle (in this case 0°), the variance in the attenuation data for the single projection angle can be calculated and related to the onset of the void prediction bias in the data. The maximum normalized standard deviation in the measured projection data, $\max((\sigma/\mu)_i)$, is chosen as the metric (to determine the greatest noise contribution), where σ is the standard deviation of the projection measurement and μ is the average of the projection measurements for each of the i detectors. The simulation process is as follows:

1. Generate a random void distribution.
2. Take a single projection with added Poisson and crosstalk noise.
3. Repeat the projection 10 times at the same angle (resample the Poisson and crosstalk noise)
4. Take the normalized standard deviation (σ/μ) of the 10 samples for each of the 112 detectors. For example, the data is represented as a matrix with rows representing the number of detectors and columns representing the sample number, and the standard deviation and the mean is calculated across each row and a new normalized standard deviation vector is created.
5. Take the maximum of the normalized standard deviation vector.

6. Repeat for each generated void distribution.

This process was simulated for 10 randomly generated void distributions and the results are shown in Figure 4.1.33. Figure 4.1.35 indicates that the 90-angle case (20 seconds per projection) is when the bias starts to minimize and thus is used as a scan time reference. This provides a minimum required per-projection scan time of 20 s in this example. Therefore, the maximum normalized standard deviation measurement from a measured sinogram would have to be less than 0.04 for the void fraction bias to be minimized. This measurement can be taken in-situ before a full scan to ensure that the void bias will not be present in the data.

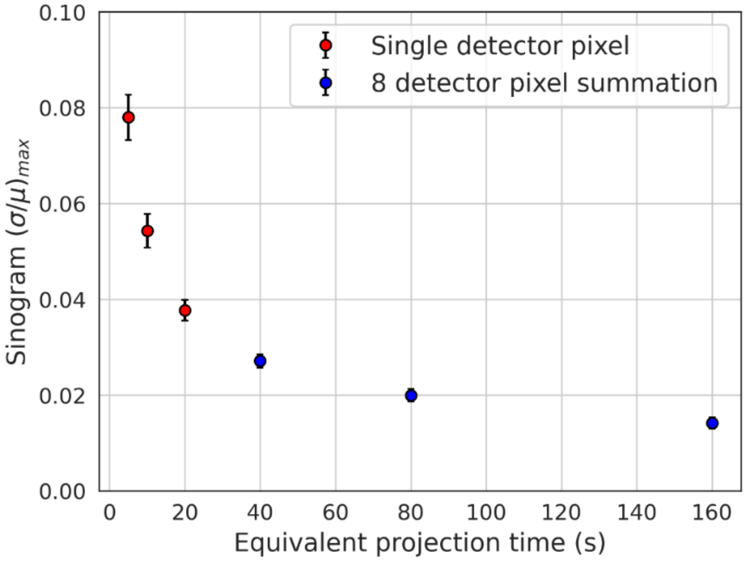

Figure 4.1.33: Sinogram normalized standard deviation measurement scan time dependence. Equivalent scan time is used to demonstrate that by combining 8 detector pixels would have the same effect on count rates as increasing the scan time by 8 times (it scales detector area instead of time in equation 4.1. **6. For example, combining 8 pixels during a 5 second projection time would have an equivalent projection time of 40 seconds.**

In the 8-detector pixel summation case, the bias is not realized since combining detectors effectively increases the count rate by 8 times. The standard deviations are similar for each of the cases, but the 90-angle case has a greater RMS error in some subchannel cases (Figure 4.1.34). This could be due to greater information for reconstruction in the 360 angle case resulting in more accurate reconstructions. Therefore, in the case of a constant 30-minute total scan time, 360 angles would be preferable when combining pixels as it provides the least RMS errors, but 90 and 180 angular interval acquisitions can also provide similar RMS errors and relative standard deviations if 360 angular interval acquisitions are not possible.

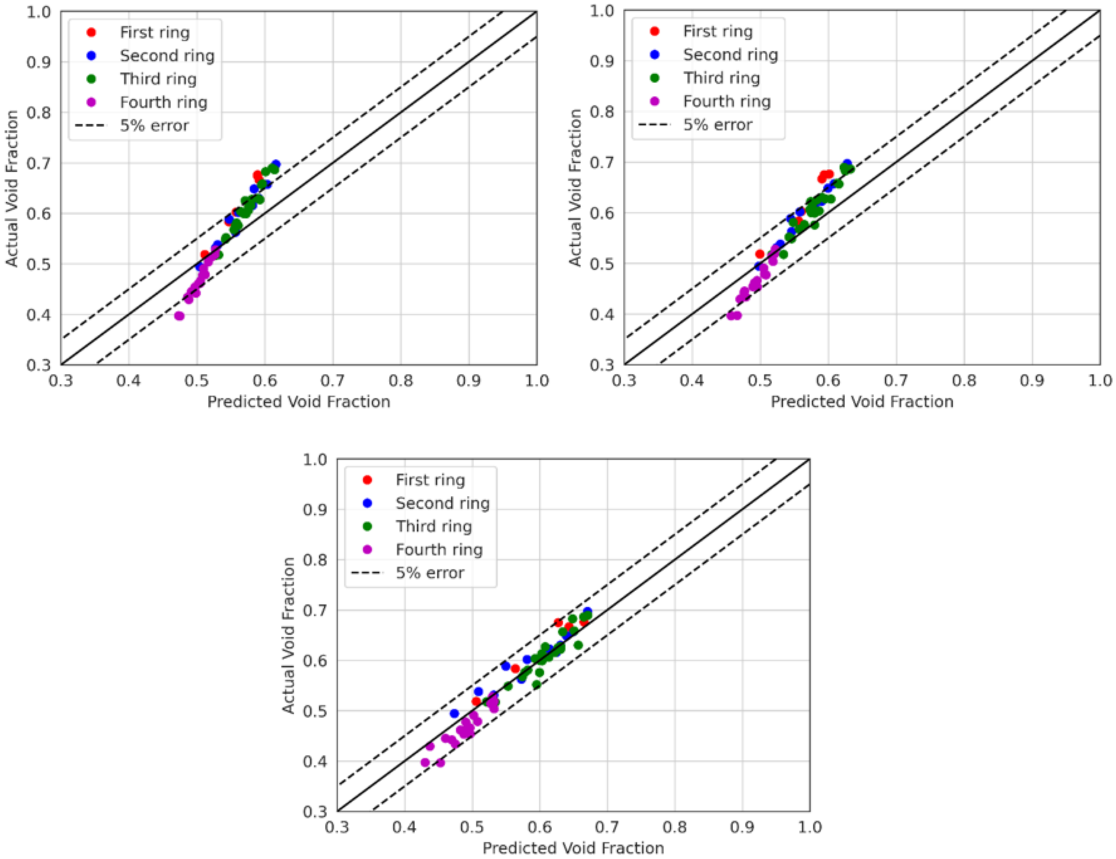

Number of Angles	360	180	90
RMS error	0.046	0.038	0.022
Average error	-0.015	-0.015	0.003

Figure 4.1.35: single detector row scans (3 x 3 mm^2 detector area): 360 angle with 5 s projection scans (top left), 180 angle with 10 s projection scans (top right), and 90 angle 20 s projection scan (bottom). A single random object sample is shown to display general trends on a ring basis more clearly.

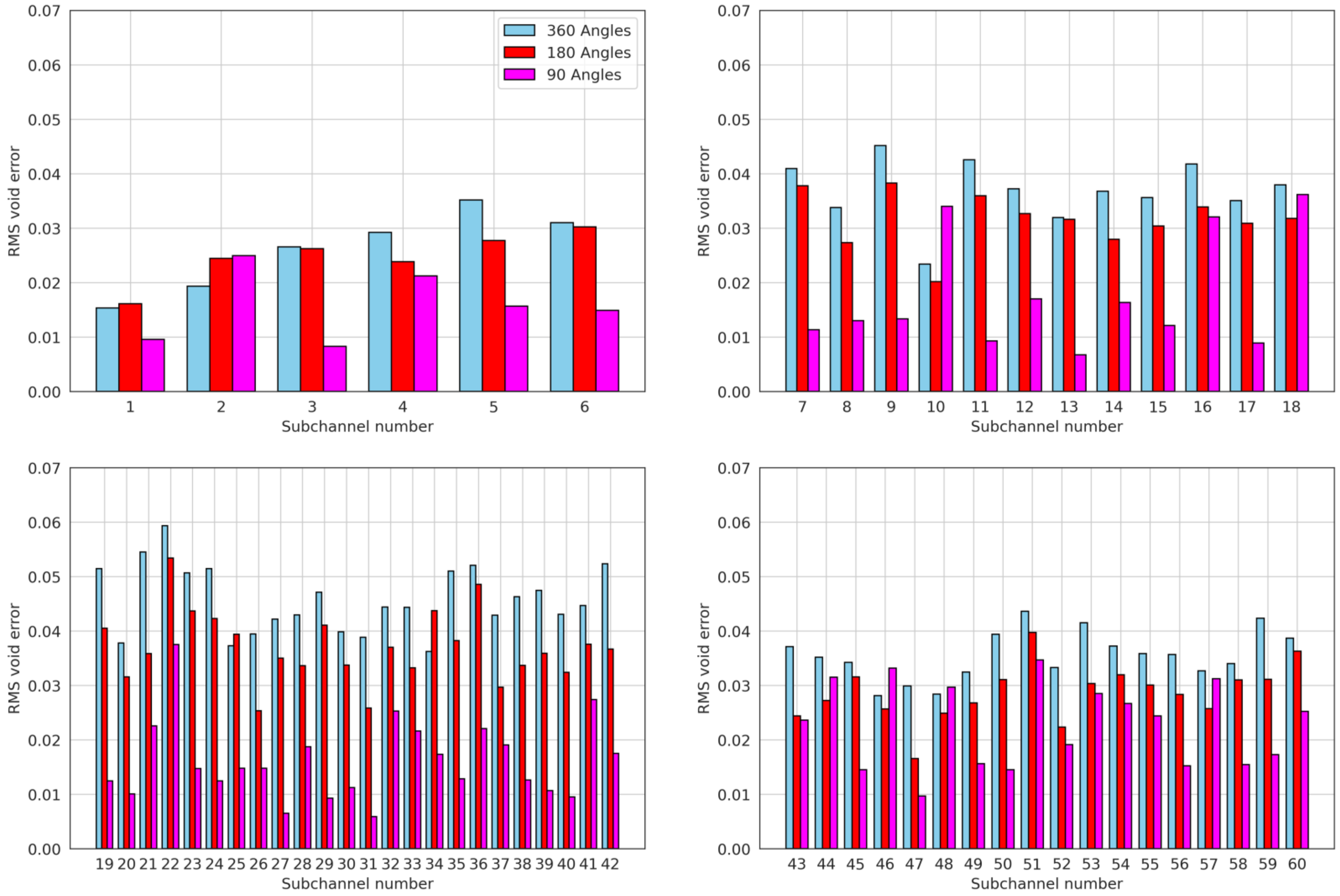

Figure 4.1.36: Void RMS errors for each subchannel (with reference to Figure 4.1.41) for single detector row scans (3 x 3 mm^2 detector area). RMS errors are lower in the 90 angle case compared to the 360 and 180 angle cases for the majority of subchannels.

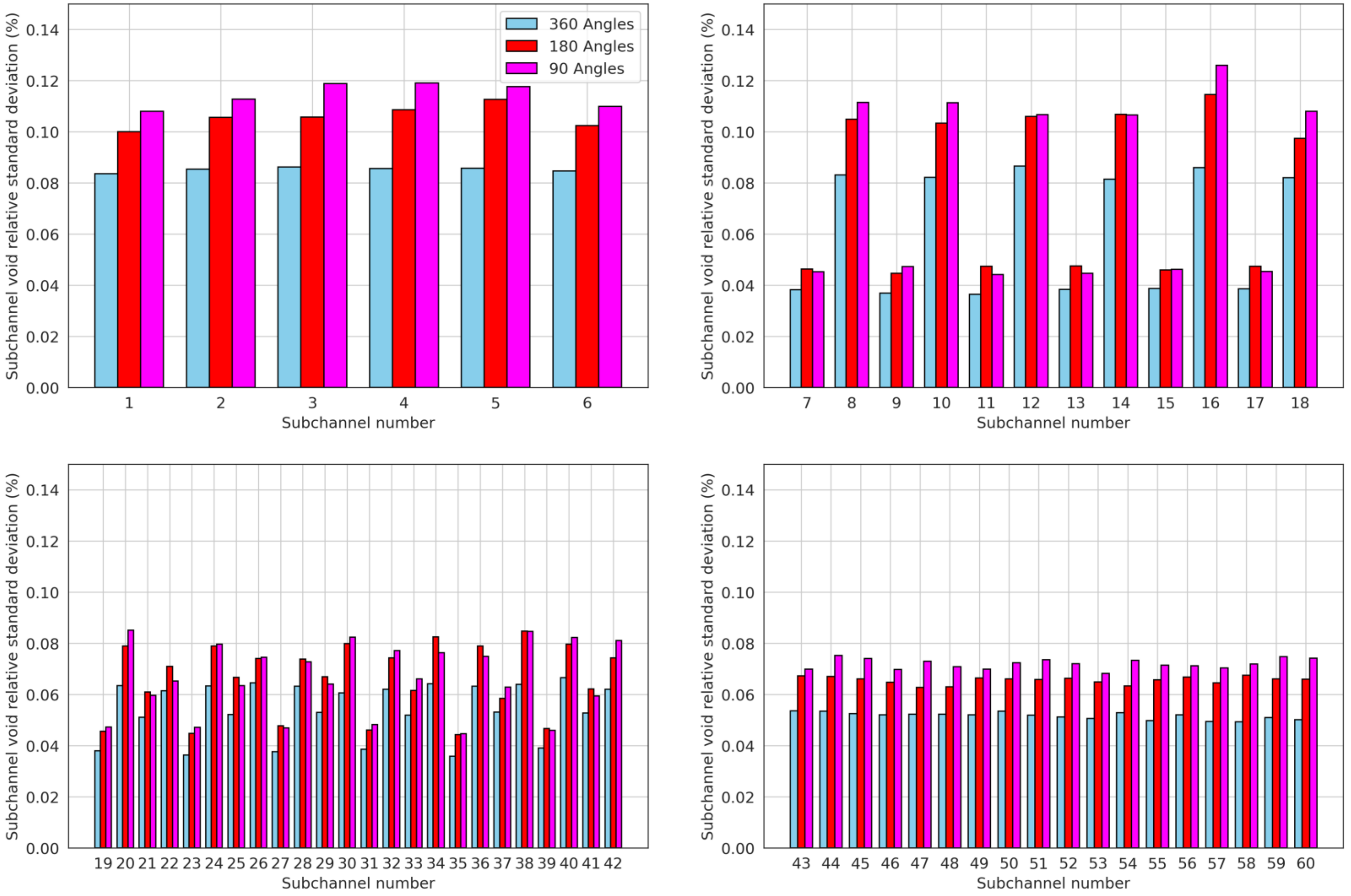

Figure 4.1.37: Void relative standard deviation for each subchannel (with reference to Figure 4.1.41) prediction for single detector row scans (3 x 3 mm^2 detector area). The standard deviation represents the spread in the prediction of void fraction and is lower in the 360

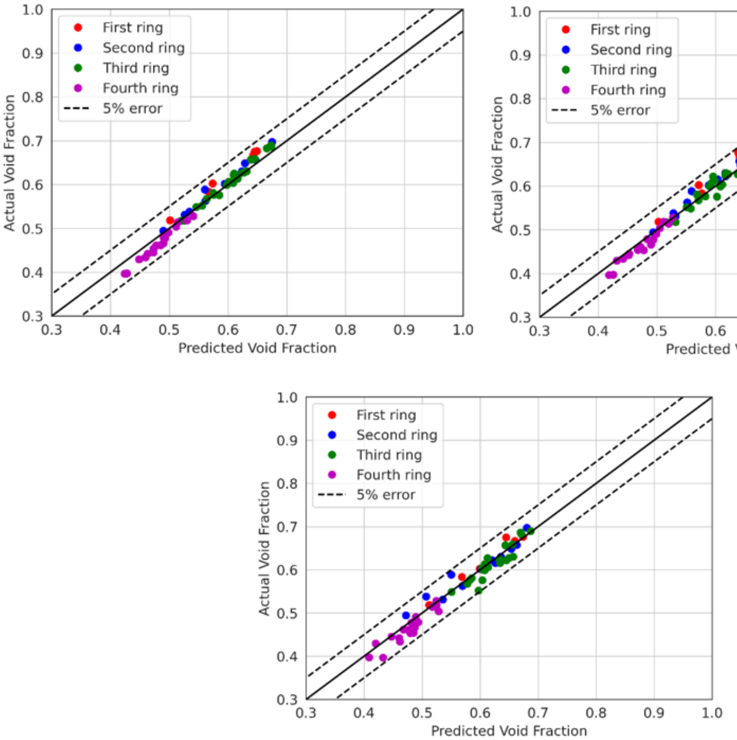

Number of Angles	**360**	**180**	**90**
RMS error	0.016	0.015	0.017
Average error	-0.001	-0.003	0.004

Figure 4.1.38: summed pixel scans (8 x 3 x 3 = 72 mm^2 detector area): 360 angle with 5 s projection scans (top left), 180 angle with 10 s projection scans (top right), and 90 angle 20 s projection scan (bottom). A single random object sample is shown to display general trends on a ring basis more clearly.

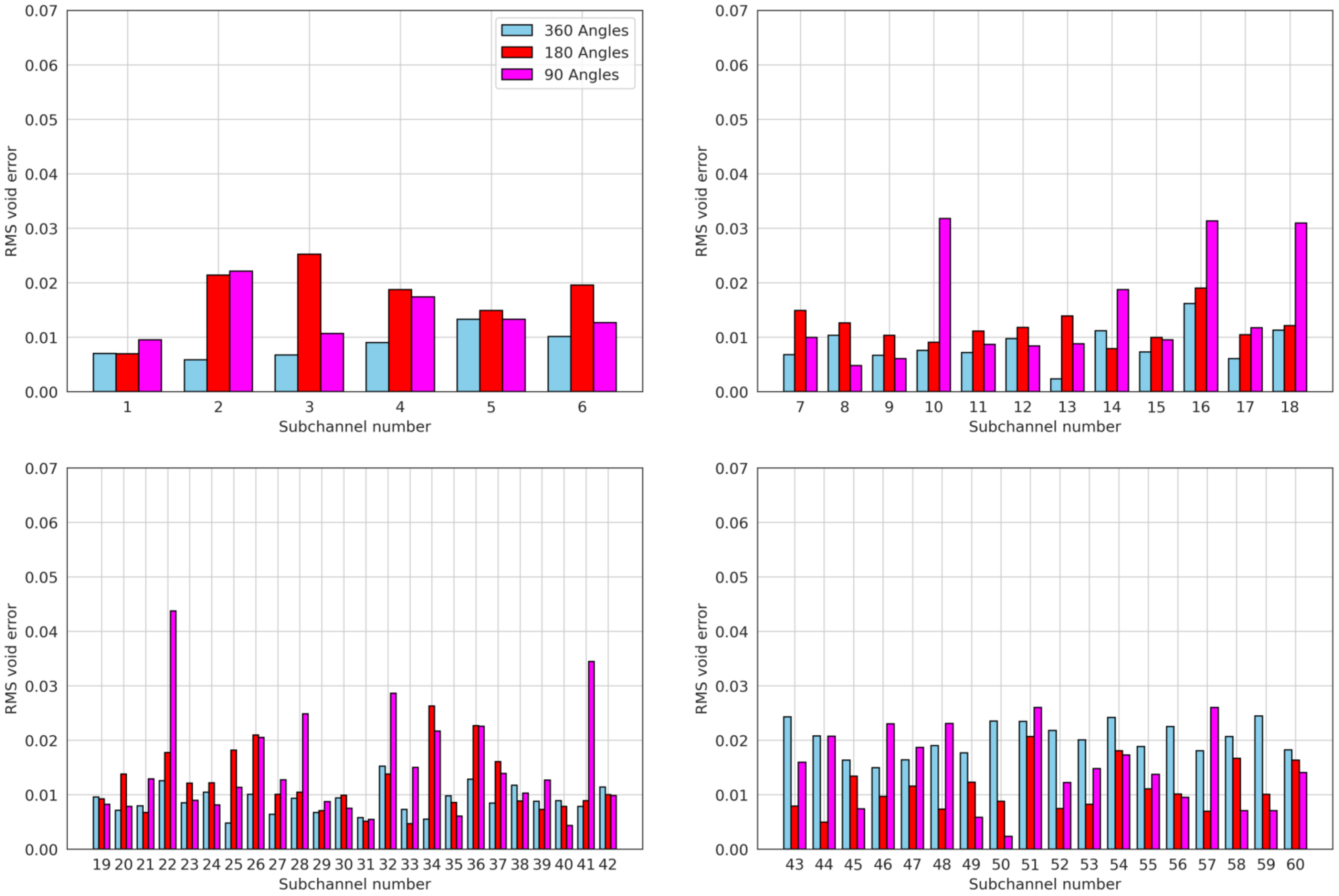

Figure 4.1.39: Void RMS errors for each subchannel (with reference to Figure 4.1.41) for the summation pixel case (8 x 3 x 3 = 72 mm^2 detector area).

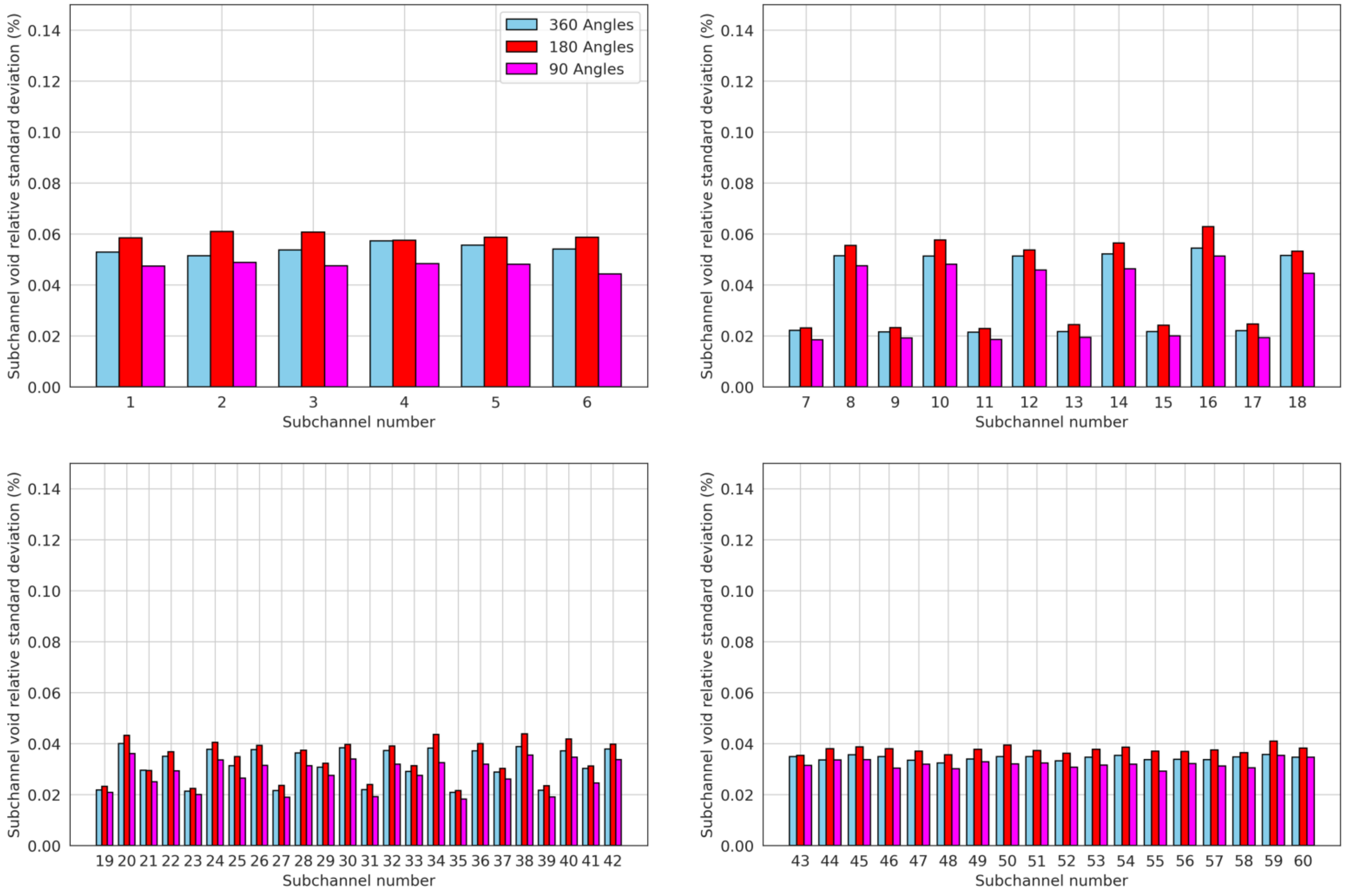

Figure 4.1.40: Void relative standard deviation for each subchannel (with reference to Figure 4.1.41) prediction for the summation pixel case (8 x 3 x 3 = 72 mm^2 detector area). The standard deviation represents the spread in the prediction of void fraction and is similar for each of the number of scanning angles.

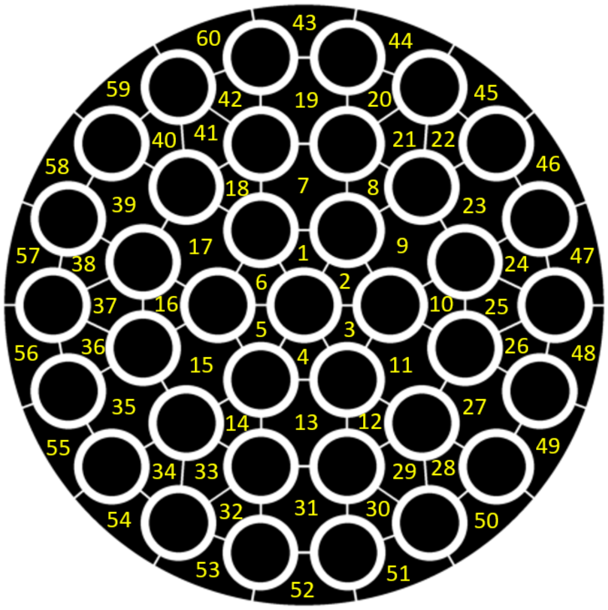

Figure 4.1.41: subchannel map for the 37-element CANDU geometry.

A reduction in scan times can be realized by selecting 90 angles and reducing the time per projection to 5 s (scan of 7.5 minutes). However, the reduction to 5 s per projection necessitates the 8-pixel summation method to obtain acceptable agreement with the actual void values. A comparison between the 5 s and 20 s 8-pixel scan predictions for 90 angular intervals is shown in Figure 4.1.44 and indicates that a minimum theoretical scan time of 7.5 minutes can be achieved with minimal reduction in prediction fidelity. An example of the overall subchannel predictions for these single and summation cases are shown in Figure 4.1.47. The comparison of the RMS and relative standard deviation is shown in Figure 4.1.42 and Figure 4.1.43 respectively. It is apparent that the single pixel case has larger relative standard deviation and therefore larger error bars, which is due to the higher statistical error compared to the 8-pixel summation (20 second scan time for the single detector pixel case versus 5 seconds * 8 pixels = 40 second equivalent scan time for the 8-detector pixel summation case). However, the RMS errors are similar and therefore the prediction quality is not diminished. Therefore the faster scan time comes at the expense of increased random error due to stochastic noise.

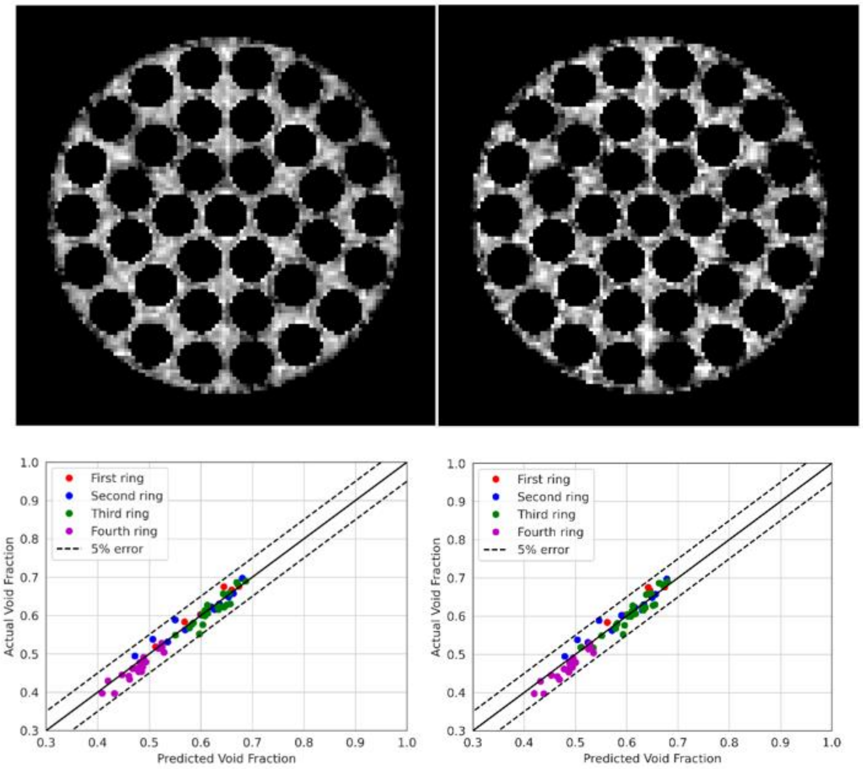

	20 s	5 s
RMS error	0.017	0.019
Average error	0.004	0.004

Figure 4.1.44: 90-angular projection case: 5 s per projection prediction (right column) and 20 s per projection prediction (left column). A single random object sample is shown to display general trends on a ring basis more clearly.

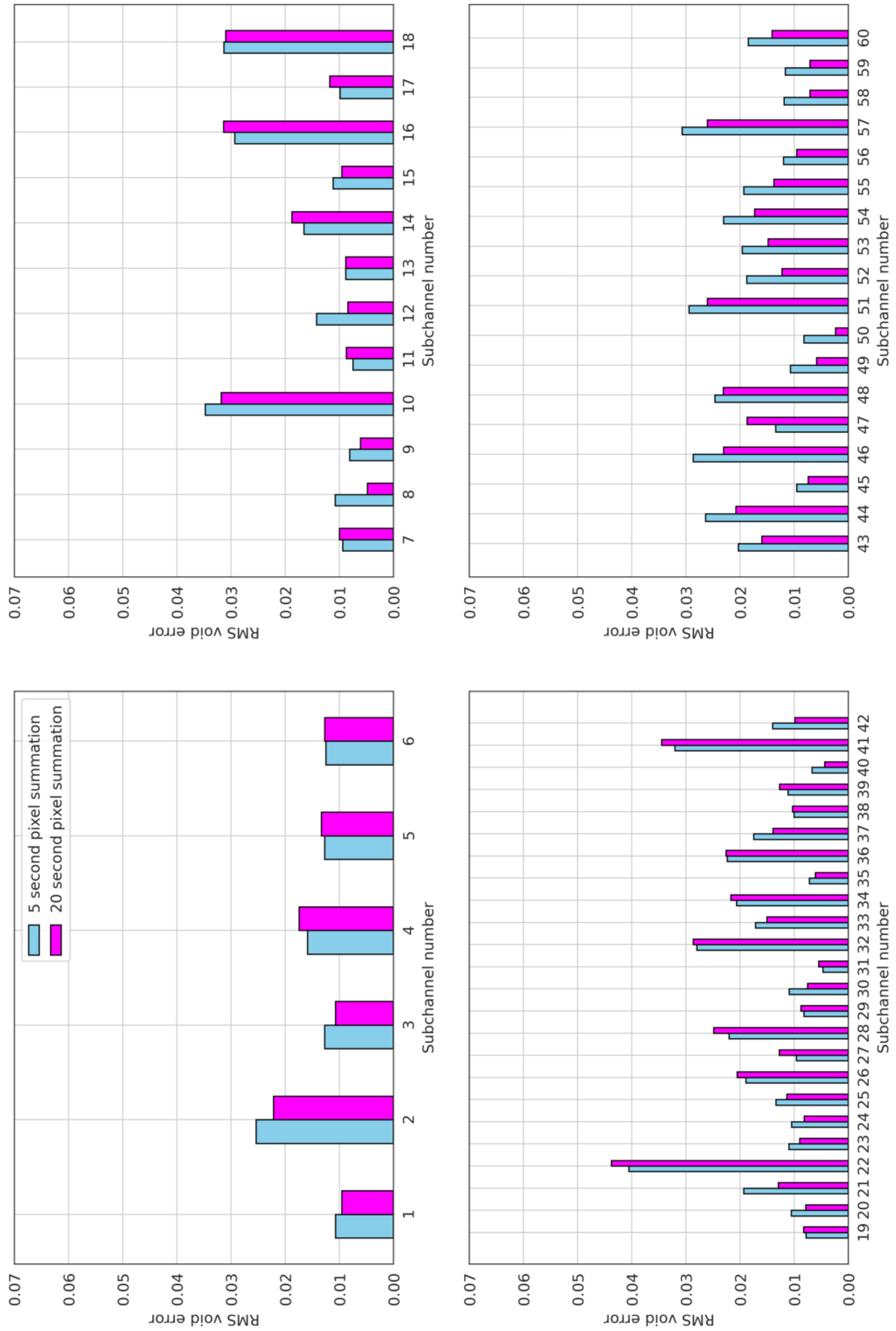

Figure 4.1.45: Void RMS errors for each subchannel (with reference to Figure 4.1.41) for the 7.5 minute scan time and the 30 minute scan time.

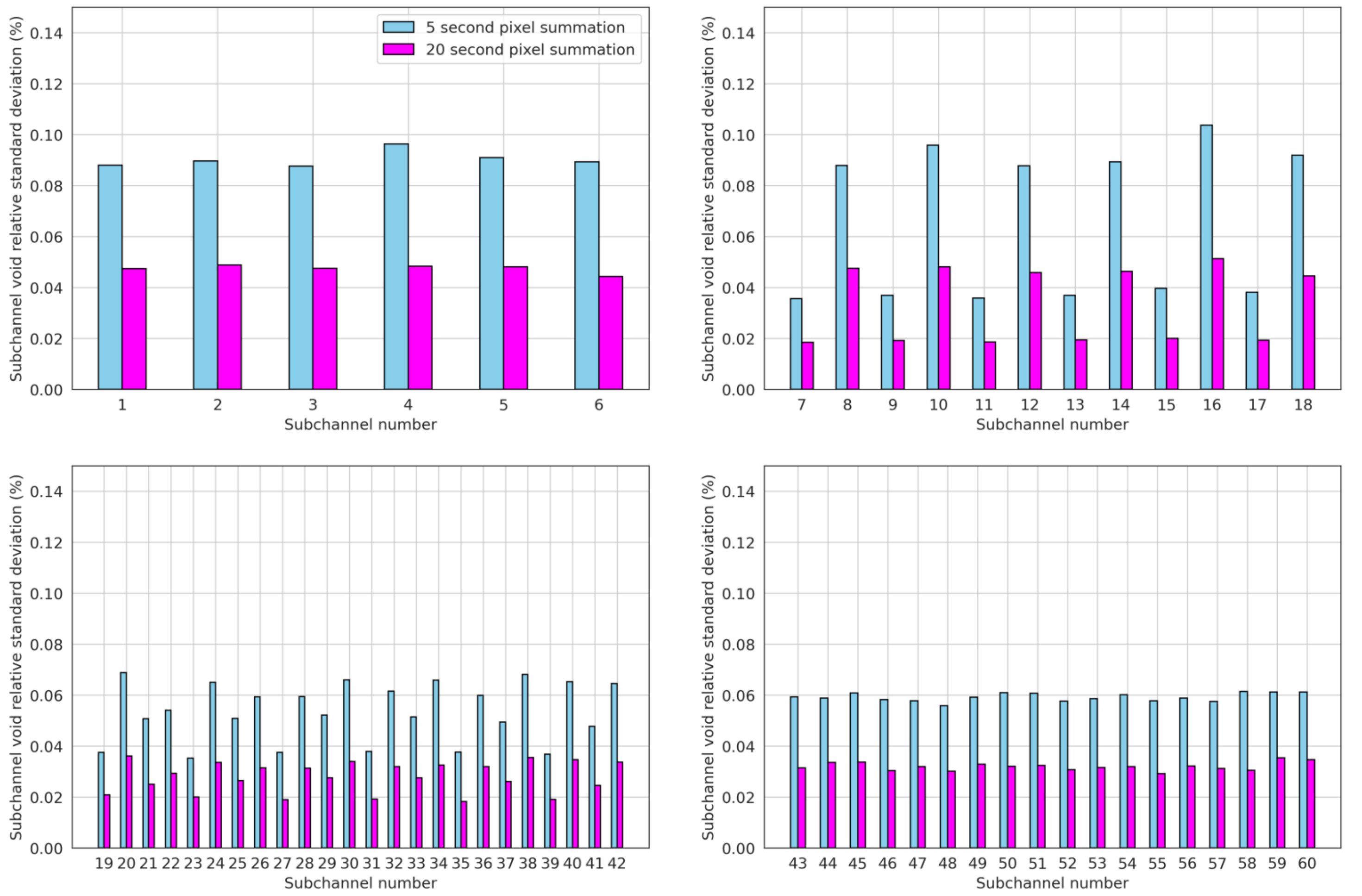

Figure 4.1.46: Void relative standard deviation for each subchannel (with reference to Figure 4.1.41) prediction for the summation pixel case (8 x 3 x 3 = 72 mm^2 detector area) for 90 angles with 5 s projections time (7.5 minutes total) and 20 second projection time (30 minutes total).

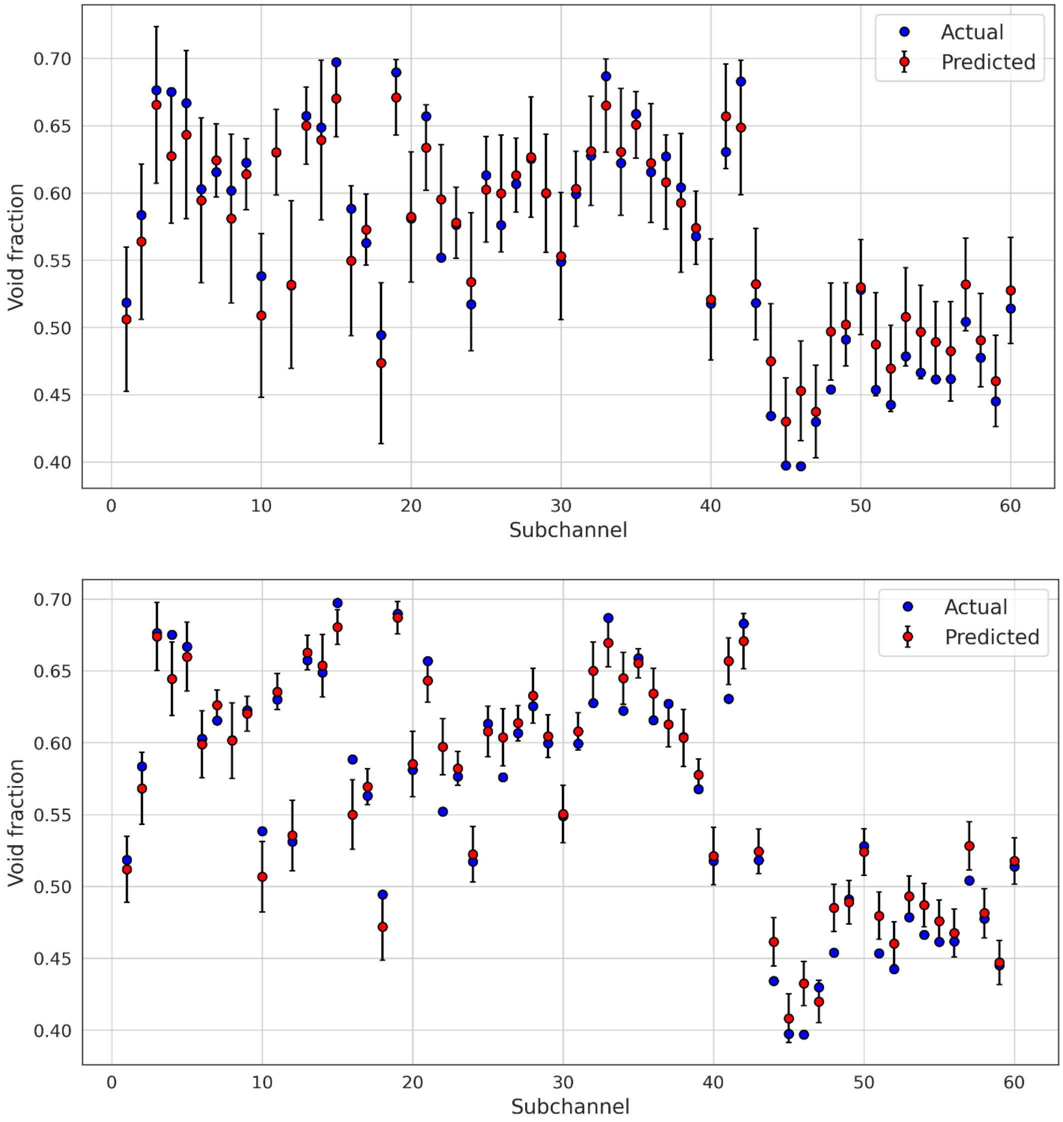

Figure 4.1.47: subchannel averaged void prediction for each subchannel for single (3 x 3 = 9 mm^2 detector area) (top) and 8-pixel (8 x 3 x 3 = 72 mm^2 detector area) summation (bottom) cases.

Another alternative method to shorten the projection time has been used with XCT systems by Morooka et al [37] and more recently by Arai et al [33] to take several sinograms at the same projection angle at shorter scan times, and calculating the average sinogram. In principle this method is used to shorten the scanning window to the millisecond range to reduce the magnitude of time-averaging artifacts in the measurement. However, in the case of the current fast neutron system, the scan times on the order of milliseconds increase statistical errors drastically compared to an X-ray method. Therefore, to make use of such a measurement technique in the future, a stronger source, or more efficient detectors would be necessary.

Angular views at facility

Another constraint to consider involves the final application of the system at Stern Laboratories. At Stern Laboratories, the test facility uses an I-beam below the test section for instrumentation support and makes complete 360° rotation impossible. This results in an angular scanning range of 16 – 344 degrees giving 83 angular projections (using the 90 projection 4° intervals over the full 360° as the base case). The effect of limited angles on the reconstruction are shown in

Figure 4.1.50, Figure 4.1.48 (RMS errors), and Figure 4.1.49 (relative standard deviations). The data shows minimal difference between the limited angle and full angle cases and the void prediction is not significantly impacted.

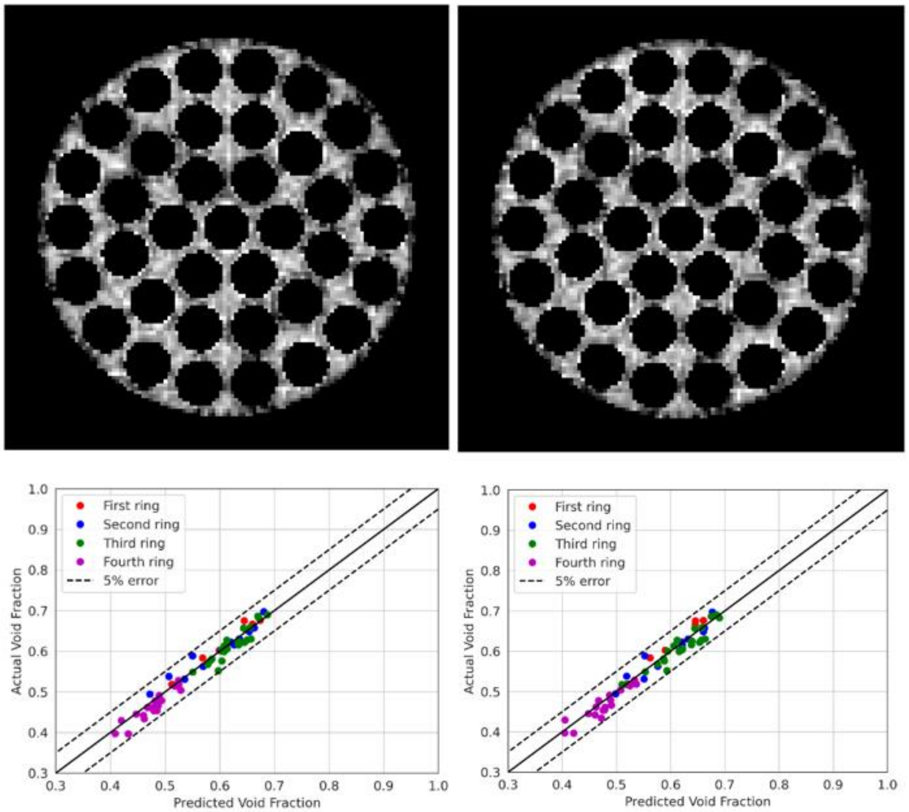

	90 angles	83 angles
RMS error	0.017	0.017
Average error	0.004	0.004

Figure 4.1.50: limited angle prediction (right column) and full 360 angle prediction (left column).

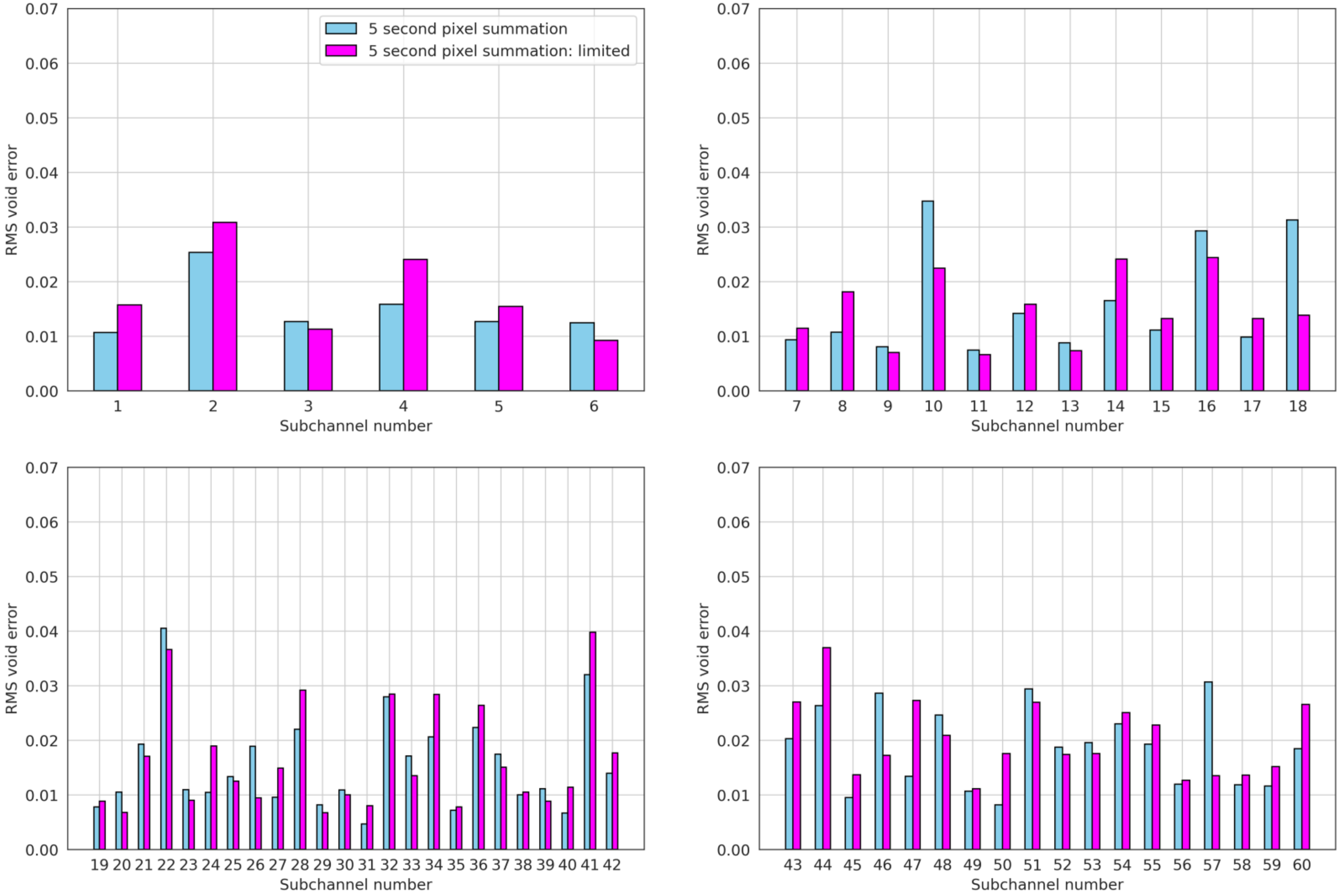

Figure 4.1.51: Void RMS errors for each subchannel (with reference to Figure 4.1.41) 90 angle and limited 83 angle cases with 5 seconds per projection.

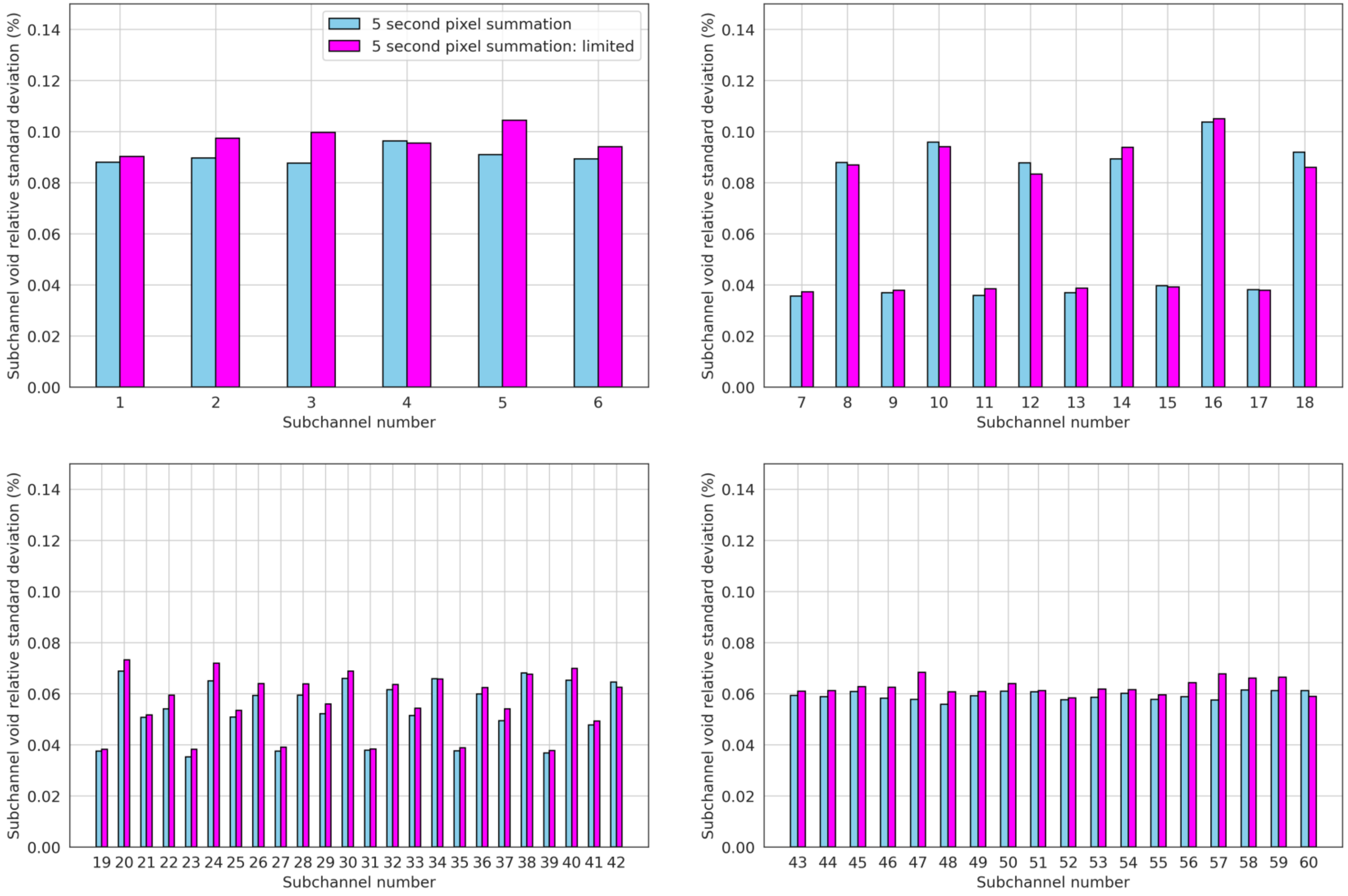

Figure 4.1.52: Void relative standard deviation for each subchannel prediction for the summation pixel case (8 x 3 x 3 = 72 mm^2 detector area) for 90 angles and 83 angles with 5 seconds per projection.

Dynamic bias discussion

Simulation studies of the dynamic bias error have involved tube studies primarily, and there have been no studies of the effect for bundle void fraction. A few representative simulations are included here to gauge the broad effect of the dynamic bias under some representative cases, as there has been no direct way to correct bundle-type data in the open literature, other than to scan in very short time intervals (which is not possible in this case due to low output statistics when sampling on the order of transient phenomena). The case studies here use a square wave change in void with equal periods of fluctuation conditions meaning that two image frames are cycled for equal periods when generating the projection data. A square pulse function is identified as the maximum error inducing function, given the abrupt changes in void fraction [113], which is also confirmed in the simple void fluctuation case from 0 to 100% void given by Andersson [112]. Each of the test cases were imaged assuming negligible counting error to explore the systematic effect on void prediction; counting error will increase the spread of the data, while maintaining the same underlying systematic trend. The test cases are:

1. 0 to 100% void in every subchannel (Figure 4.1.53): this is the "worst-case" scenario, providing the highest void fluctuation and therefore represents a maximum variance in void fraction.

2. Stationary subchannel core void with changing liquid film thickness on every pin (Figure 4.1.54): this shows the effect of changing liquid films on the void predication. Each pin has equal liquid film thickness, and changes from 100 – 750 μm between frames. A constant core void of 0.5 is applied in every subchannel.

3. Stationary liquid films, changing core void fraction (Figure 4.1.55): this shows the effect of the changing vapour core void fraction on void prediction. Each pin has the same liquid film thickness of 400 μm and a void core that changes between 0.5 and 0.8.

4. Randomly selected film thicknesses and randomly selected core void fractions (Figure 4.1.56): this shows the combination effect of changing liquid films and core void fractions together. Each pin has its own liquid film randomly selected between 100 and 750 μm. The core void fraction is allowed to vary on a pixel-by-pixel basis between 0.5 and 1.0. The films and core void fractions are then updated randomly for the next sampled frame.

Overall, the effect seems to be quite minimal for variations of liquid films and core void fractions. The primary exception is test case 1, which ultimately provides a worst-case scenario of fluctuations. Even in this case the voids were overpredicted by at most about 9% void (Figure 4.1.53). Although case 1 is not realistic, it indicates that the effect will act to systematically overpredict void under high fluctuations, and it represents a theoretical maximum void error that may be incurred. Such effects are more relevant for flow regimes such as slug flow and are not expected in flow regimes such as annular flow which are of concern in this thesis. For the other cases it seems that the small perturbation effect described by Harms and Laratta [5] may have some relevance. They showed that the void error due to a small fluctuating void component around a central average is approximately proportional to the squared amplitude of such void fluctuations. Therefore, if such fluctuations are small, the void error will also be small. It is therefore expected that in the experimental region of interest, where liquid films and variations are small, that the dynamic bias error will also be small.

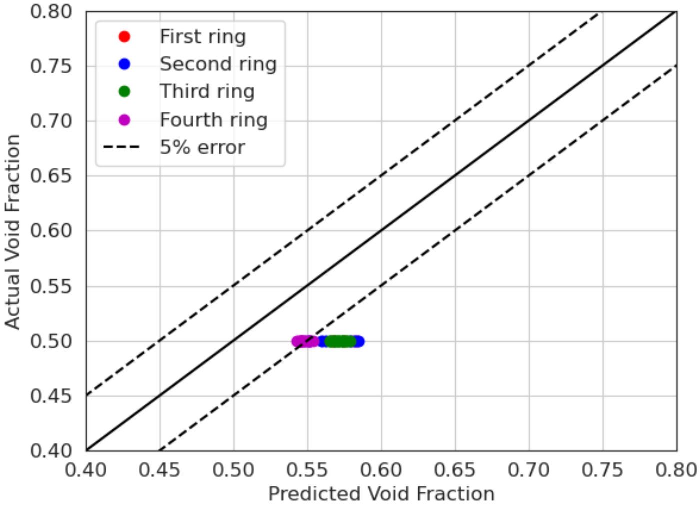

RMS error	0.072
Average error	0.071

Figure 4.1.53: Case 1: on/off liquid phase

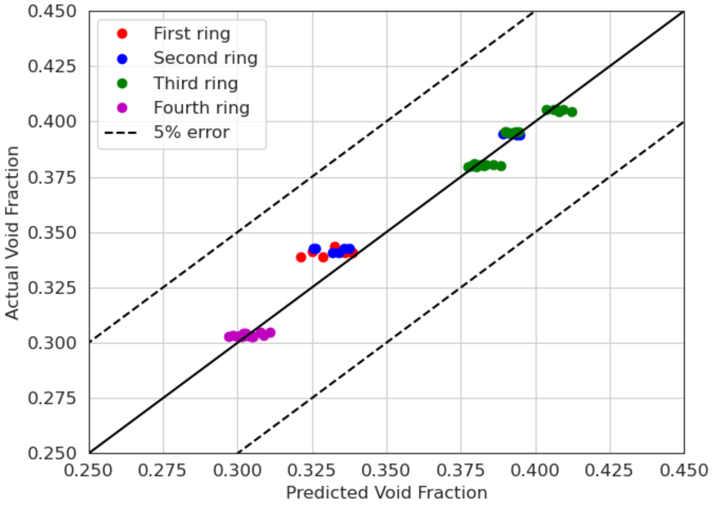

RMS error	0.006
Average error	-0.002

Figure 4.1.54: Case 2: Stationary void core, film fluctuate between 100 and 750 µm

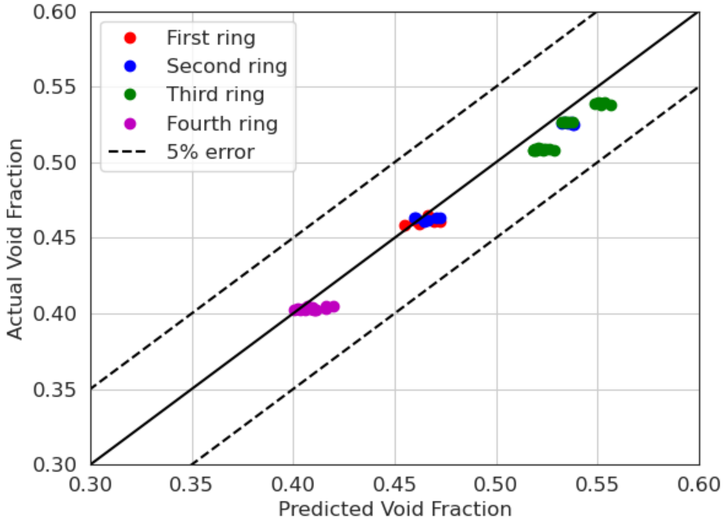

RMS error	0.010
Average error	0.008

Figure 4.1.55: Case 3: Stationary film of 400 μm, void core varies from 0.5 – 0.8

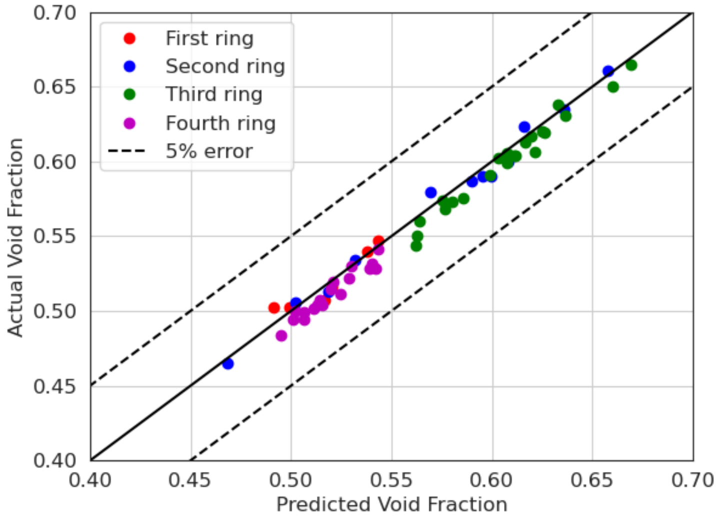

RMS error	0.008
Average error	0.005

Figure 4.1.56: Case 4: Random films between 100 and 750 μm, random void core pixels from 0.5 to 1.0.

4.1.4 Summary

In this section the noise properties of the imaging system such as the effect of background and crosstalk count fractions were quantified. The ambient background fractions were determined for three testing facilities. Representative object background scatter noise was also determined. These background fractions can be used to correct the experimental measurements. A crosstalk kernel was developed and applied to simulated data and the effect of crosstalk on resolution was quantified.

The void fraction measurement potential was also quantified using a representative CANDU 37-element bundle example with the scan times limited to 30 minutes. A systematic underprediction of void fraction was noticed at low per-projection scan times. This was due to thresholding void fraction values to physical between 0 and 1. Since the stochastic noise in limited scan time cases is high, this leads to an underprediction when thresholding. An in-situ measurement technique using a single projection view to eliminate this underprediction bias was developed. The method acquires a single projection 10 times and calculates the maximum normalized standard deviation (σ/μ) for the sample. It was found that a normalized standard deviation of 0.04 provides a cut off for underestimation bias elimination and corresponds to a per projection scan time of 20 s. A theoretical minimum scan time to acceptably measure the subchannel averaged void fraction was identified at 7.5 minutes using this criterion.

A potential dynamic bias error was explored and found that the error is minimal for the cases tested. However, if the void fraction in flow regimes with higher levels of fluctuation are to be measured, such as slug flows, a more in-depth systematic analysis is required to fully characterize the dynamic bias error for bundle geometries. With the system resolution quantified and the void fraction prediction capabilities explored, the next section discusses the experimental measurements taken with the FNCTS on test phantom geometries.

5 The Fast Neutron Computed Tomography System

> *Engineers like to solve problems. If there are no problems handily available, they will create their own problems.*
> Scott Adams

5.1 System components

This section provides an outline of the equipment involved in the design of the FNCT system and the relevant operating principles. Focus will be given to the details of the equipment that are used in the benchmarking tests, and the gantry design will be briefly outlined. Standard operating procedures (SOPs) for the system are in **section 9.3**. The high-level system design consists of 3 major components:

1. the neutron generator
2. the scintillator/detector array and processing electronics
3. rotational gantry system/rotational mechanism

The rotational gantry is described first, followed by the system components used in the experimental testing and validation of the fast neutron imaging system.

5.1.1 Gantry

The gantry system is the mechanical system used to traverse, hold, and position the source and detector about the test section. The final gantry has the following specifications:

- Rotates to a desired angle with an accuracy of ± 0.5°
- Rotates at a minimum speed of 1°/s.
- Holds a set angle for a duration of over 1 minute.
- Fits around existing test facility
- Supports the weight of the neutron generator and detector unit
- Mounts to I-beam at Stern Laboratories test facility

The gantry is composed of a double-ring assembly (DRA), a suspension assembly (SA) and support brackets with motors and encoders. The DRA (Figure 5.1.1) is the main portion of the gantry and is designed to mount the source and detector units. A complete DRA assembly is composed of four half-rings (Figure 5.1.2) 304 stainless steel sections (914 mm ID) and eight cross-members (Figure 5.1.2); the half-ring sections are used to assemble the gantry around an existing test section, and the cross-members provide mounting positions for detectors and the neutron generator in addition to providing support for the two ring sections. The SA mounts to the overhanging I-beam in the Stern Laboratories facility (Figure 5.1.1). The SA members allow the attachment of the gantry. Rotation of the gantry is accomplished via custom-made ring support brackets with stepper motor control which can position the gantry to within 0.5° with an angular travel speed of 1°/s (Figure 5.1.3). The full gantry assembly is shown in Figure 5.1.4. The gantry is not used for the experimental data collection for this thesis but is slated to be used in future testing and the final system application at Stern Laboratories.

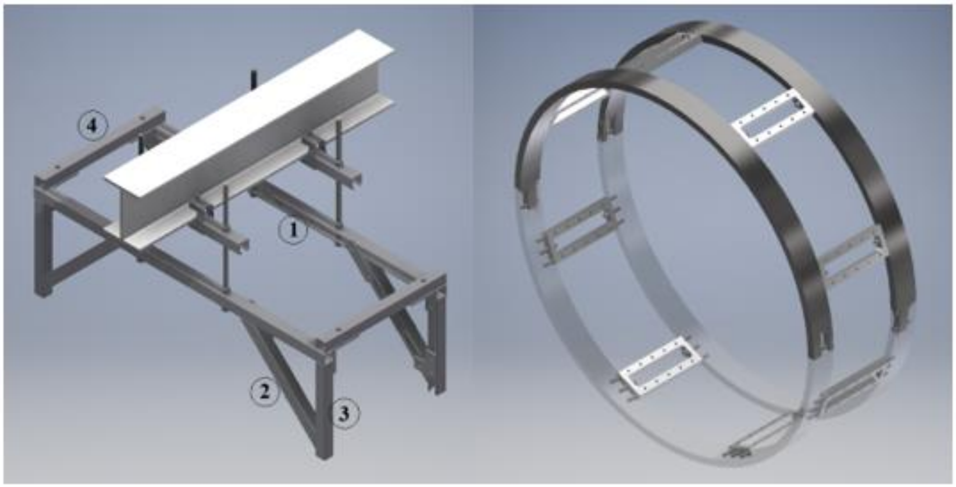

Figure 5.1.1: suspension assembly (left) and half-ring and cross-member assembly (right).

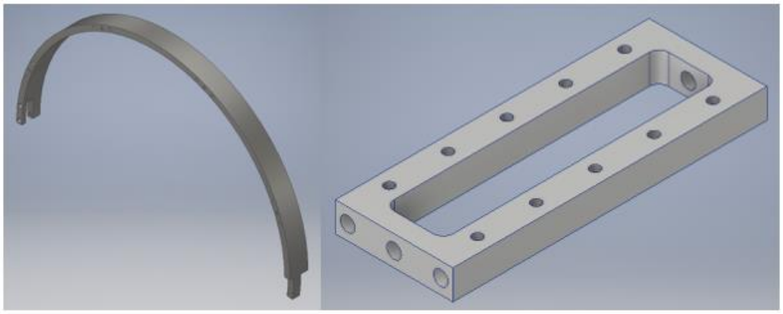

Figure 5.1.2: half-ring (left) and cross-member (right).

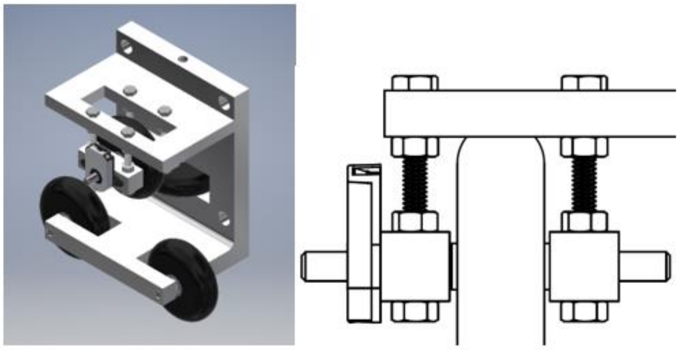

Figure 5.1.3: gantry ring support and rotation mechanism.

Figure 5.1.4: full gantry assembly (left) and CAD rendition of assembly (right).

5.1.2 Neutron generator

The fast neutrons are generated using the Starfire nGen™ 400 D-D very intense point source (VIPS) neutron generator. This neutron generator provides:

- a high neutron output (2.6×10^8 n/s maximum, on-axis at 180 keV accelerator voltage)
- a small emission spot size of 2 mm
- a lightweight frame of 11 kg.

making the generator compact and transportable. Additionally, the generator runs off of a standard single-phase 120 VAC wall plug, drawing about 5 A of current. The frame also has mounting brackets such that it can be mounted to the rotational gantry. A dedicated cooling system is used to remove heat from both the target and generator head. A picture of the generator and the dimensions are shown in Figure 5.1.5 and the output characteristics are listed in Table 3.

The operation and control of the neutron generator is self-contained in a control system GUI provided by Starfire (Figure 5.1.6) which provides simple on/off capability with a single button press. Parameters such as the accelerator operating voltage and system pressure may be adjusted to alter the output rates of the neutron generator with the accelerator voltage providing stable operation between 160 kV – 180 kV.

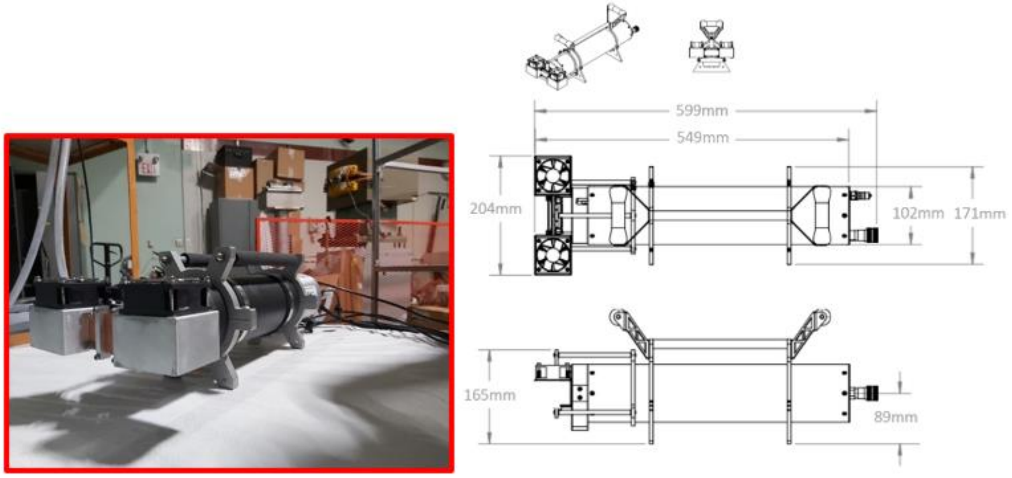

Figure 5.1.5: neutron generator (left) and dimensions (right [132]**)**

Table 3: neutron generator output characteristics

Voltage (kV)	Current (mA)	Neutron output measured on-axis (n/s)	Anisotropy corrected neutron output (n/s)[4]
160	0.42	1.9x10^{8}	1.1x10^{8}
170	0.44	2.2x10^{8}	1.2x10^{8}
180	0.46	2.6x10^{8}	1.4x10^{8}

---

[4] The on-axis (0°) measurement is used to determine the total flux. This flux is a factor of 2 higher than the average isotropic output and therefore requires correction to determine and report the total neutron production rate of the generator.

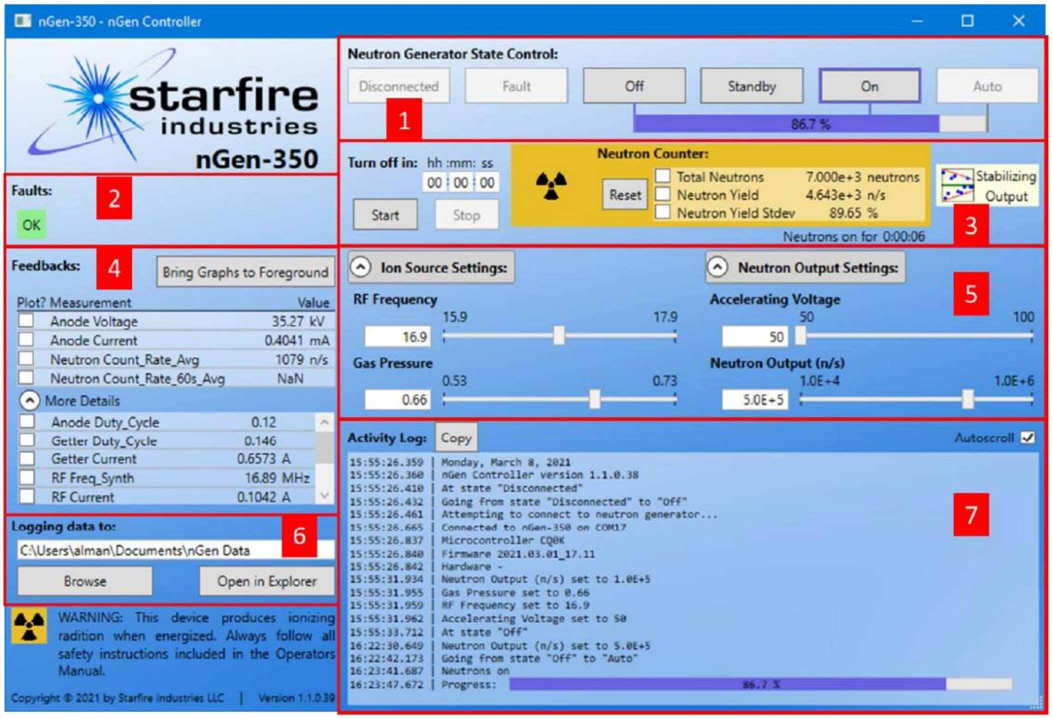

Turn off in: hh :mm: ss 00 : 00 : 00

Neutron Counter:

☐	Total Neutrons	7.000e+3 neutrons
☐	Neutron Yield	4.643e+3 n/s
☐	Neutron Yield Stdev	89.65 %

Neutrons on for 0:00:06

Plot?	Measurement	Value
☐	Anode Voltage	35.27 kV
☐	Anode Current	0.4041 mA
☐	Neutron Count_Rate_Avg	1079 n/s
☐	Neutron Count_Rate_60s_Avg	NaN
☐	Anode Duty_Cycle	0.12
☐	Getter Duty_Cycle	0.146
☐	Getter Current	0.6573 A
☐	RF Freq_Synth	16.89 MHz
☐	RF Current	0.1042 A

RF Frequency: 16.9 (15.9 – 17.9)

Gas Pressure: 0.66 (0.53 – 0.73)

Accelerating Voltage: 50 (50 – 100)

Neutron Output (n/s): 5.0E+5 (1.0E+4 – 1.0E+6)

C:\Users\alman\Documents\nGen Data

WARNING: This device produces ionizing radition when energized. Always follow all safety instructions included in the Operators Manual.

Copyright © 2021 by Starfire Industries LLC | Version 1.1.0.39

```
15:55:26.359 | Monday, March 8, 2021
15:55:26.360 | nGen Controller version 1.1.0.38
15:55:26.410 | At state "Disconnected"
15:55:26.432 | Going from state "Disconnected" to "Off"
15:55:26.461 | Attempting to connect to neutron generator...
15:55:26.665 | Connected to nGen-350 on COM17
15:55:26.837 | Microcontroller CQ0K
15:55:26.840 | Firmware 2021.03.01_17.11
15:55:26.842 | Hardware -
15:55:31.934 | Neutron Output (n/s) set to 1.0E+5
15:55:31.955 | Gas Pressure set to 0.66
15:55:31.959 | RF Frequency set to 16.9
15:55:31.962 | Accelerating Voltage set to 50
15:55:33.712 | At state "Off"
16:22:30.649 | Neutron Output (n/s) set to 5.0E+5
16:22:42.173 | Going from state "Off" to "Auto"
16:23:41.687 | Neutrons on
16:23:47.672 | Progress:                86.7 %
```

Figure 5.1.6: neutron generator control interface.

5.1.3 Fast neutron detector

5.1.3.1 SiPM

The SiPM sensors used in this system are the Hamamatsu S13361-3050AE-08, which is an 8 x 8 matrix of SiPM channels with a 3 x 3 mm^2 pixel size providing a total array size of 25.8 x 25.8 mm^2 (including structural grid). Each pixel consists of 3584 micropixels (50 x 50 µm^2 each) all connected in parallel. The array requires a low bias voltage of 53 – 58 V depending on the required gain and noise minimization. The final designed detector system consists of 14 8x8 arrays, providing 112 detector pixels in the radial direction with 8 pixels in the axial direction. A benefit of the detector array configuration is that axial pixels can be binned to increase count rates if necessary. This binning configuration was examined in the previous chapter and is used throughout the experimental testing to ensure acceptable counting statistics.

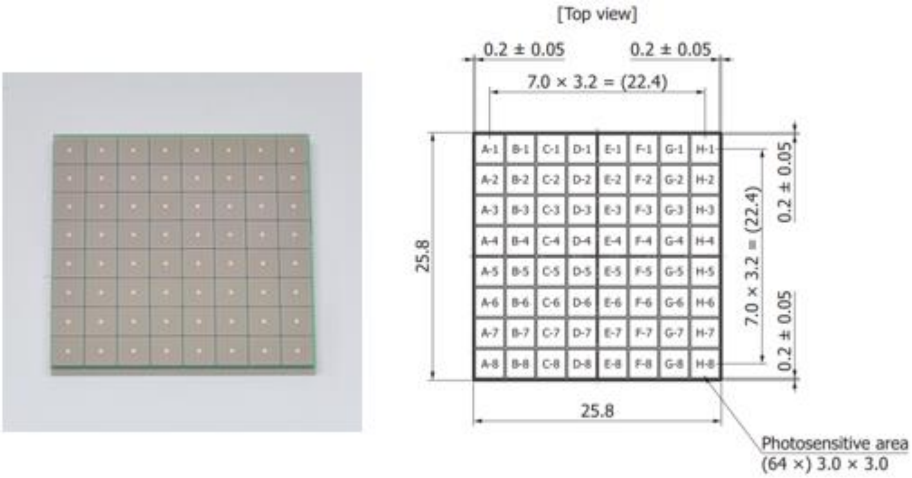

Figure 5.1.7: Hamamatsu S13361-3050AE-08 SiPM array (dimensions in mm). Reprinted from [133]**.**

5.1.3.2 Scintillator

The scintillator is a hydrogen-rich Saint Gobain BC400 pixelated plastic scintillator [134] matching the dimensions of the SiPM array. Bulk crystals were considered due to the ease of manufacture, and thus lower cost, than the pixelated scintillators but were found to provide more diffuse light collection than the size-matched pixelated detectors. The analysis is presented in section 9.2.1.

Each of the pixelated sections is separated by a light reflective coating to optically isolate the scintillator pixels and maximize light collection within a given pixel region (Figure 5.1.17). Additionally, the BC400 scintillator has good spectral matching to the Hamamatsu SiPM (423 nm wavelength peak) and fast emission decay times. As explained earlier the scintillator thickness of 5 cm was chosen since it corresponds to the mean free path of 2.5 – 2.8 MeV neutrons and provides good detection efficiency while limiting background counts.

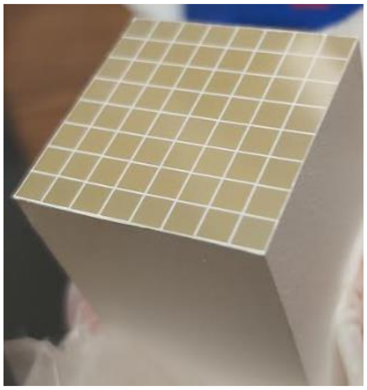

Figure 5.1.8: Saint Gobain pixelated BC400 plastic scintillator

5.1.4 Processing electronics

Pulse processing electronics were initially designed in-house for the system and the schematics are included in the **section 9.2** for completeness. The final design replaced the initial circuit with a scalable ASIC design from CAEN that uses the PETIROC ASIC technology combined with FPGA readout control in an all-in-one platform of the DT5550W. The DT5550W system provides a fully programmable readout system for rapid digital processing of 128-pixel channels per board with a prototyping GUI (Figure 5.1.9) to rapidly test, prototype, and optimize important operational settings in pulse counting (i.e., trigger levels, shaping constants, detector bias voltages, etc.).

```
0000000000000000000000000
[ACQ  (NI120012) 03/10/2018 18:38:43]   Starting acquisition
[CORE (NI120012) 03/10/2018 18:38:43]   Live Process is enabled: EVENTS and CLUSTERS
decoded
[ACQ  () 03/10/2018 18:38:46]   Reset live data
```

Run ID: 0
Run: FREE RUNNING
File Size: 0.00 MB
Run Time: 00:00:09.284
Disk: 84,098.07 MB
Events: 28143
Clusters: 15633
Download: 2.0054/1.0025

Figure 5.1.9: DT5550W prototyping GUI.

A single DT5550W board (Figure 5.1.10) is comprised of:

- 1 field programmable gate array (FPGA)
- 1 CAEN DT5550W processing board
- Output graphical user interface (GUI) for prototyping
- A55PET with 4 ASIC mounting slots
- SAMTEC ERCD-040-240.0-TTL-TTL-1-D extension cables (2 m long) to extend the detectors off of the processing board.

Figure 5.1.10: DT5550W processing board with A55PET mounted. ASIC (red) and FPGA (yellow) highlighted.

The A55PET piggyback board provides the SiPM signal pulse processing via 4 PETIROC ASIC chips. Specifically, 2 ASICs can process 64 individual channels (a full 8 x 8 SiPM array). Each processing channel uses a fast preamplifier for accurate time-triggering, a pulse shaper and sample and hold circuit for accurate energy readout, and an internal ADC. The A55PET piggyback board specifications are:

- 2 sockets for 8x8 silicon photomultiplier (SiPM) array per board (coupled to scintillators)
- 4 PETIROC application specific integrated circuit (ASIC) chips
- Integrated low-noise power supply (CAEN A7585D)

Each PETIROC ASIC has its own set of 32 charge and time triggers, which combine to provide a full-digital readout of the system. The charge readout line uses a fast pulse shaping amplifier with tunable capacitance value to choose the shaping time and pulse magnitude (Figure 5.1.11). The shaping parameters can be changed according to the information in Table 4. A sample-and-hold method is used to measure the charge (voltage) using a high bandwidth preamplifier (DC-coupled) coupled with a fast discriminator that will trigger a "hold" signal with a tunable delay to sample the voltage peak (see **section 9.2.2**). The readout of each DT5550W/A55PET processing board is sent to a processing computer via USB 3.0. For more information on the PETIROC ASIC, see [135].

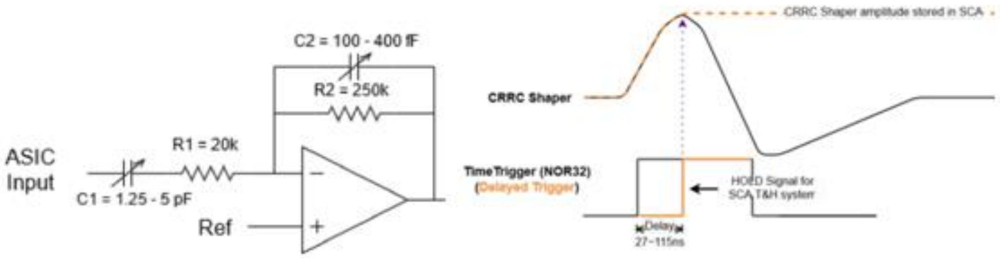

Figure 5.1.11: pulse processing electronics for the A55PET.

Table 4: PETIROC pulse shaping parameters.

C1 (pF)	**R1 (kΩ)**	**τ1 (ns)**	**C2 (fF)**	**R2 (kΩ)**	**τ2 (ns)**
1.25	20	25	100	250	25
2.5	20	50	200	250	50
3.75	20	75	300	250	75
5	20	100	400	250	100

The imaging system is comprised of 6 to 7 of these boards and necessitates parallel acquisition. Each board requires 3 LEMO cables to propagate the acquisition and trigger signals for each readout board simultaneously (Figure 5.1.12) as well as a

USB3.0 port available on the processing computer for each board used in the acquisition.

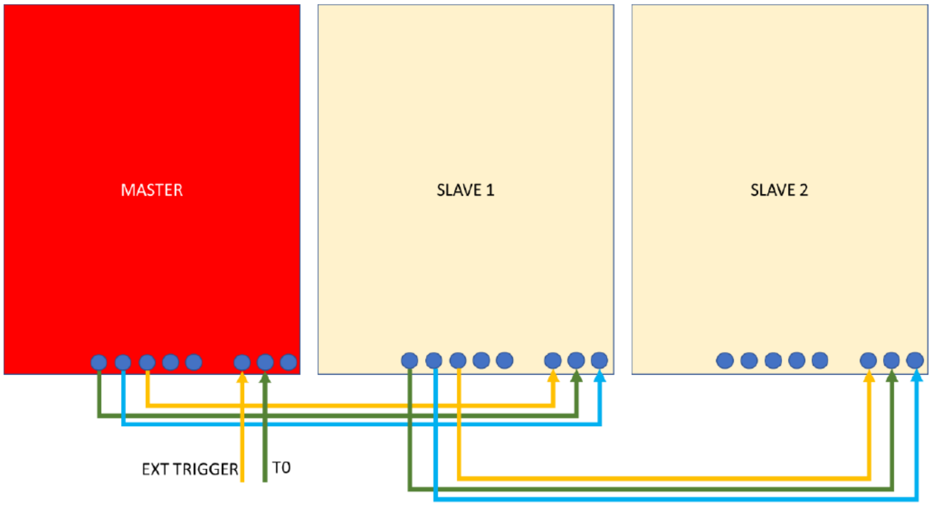

Figure 5.1.12: multi-board connection where the yellow, cyan, and green wires propagate the timing information and run signal trigger to multiple boards [136]**.**

CAEN has developed a multi-board readout system to accomplish this with a much simpler display than the traditional GUI (Figure 5.1.13).

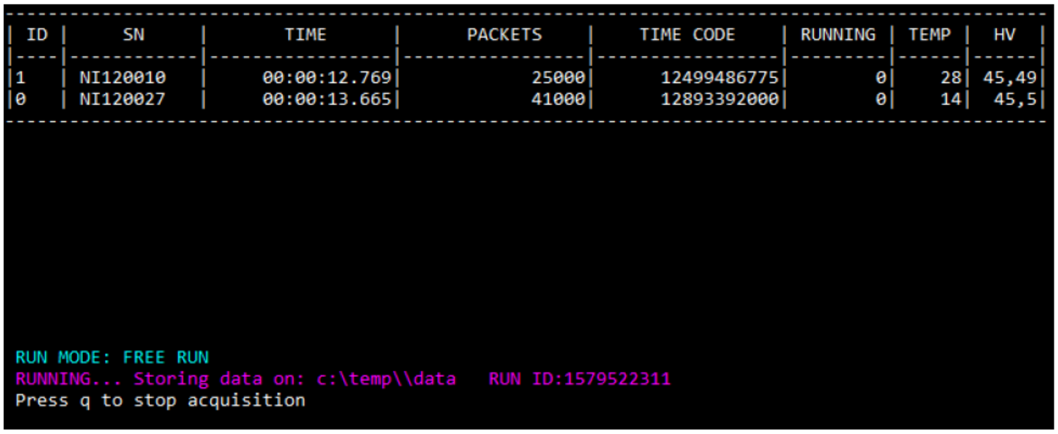

```
--------------------------------------------------------------------------------------------------
| ID |     SN      |      TIME       |     PACKETS     |   TIME CODE     | RUNNING | TEMP |  HV  |
|----|-------------|-----------------|-----------------|-----------------|---------|------|------|
|1   | NI120010    |     00:00:12.769|            25000|      12499486775|        0|    28| 45,49|
|0   | NI120027    |     00:00:13.665|            41000|      12893392000|        0|    14|  45,5|
--------------------------------------------------------------------------------------------------




 RUN MODE: FREE RUN
 RUNNING... Storing data on: c:\temp\\data   RUN ID:1579522311
 Press q to stop acquisition
```

Figure 5.1.13: multi-board readout GUI for the DT5550W [136]**.**

Therefore, the output from multiple boards is not processed in the GUI and must be processed offline. This data is massive as it provides detailed energy information from 800+ pixels that needs to be processed. All of the data processing is accomplished using a custom-made Python processing script that performs the following functions:

- obtain the energy spectrum of every pixel
- apply pedestal energy correction to each pixel
- apply the energy threshold to each spectrum and calculate the count rates
- generate the attenuation profiles for each acquisition

Each SiPM pixel requires a unique calibration to relate the channel number to the energy of the incoming radiation. The energy calibration is necessary to provide an accurate and consistent energy thresholding for every pixel. Energy calibration for each pixel is accomplished using gamma- and X-ray sources, such as Na-22, Cs-137, Ba-133, and Cd-109, and measuring the Compton edge response output of the detector system. An example energy calibration for an individual pixel using Cs-137 and Na-22 is shown in Figure 5.1.14.

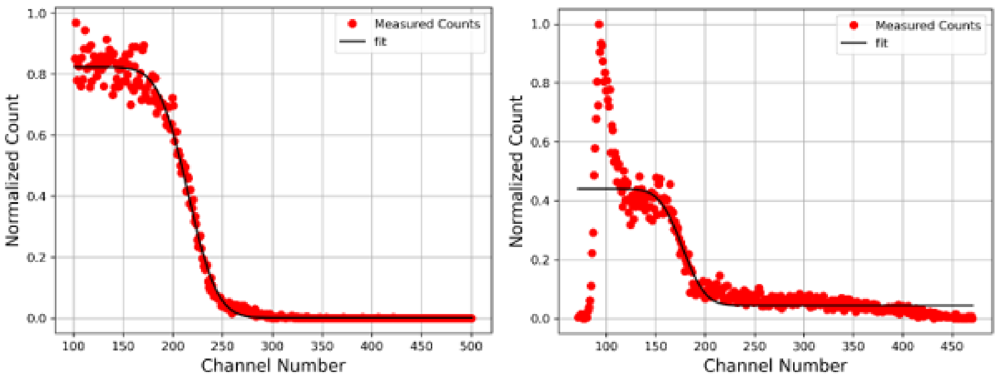

Figure 5.1.14: energy calibration using Cs-137 (left) and Na-22 (right)

5.1.4.1 Detector array assembly

The array and scintillator are coupled using optical coupling paste (EJ550) to form the final detector. Custom 3D printed PLA plastic detector holders (Figure 5.1.15) are designed to conform to the overall detector dimensions and align the detectors along the arc detector plate (Figure 5.1.16). There are two types of holders, down and up, to facilitate the cable management of the detectors[5]. The final design of the detector unit is shown in Figure 5.1.17.

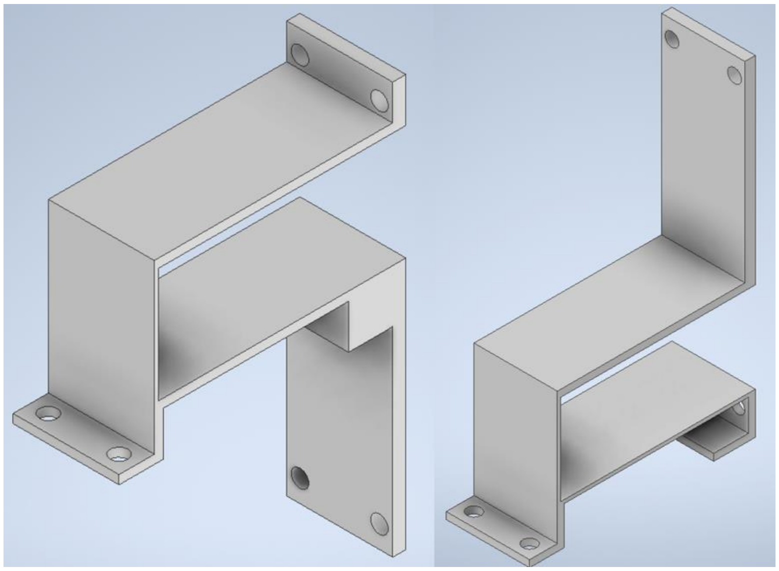

Figure 5.1.15: down position detector holder and up detector position holder.

---

[5] The SiPM output connection requires that each array be mounted at 180° from the neighbouring detector to allow for cable access when arrays are stacked as close as possible.

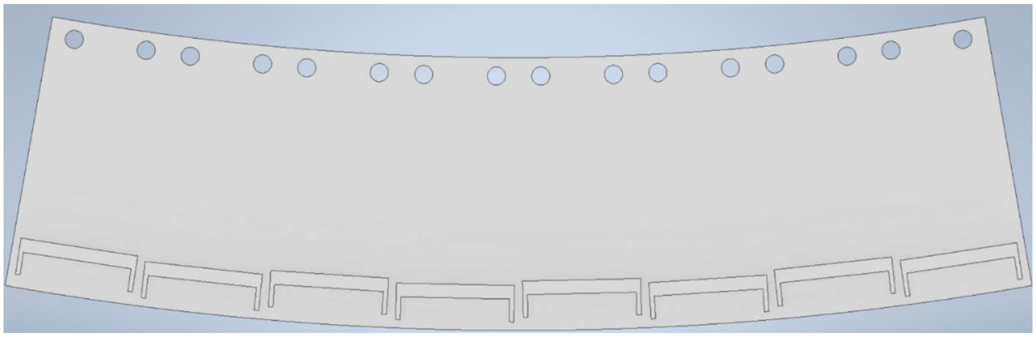

Figure 5.1.16: 60 cm detector arc alignment stage.

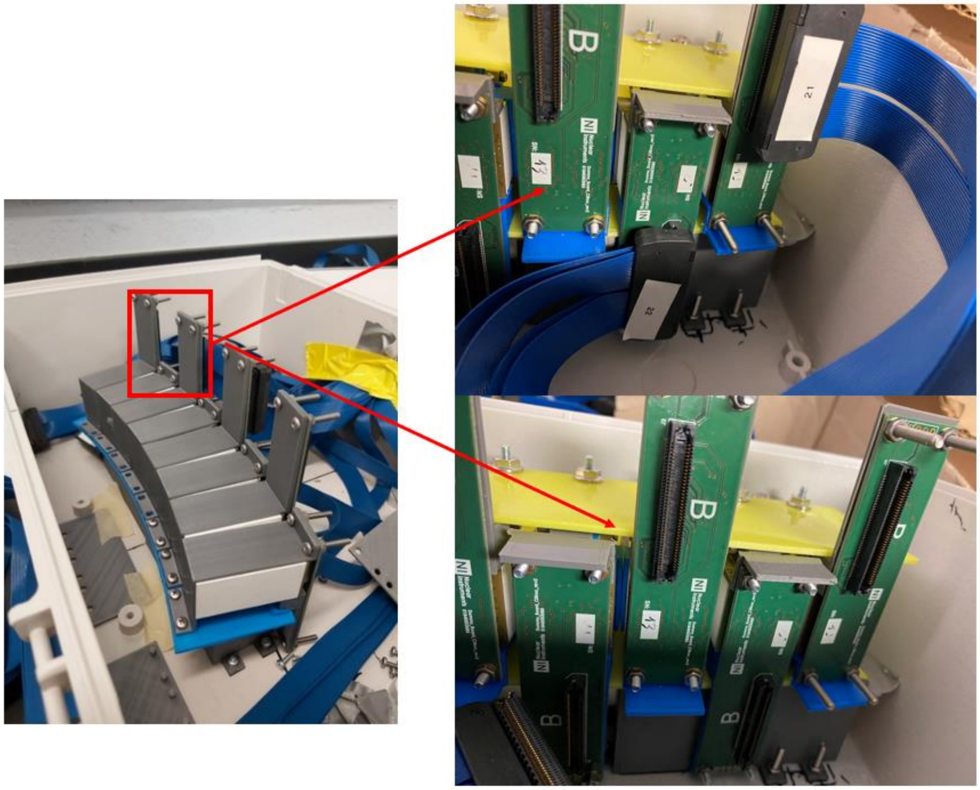

Figure 5.1.17: arc detector placed within the light-tight box enclosure showing the cables and mounts. Image shown on the left is of a 40 cm arc used in the Ontario Tech testing campaign.

5.1.5 Benchtop testing unit

The final benchtop unit consists of the detector unit housed within a light-tight enclosure, the neutron generator and a Thorlabs CR1-Z7K DC servo rotation stage (Figure 5.1.18). The rotation stage is used to rotate the object through a continuous $360°$ angle to with less than $0.02°$ repeatability error. For benchtop testing the object is rotated, as opposed to source-detector rotation, for simplicity. This represents the system configuration used in all experimental testing in this thesis. The final design parameters are summarized in Table 5, although some parameters were changed when testing in different environments and this is highlighted when necessary.

Table 5: summary of the final design parameters

Design specification	Value (mm)
Spot size	2
Detector pixel width	3
Scintillator depth	50
Source-object distance	200
Source-detector distance	600
Resolution	$\mathbf{\sim 1.85}^{*}$

*includes the crosstalk effect

Figure 5.1.18: benchtop testing unit mounted to an aluminum alignment beam with detector box (white, left) rotation stage (middle) and neutron generator (right).

6 Experimental Imaging

For a moment, nothing happened.
Then, after a second or so,
nothing continued to happen.
Douglas Adams

Before integrating the fast neutron imaging system components, a benchtop system was used to calibrate and finalize the imaging system parameters. Doing this provides a simple way to optimize system parameters in-situ, and rapidly image different test phantoms to quantify the imaging and void prediction accuracy. The benchtop system consists of the neutron generator, which is placed at a fixed distance from the rotation stage and the detector box unit, which houses the detector units. Each of the components are mounted to an optical alignment rail system to align each component by providing a reference point for each system component. To ensure the most optimal counting statistics, all pixels in a column were binned. The image acquisition process is documented in section 9.3.

The overall goal of the imaging campaign is to test some representative small-scale phantoms to determine functionality and capabilities of the system. The void fraction measurement capabilities are tested on representative test objects containing PLA plastic as a substitute for water and air as a substitute for vapour.

The attenuation coefficient of PLA is estimated using the density and weight fractions from [137] and compared with water in Table 6. The attenuation falls between the attenuation of water at room temperature and at 10 MPa saturated conditions. Notably the composition is much different, but the contrast in images should provide a representative case compared to water.

Table 6: comparison of water and PLA attenuation coefficients.

	Water (STP)	**PLA**	**Water (10 MPa saturated)**
Attenuation coefficient	$0.0196\ mm^{-1}$	$0.0164\ mm^{-1}$	$0.0135\ mm^{-1}$

6.1 Tomographic measurements

6.1.1 McMaster laboratory experiments

The first measurements were taken using the benchtop configuration (Figure 5.1.18) and initial testing was done using a custom-made stepper motor rotation stage while waiting for the Thorlabs CR1-Z7K DC servo rotation stage. The detector system was initially in a flat panel configuration for preliminary testing due to the ease in which different source-detector distances can be tested; testing in an arc configuration means that different distances would neccesitate a different arc curvature every time. Additionally, only 4 detectors (32 detectors along the cross section) are used for the initial testing to minimize radiation dose to all detectors while testing functionality, thus limiting the size of the objects that can be tested.

The per-projection scan times were set to 15 s and taken at 200 different projection angles at a magnification of 1.4. Notably, a larger source to detector distance is used to a) reduce the amount of fluence to the detectors and reduce the risk of damage to scintillators and SiPMs while testing and b) ensure that the test board electronics were far away from the source for the same reasons. Both of these considerations ensure that a large amount of testing does not cause damage and ruin later imaging tests when a higher magnification and a larger detector unit are used. The source to object distance is similarly increased to accommodate the smaller detector unit by lowering the magnification. Detectors external to the test object are used to normalize the results to account for any source fluctuations in a given projection. The scan parameters are summarized in Table 7.

Table 7: McMaster tomography test parameters.

Parameter	Value
Projection time	15 s
Number of projections	200
Angular increment	1.8°
Number of detectors	32
Magnification	1.4*
Image domain	32x32
Expected resolution	2.2 mm

*source-object (670 mm), source-detector (955 mm)

The test phantoms chosen for initial testing are a rectangular block to measure the resolution and contrast, and a 2x2 tube array to determine the ability to measure more complex structures. The CT images are reconstructed using the SART reconstruction method in AIRTools II [105]. The images for a rectangular block phantom and a 2x2 square subchannel geometry are shown in Figure 6.1.1 and Figure 6.1.3 respectively. These reconstructions required a shift in the sinogram as the center of rotation (COR) was shifted during the acquisition. The shift was implemented using a simple algorithm proposed by Yang et al. [138] and is accounted for in a modified system matrix calculation.

The resolution is quantified by measuring the ESF of the square block. The ESF is measured by taking multiple lines along each edge and averaging them together to produce an overall ESF. The measured resolution of ∼2.1 mm agrees well with the predicted resolution of 2.2 mm. A plot of the ESF fit is shown in Figure 6.1.2. The tube array is reconstructed well with all tube structures visibly identical.

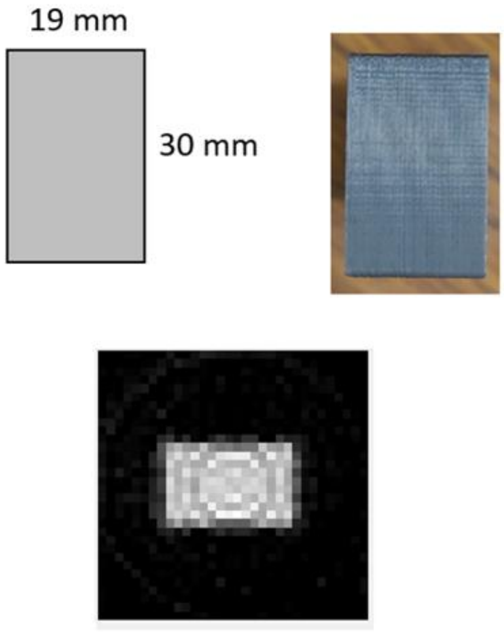

Figure 6.1.1: rectangular block phantom and reconstruction.

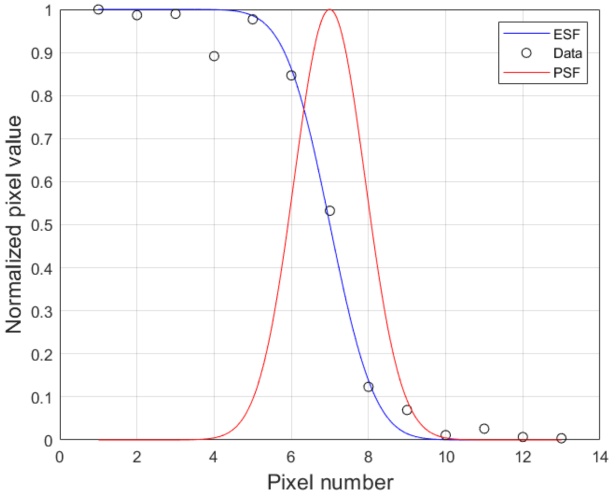

Figure 6.1.2: resolution quantification showing the fitted ESF function and PSF function.

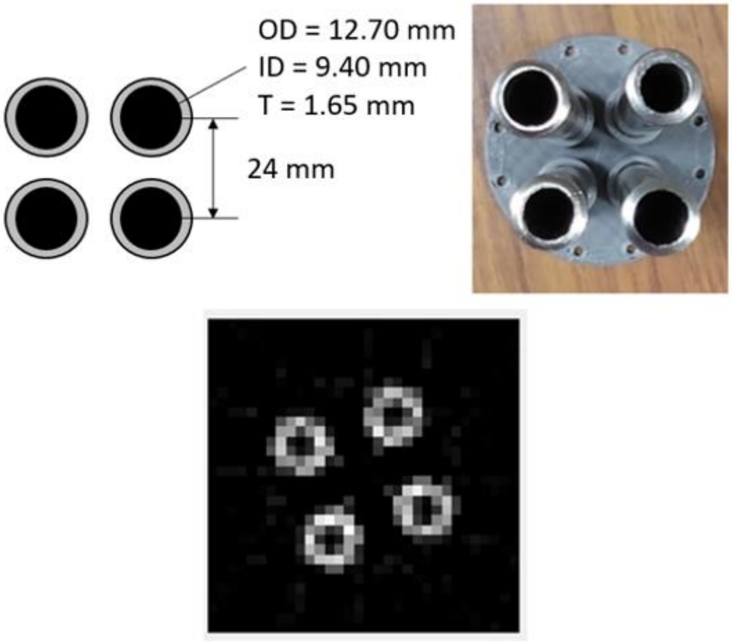

Figure 6.1.3: tube array phantom and reconstruction.

The images contain some ring artifacts and noise, but with an improved rotation stage and an aligned COR, less reliance on correction schemes and more consistent projection angles could reliably be obtained. Nonetheless, overall the objects are reconstructed reasonably well and the results demonstrate the functionality of the CT imaging system and the model prediction of resolution. The next stage is to measure more complex structures such as stationary liquid films and void cores within the small tube array.

Unfortunately, such images could not be taken with the design-basis neutron generator due to a catastrophic failure of the device. Fortunately, the neutron generator facility at Ontario Tech was available to take the void fraction images. However, the generator at this facility has an output several orders of magnitude less than the McMaster generator, and thus the scan times are much longer to provide the same statistics. The much larger scan times (on the order of 3 to 4 hours) also leads to issues of system stability (e.g., electronic drift) which is a potential source of noise not previously investigated. In addition, the spot size is also much greater than the McMaster generator (on the order of 5x greater) and therefore resolution will be much poorer. Therefore, the Ontario Tech imaging tests are used to show the ability of the system (i.e., detectors and readout system) to image feature differences, such as different thicknesses of plastic films and void fraction sensitivity with the understanding that with an increased neutron output and smaller spot size, the quantitative results would be greatly improved.

6.1.2 Ontario Tech laboratory experiments

The Ontario Tech neutron generator is a Thermo Scientific P385 D-D neutron generator model. The spot size is estimated to be about 10 mm, with an estimated output of $3\text{x}10^6$ n/s. As presented in [119], the neutron yield in the direction orthogonal to the beam is approximately 2/3 of the average output level. Therefore, the noise level of the images will be much higher than Adams et al. [72] and certainly lower than the McMaster neutron generator which is 2 orders of magnitude higher output than the system of Adams et al. [72]. Additionally, the image resolution will be worse, considering the spot size maximum estimate of 10 mm given by the company is 5 times larger than the McMaster generator spot of 2 mm. The parameters for the Ontario Tech tests are shown in Table 8.

Table 8: Ontario tech test parameters

Parameter	2x2 array
Projection time	60 s
Number of projections	100
Angular increment	3.6°
Number of detectors	64
Magnification	2.7*
Image domain	128x128
Expected resolution	6.4 mm

*source-object (150 mm), source-detector (400 mm)

Building on the measurements from the McMaster tests, a 2x2 square subchannel is imaged, this time with plastic films surrounding the outer surface of the pins to simulate a liquid film on a metallic surface. The goal is to obtain the subchannel void fraction of the image which requires full, empty, and 2-phase information, as per equation 3.1.16. For each of the image acquisitions, 100 equally spaced projections were taken over 360 degrees, with each projection taking 60 s of acquisition time. The number of angular projections was chosen to maximize the number of total projections available for the reconstruction algorithm, and hence increase the number of pixels that can be used in the reconstruction domain. The number of angles could not be increased further due to scan time constraints, and less angles would necessitate a reduced number of reconstruction domain pixels and therefore reduce the resolution of the reconstructed images. The scan time was set at a maximum of 60 s to make scan times feasible and provides a lower limit of statistical counting noise for the tests. The test parameters are outlined in Table 8 and the image reconstructions are shown in Figure 6.1.4.

Looking at Figure 6.1.4, the noise level of the images is admittedly poor (especially for the full plastic case where attenuation is highest), but the capability of the system to detect and measure structural differences is still apparent. For example, there is a clear difference between the bare rod case and the case with different films surrounding each pin. Additionally, in the film case the size of the films in the image are consistent with the expected relative sizing (Figure 6.1.5). From a qualitative perspective, the two 3 mm films are the same size, and the 2 mm and 1 mm films are noticeably different in size in the reconstruction. Therefore, although the statistics of the images are poor for the Ontario Tech case, the capability of the system to distinguish geometric features is demonstrated.

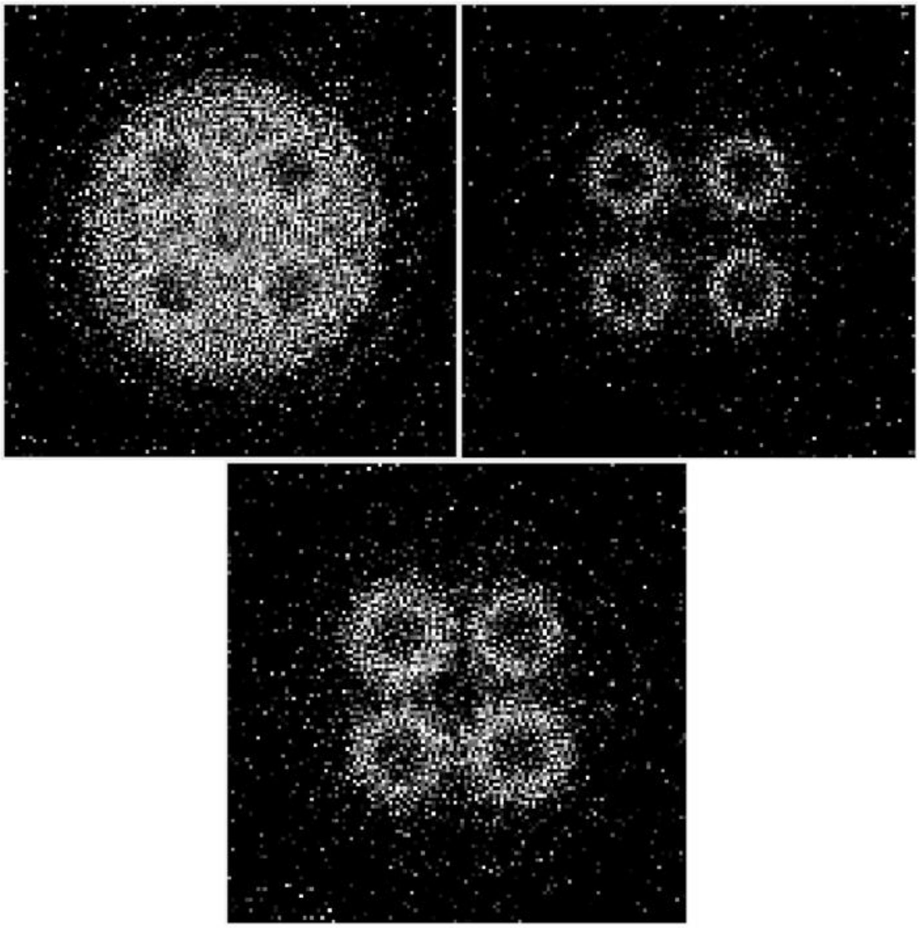

Figure 6.1.4: Image reconstruction of the full plastic (top left), bare array (top right) and the plastic film case (bottom).

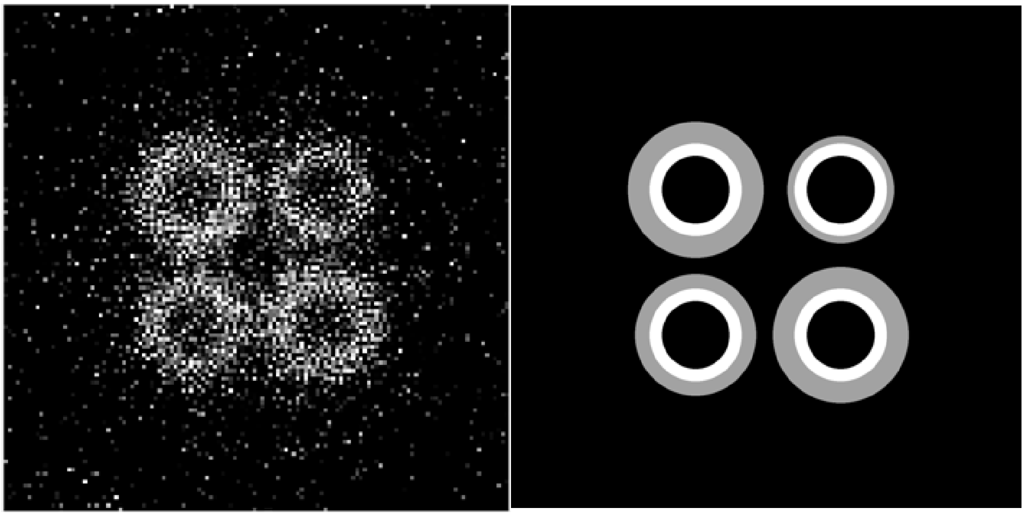

Figure 6.1.5: comparison of the reconstructed film case (left) and the actual film distribution (right). The film differences are apparent.

The image quality improvement due to improved source properties, such as smaller spot size (to improve resolution) and larger neutron output (to reduce the stochastic noise), can been demonstrated using a simulation of the McMaster neutron imaging system. Using the modelling techniques from chapter 4, a simulated result for the McMaster system is be generated and compared to the Ontario Tech system. The same parameters outlined in Table 8 to show the improvement in quality due to a smaller spot size and a larger neutron output obtained with the McMaster system. Figure 6.1.6 shows the expected improvement in image quality for the full, empty, and film cases and the significant improvement in the film case is further highlighted in Figure 6.1.7.

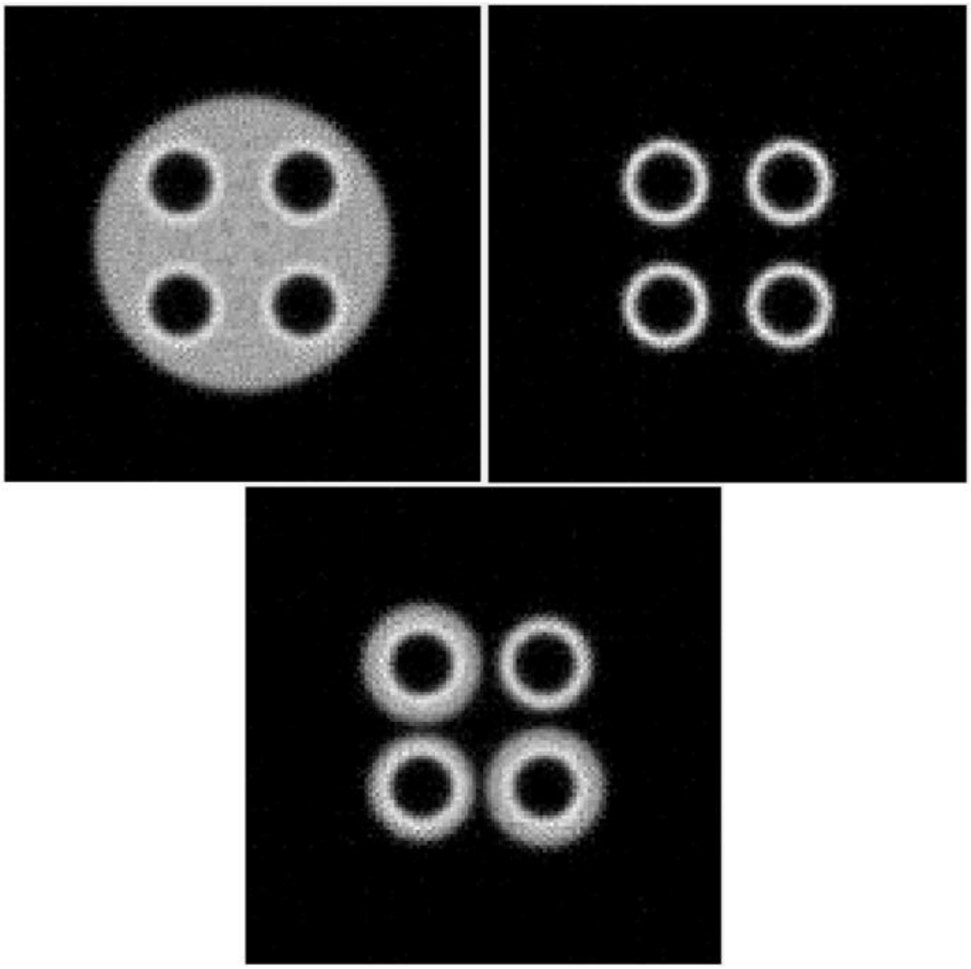

Figure 6.1.6: simulated image reconstruction of the full plastic (top left), bare array (top right) and the plastic film case (bottom) for the McMaster system.

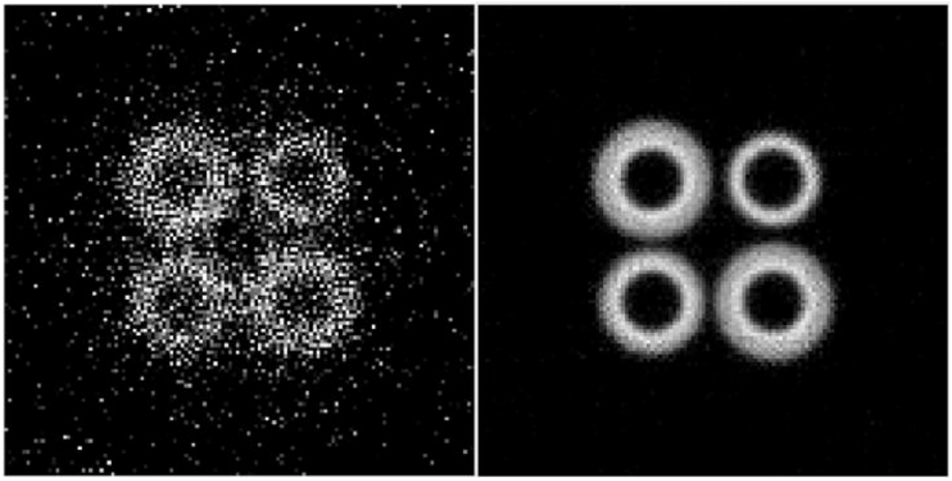

Figure 6.1.7: comparison of the Ontario Tech reconstructed film case (left) and the simulated McMaster reconstruction (right).

To obtain a measure of the void fraction for the Ontario Tech system, the void image was constrained so that the values could achieve a maximum of 1 and a minimum of 0 to maintain physically realizable values of void fraction (Figure 6.1.8). The void image is admittedly noisy, but the calculated average using the void threshold shows good agreement with the expected value (Table 9). However, the averaged void measurement is highly sensitive to thresholding, as shown in Table 9: void fraction comparison for the 2x2 tube array phantom for the Ontario Tech measurements. due to the noise creating negative values as well as large values above 1. As shown in Table 9, if the void fraction does not threshold values above 1.0, the void fraction measurement will produce a value of ∞ leading to an unreliable void fraction measurement. The void fraction image improvement using the McMaster system simulation are shown in Figure 6.1.9 and the estimated void fraction value and the effect of thresholding are shown in Table 10. The simulation demonstrates less threshold dependence and therefore a more reliable void fraction measurement is expected using the McMaster system.

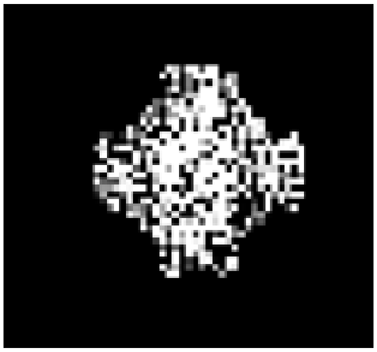

Figure 6.1.8: subchannel void fraction map using the images in Figure 6.1.4. Display range [0, 1]. The image displays non-realistic contrast since a value threshold is used.

Table 9: void fraction comparison for the 2x2 tube array phantom for the Ontario Tech measurements.

Actual	Measured*	Threshold > 1. 0	Threshold < 0
0.61	0.60	0.1787	∞

*Highly sensitive to the void fraction thresholding.

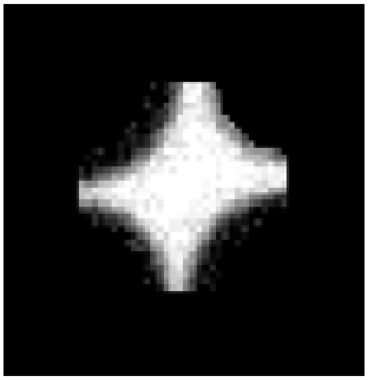

Figure 6.1.9: subchannel void fraction map for the McMaster simulation using the images in Figure 6.1.6Figure 6.1.4. Display range [0, 1].

Table 10: void fraction comparison for the 2x2 tube array phantom for the McMaster simulation.

Actual	Simulated	Threshold > 1. 0	Threshold < 0
0.61	0.60	0.59	0.60

Given the high level of noise in the Ontario Tech measurements, the unavailability of the McMaster neutron generator, and the infeasibility to obtain better image quality in a reasonable scanning time using the Ontario Tech source, a machine learning model is implemented to improve the quality of the reconstruction data. A convolutional neutral network (CNN) works well for this purpose since at a basic level the network is trained on data to 'learn' filtering operations to enhance image quality and/or identify features. For example, convolutional neural networks (CNNs) have been developed for low-projection CT imaging to improve image quality [139], and to denoise CT images in low dose imaging [140], [141].

A CNN implementation has the potential to improve imaging quality for the simple 2x2 rod array case examined here, and more importantly also can reduce scan times and enhance image quality for the final CANDU application once the McMaster neutron generator is repaired. The machine learning model used for this purpose is an open-source CNN architecture developed by Jin et al. [139] for limited angle CT reconstruction.

To train the model, high-quality training data must be produced. The data is generated using the principles outlined in section 4.1 by applying a range of spot size dimensions (3 – 10 mm) as well as different levels of background and statistical noise to capture some uncertainty in the generator neutron output rate and background scatter events and crosstalk. A total of 5000 sample data is generated and split into 4000 training and 1000 testing data for each phantom case (plastic-filled, empty, and film). The open-source hyperparameter optimizer package Optuna [142] is used to optimize the learning rate parameters. The model for each phantom (plastic-fill, empty, and 2-phase) is trained using TensorFlow with a batch size of 4 with the number of epochs set to 100 with the loss function optimizer set to mean squared error. A simplified flowchart is shown in Figure 6.1.10.

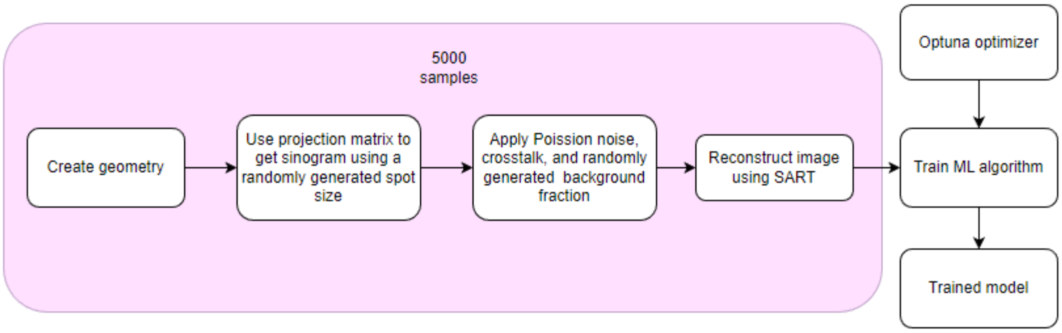

Figure 6.1.10: flowchart of machine learning model generation

The CNN is applied to the raw reconstructed image (Figure 6.1.12) and displays a remarkable improvement over the initial raw reconstructions. A comparison to the actual case and the raw image reconstruction highlights this further in Figure 6.1.13. The subchannel void fraction prediction for the test data is shown in Figure 6.1.11 and shows a slight systematic underprediction in the void fraction value, but within a 2% void error boundary. The systematic error could be reduced by having more defined set of parameters for spot size and neutron output rate used in the training set.

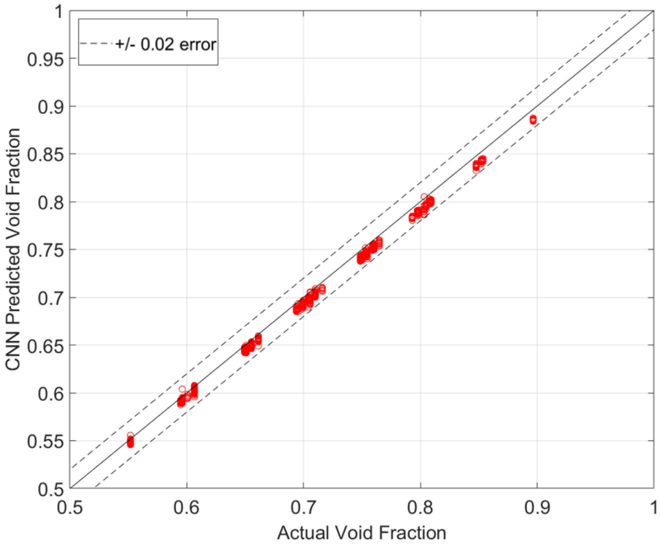

RMS error	0.007
Average error	-0.007

Figure 6.1.11:CNN void fraction prediction for the test data.

The subchannel void comparison for the Ontario Tech data is shown in Figure 6.1.14 and large improvement over the raw measurements. Notably, extreme values are no longer present, and the void distribution is significantly more uniform than the raw reconstruction. The predicted averaged void fraction value also compares well with the expected void fraction, as shown in Table 11, and is no longer as sensitive to thresholding.

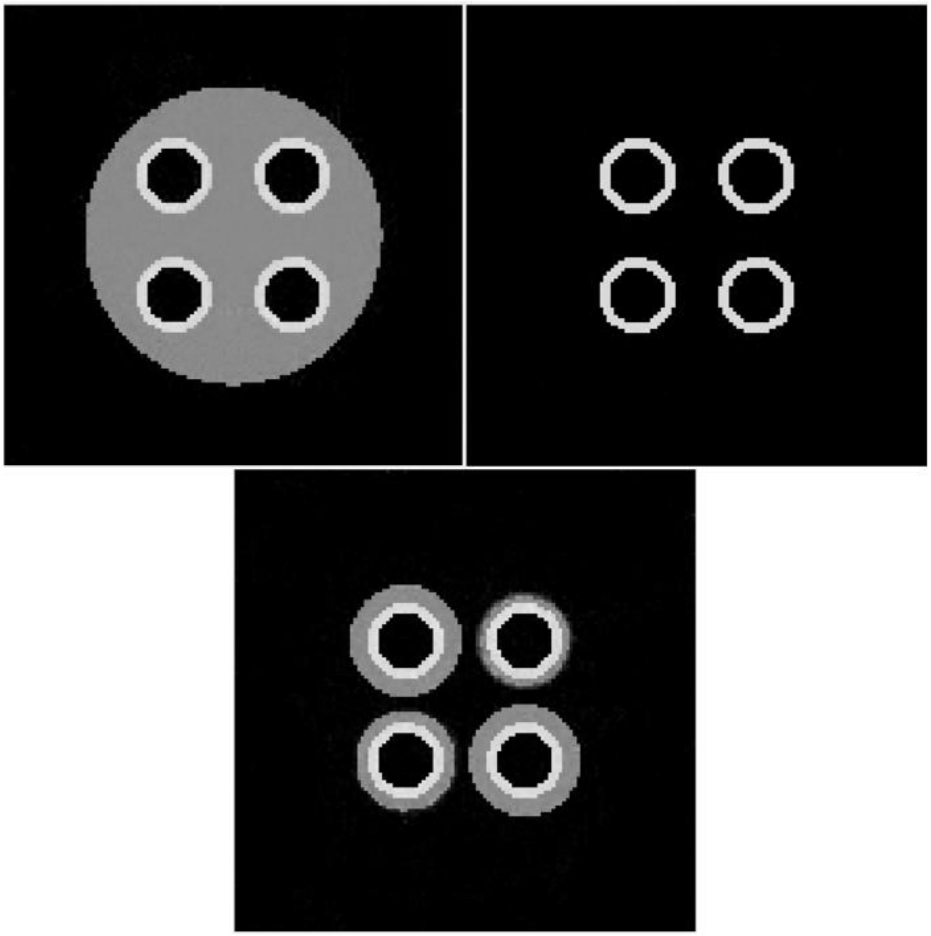

Figure 6.1.12: image reconstruction after the CNN processing: plastic fill (top left), bare array (top right) and plastic film case (bottom).

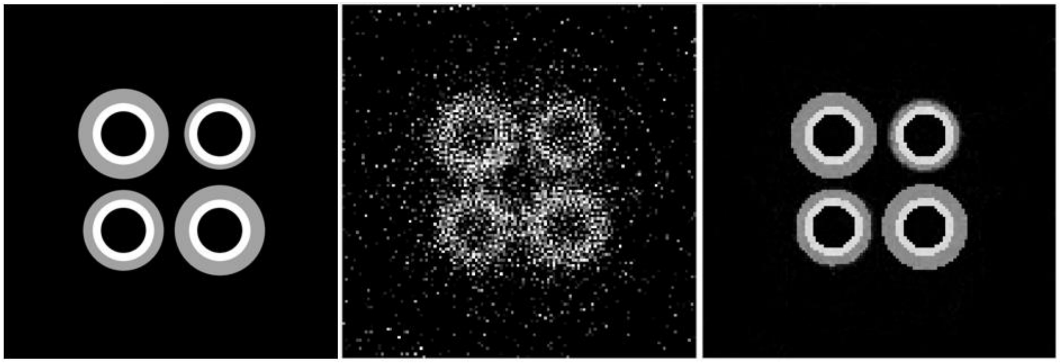

Figure 6.1.13: The actual film distribution (left), the raw reconstruction (middle), and the CNN output (right).

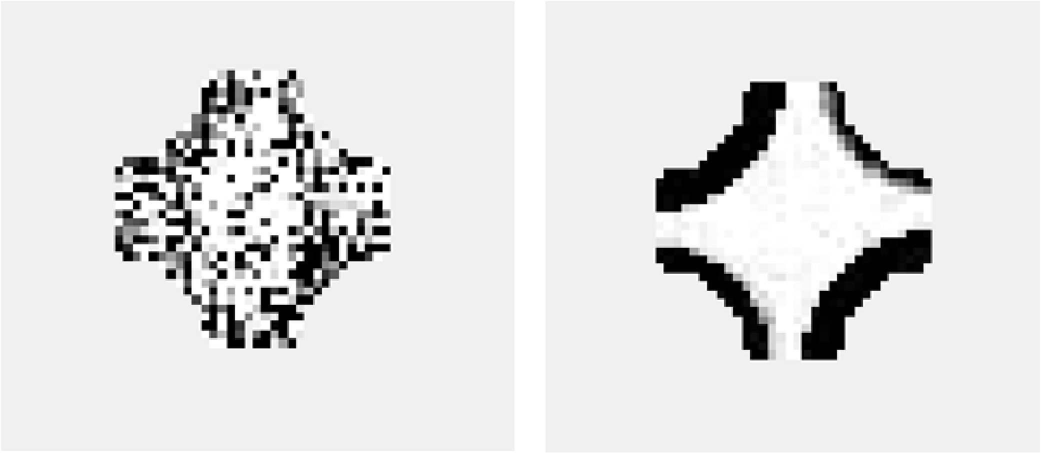

Figure 6.1.14: subchannel void fraction comparison between the raw measurement (left) and the CNN processed reconstruction (right).

Table 11: comparison of the subchannel averaged void measurements.

Actual	CNN	Threshold > 1. 0	Threshold < 0
0.61	0.62	0.61	0.63

The improvement in image quality obtained through the CNN displays the ability of machine learning to reconstruct higher quality images under low scan time and limited view conditions. The improvement in image quality obtained using the CNN demonstrates that 1) the system models developed in this thesis simulate the system well (based on the successful model training) and 2) it is possible to obtain high quality reconstructions under low scan times. Therefore, it is possible to generate representative data for training machine learning models to image more complicated geometries, such as the CANDU bundle, using the noise models developed in this thesis. This application represents the first step in applying machine learning with the fast neutron void fraction imaging system.

Success of the machine learning model is dependent on a dataset representing the imaging properties correctly. The system models developed in this thesis were used to generate representative training data for the CNN, and thus demonstrates the applicability of the models in predicting imaging system parameters. Although there is some minor systematic underprediction, this could be reduced by having more defined set of parameters for spot size (through measurements such as those used by Adams et al. [96]) and the neutron output rate used in the training set. A more defined sample could also improve the minor void threshold dependence. Overall, the image reconstructions as well as the void fraction prediction are greatly improved by the CNN and match the expected void fraction to within 0.01.

In contrast, the McMaster system has spot size and output quantified by the manufacturer which are superior for imaging compared to the Ontario Tech neutron generator. Therefore, it is expected that training with the McMaster system measurements should yield better predictions with higher resolution and with much less noise. Additionally, the training input noise level under the same conditions as the Ontario Tech system would be significantly lower since the McMaster neutron generator has approximately 100 times the neutron output. Therefore, it is also expected that the CNN modelling used in this thesis can be applied to the McMaster data with improved performance.

7 Conclusions and future work

There is no real ending.
It's just the place
where you stop the story.
Frank Herbert

This thesis designed and constructed an FNCT system using a state-of-the-art neutron portable neutron generator, pixelated SiPM detectors, and FPGA processing electronics to provide a transportable method of void fraction measurement for use at thermalhydraulic test facilities, which has not previously been deployed. The design was optimized to provide the greatest resolution and contrast possible based on the component parameters, such as pixel size and emission spot size, as well as analyze practical limitations due to scatter noise parameters such as background and crosstalk. The optimization procedure used a system model that was developed in this thesis. The model incorporates all the noise sources (stochastic, background and crosstalk counts) and source and detector geometries to simulate the imaging process quickly and efficiently for rapid prototyping. This model can be used to rapidly prototype fast neutron imaging designs, or to generate machine learning training data for use in advanced reconstruction algorithms and thus provides a valuable model for the development of fast neutron imaging systems.

Based on this optimization, a methodology was developed to quantify the void fraction measurement capability of FNCT systems using the system model derived in this thesis. Such methodology is lacking in the portable FNCT literature for void fraction measurement where the focus is primarily on resolution. This includes experimental validation, where no void fraction prediction measurements for portable fast neutron systems have been demonstrated. The void fraction measurement performance for the portable FNCT system developed in this thesis, through simulations and experiments, demonstrates that the system is ready for deployment to image complex two-phase flows.

The following sections will provide the summary and conclusions for each part of this work.

7.1 Theoretical and computational analysis of noise and system properties

The imaging process is affected by stochastic noise as well as scattering effects such as crosstalk, background, and object scatter. Historically these were the major impediments for neutron imaging from accelerator driven sources and hence a large amount of numerical and theoretical analysis was done during the design and construction of the system as outlined below.

Simulations were developed using custom MCNP6, MATLAB, and python scripts to quantify the noise properties and the effect that they have on the image acquisition procedure. The simulations quantified the scatter contribution from different laboratory environments and objects as well as the inherent detector crosstalk effect with different applied energy thresholds. An energy threshold of 0.5 MeV was chosen for the system as it is the limiting case for eliminating the bremsstrahlung radiation emitted from the neutron generator.

The ambient background fractions were determined for three testing facilities: McMaster University, Ontario Tech, and Stern Laboratories. The simulations show that the background fraction, B, can be filtered to ~ 0.3 using a selected threshold of 0.5 MeV in each laboratory environment. However, since the Stern Laboratories background fraction varies continuously around the object while rotating, there is no easily definable threshold.

Representative object background scatter noise was also determined for the two void fraction measurement phantoms used in this work: a CANDU geometry and a 2x2 square subchannel. The CANDU object background fraction was found to be a strong function of pressure boundary and insulator material and a weak function of void fraction, due to the limited amount of water content compared to structural materials. The 2x2 square subchannel provided object background fractions below 0.1. The values of both object scatter fraction are estimated to be about half of the value of the background scatter fractions for the CANDU channel and about one fifth for the 2x2 array, for an energy threshold of 0.5 MeV.

A crosstalk kernel was developed using MCNP6 simulations and applied to simulated data. A procedure to introduce crosstalk into simulations was developed by transforming the crosstalk fraction data from MCNP6 into a convolution kernel and applying it to the projection count data in MATLAB. The crosstalk effect was found to be small, and increased the resolution value from 1.67 mm to about 1.87 mm.

The overall effect of the background and object background counts is to reduce contrast in the overall acquisition. Background counts were shown to eliminate the attenuation profile entirely, leading to attenuation of 0 for all detectors as the fraction becomes large (Figure 4.1.24). An ever-increasing object background yields an attenuation profile that becomes flatter, but also becomes negative (Figure 4.1.23). Crosstalk was found to have a small effect on the resolution for the system. Therefore, a procedure was developed to correct the background and object background fraction contributions in the measured count to obtain a correct attenuation measurement during image acquisition. The procedure can be applied in any lab environment and with any test phantom and is necessary for producing accurate image reconstructions.

7.2 Full bundle simulations

The void fraction measurement potential of the FNCT system was quantified using a representative CANDU 37-element bundle geometry and a custom MATLAB script. The simulation generated sinogram data of a randomized void distribution and repeated the sinogram collection process 100 times. The process was repeated to capture the stochastic variations that are present in the image acquisition process. The simulations determined the minimum number of projection angles and scan time per projection that can be used to provide an acceptable void fraction prediction within an acceptable timeframe.

Void fractions were calculated for each reconstruction using reference water filled and air filled CANDU bundle geometries. A single void fraction estimate for each subchannel was calculated by averaging the 100 void maps (average each subchannel average void fraction over the 100 samples). The void fraction standard deviation of the sample was used to quantify the uncertainty in the measurement.

A noticeable underprediction bias was found in predicting void fractions using low scan times. This is due to the thresholding of void fraction to between 0 and 1 to ensure physically realizable values. Due to the noise, however, some pixels exhibited values below 0 and above 1, leading to a bias. The concept of equivalent scan time[6] was used to explore the effect and determine the lower limit of per-projection scan time, in-situ, that minimizes or removes this bias before the full measurements take place. To determine the limit, a sample of 10 projections were

---

[6] Equivalent scan time was used to incorporate the detector pixel summation effect. For example, combining 8 pixels for a per-projection scan time of 5 seconds results in 40 seconds of equivalent scan time.

simulated at a single viewing angle and the standard deviation for each detector was taken. The maximum normalized standard deviation, σ/μ, was used as a metric, and it was found that if a sinogram has a value greater than 0.04, the bias would exist in the data. Therefore, this metric can be used in situ as an upper noise limit for sinogram acquisition, help users adjust scan times if necessary, and help identify if there is bias in the data. In this thesis, 20 seconds of equivalent projection time was determined as the lower projection scan time limit.

Using the sinogram metric, a minimum scan time of 7.5 minutes was determined by selecting 90 angles and reducing the time per projection to 5 s and combining 8 pixels (for an equivalent per projection scan time of 40 s) with RMS errors within 0.04 and relative errors within 10% for all subchannels. It was found that transient flow phenomena (void core and liquid film fluctuations) provide negligible differences in the void prediction in flow regimes under study and therefore the dynamic bias error is negligible for the flow regimes of interest.

7.3 Benchtop scale validation of models

The benchtop validation cases measured representative small-scale phantoms consisting of a rectangular block and 2x2 tube array to validate the simulation models for the FNCT system and to quantify system resolution and void fraction prediction. The resolution was determined to be $\sim$2.1 mm for the McMaster system configuration at a magnification of 1.4 which is expected from theory. Therefore, the resolution value for the final system geometry (magnification of 3.0) of $\sim$1.9 mm based on the developed models is expected to accurately match the resolution of the final system.

Unfortunately, due to a catastrophic neutron generator failure the McMaster system could not be tested further. Instead, imaging tests continued at Ontario Tech using a neutron generator with lower output and larger spot size. The lower output increases the amount of noise present in the image reconstructions, and the larger spot size would produce worse resolution. A small tube array with plastic films of various sizes (to simulate liquid) was imaged using the Ontario Tech neutron generator. The raw images demonstrated the ability to differentiate plastic film (to simulate liquid films) thicknesses of 1 mm, 2 mm, and 3 mm, however the noise level affected the reconstructions greatly. Hence, the void fraction was predicted, but due to the large amount of stochastic noise (due to the low source output) the prediction was dependent on the thresholding of void values to be between 0 and 1.

While the Ontario Tech neutron generator output was sub optimal, and hence image quality generally poor due to neutron output and spot size, the system provided validation data to test the developed noise models. The Ontario tech tests show that the system is reconstructing images and representing the proportions correctly which is clearly demonstrated by the plastic film case. However the void prediction quality is highly dependent on the noise level and void thresholding leading to a large uncertainty and unphysical void variations within the subchannel.

The resolution prediction for the McMaster system was in good agreement with the theoretically expected resolution. It is evident when comparing the McMaster and Ontario Tech imaging acquisitions of a bare tube array (Figure 6.1.3, Figure 6.1.7 and Figure 6.1.4 respectively) that an increase in neutron output and reduction in spot size can be expected to provide better image quality. A simulation of the McMaster system was done to determine this improvement for the Ontario Tech imaging parameters and demonstrated the image quality and void prediction improvement when a smaller spot size and higher output generator is used.

7.4 Machine learning application

The raw images produced by the Ontario Tech system were excessively noisy due to the limited acquisition time, and therefore a CNN was applied to improve the image quality of the measurements. The system models developed in this thesis were used to generate representative training data for the CNN. The resulting image reconstruction outputs as well as the void fraction predictions are greatly improved and match the expected void fraction to within 0.01. The improvement in image quality obtained using the CNN demonstrates that the system models developed in this thesis simulate the system well (based on the successful model training). Therefore, the models developed in this thesis can be used to generate representative data for training machine learning models. For example, a CNN can be trained using the noise models developed in this thesis to predict the subchannel void fraction (and perhaps liquid film thicknesses) in more complicated geometries, such as the CANDU bundle. The application of machine learning in this thesis represents the first step in applying machine learning to void fraction prediction using the FNCTS.

Although some void thresholding dependence exists, this can be remedied through more specific knowledge of the spot size and neutron output characteristics of the Ontario Tech generator. The neutron output was not measured using a baseline, and the spot size was not known with certainty, and without knowing the target design, it is difficult to estimate without a manufacturer's specification. In contrast the McMaster generator has a measured spot size and higher output that can be used 1) to define a more specific training set for a CNN model and 2) provide less statistical error due to a higher count rate. The base reconstructions and therefore the CNN model performance will further improve when using the McMaster system output as training data.

7.5 Summary

This thesis developed models and methods to assess the FNCT system capabilities, including the impact of the dominant noise sources on the reconstruction quality and void fraction prediction. Void fraction prediction simulations of the McMaster FNCT system show that a minimum scan time of $\sim$ 7.5 minutes is achievable. The simulations were also used to derive an in-situ measurement technique to ensure that a void underprediction bias that was prevalent at low per-projection scan times can be avoided.

Benchtop tests were done at two facilities – McMaster and Ontario Tech – to generate data to validate the models and quantify the system performance. The McMaster system resolution was measured and agreed with the expected resolution and the final system is therefore estimated to have a resolution of ∼1.7 mm to 1.9 mm.

Due to a catastrophic failure of the McMaster neutron generator, experiments were continued at Ontario Tech. While the Ontario Tech neutron generator output was sub optimal in terms of neutron output and spot size, the system provided further validation data to test the developed noise models. To improve the image quality, and test the accuracy of the noise models, a machine learning model was trained using simulated phantoms that applied the noise models. The trained machine learning model was applied to the measured images from the Ontario Tech generator and showed remarkable improvement. While the full system could not be tested due to a generator failure, the final system analysis using the models developed in this thesis shows very promising performance.

This thesis is the culmination of a significant effort to develop a fast neutron computed tomography system capable of providing subchannel void fraction information. The fast neutron system developed in this thesis provides a valuable measurement system for non-destructive measurements that can provide the necessary void information required by nuclear safety analysis codes.

7.6 Future work

This work has demonstrated the important features and trade-offs of a practical fast neutron CT system which include:

- Source and detector geometry
- Noise effects
- Scan time
- Reconstruction grid pixel size

Some suggestions for improvements in each of these categories are provided in this section together with some other categories that would provide significant benefit logistically.

7.6.1 Source geometry

Neutron generators in general have a large spot size than a typical Xray-CT system and spot size greatly affects image blur. Moving the source-object distance to large values decreases the blur caused by finite spot sizes but also decreases detector counts and magnification, all other things being equal. While smaller spot sizes for neutron generators may be possible, the heat load on the target becomes an issue and hence future developments of generators (such as rotating targets) will be needed to further reduce spot size. More complex cooling apparatus are being developed to provide more effective cooling to shrink spot size while maintaining high output [120], so future generators may provide the necessary high outputs with the required small spot sizes. Such generator technology can be developed in-house at McMaster University or developed in collaboration with commercial vendors or universities.

7.6.2 Detector geometry

Detector physical geometry/size which affects the ultimate reconstruction resolution (smaller sizes are better) and count rates per pixel (i.e., small detectors have lower counts, all other things being equal, which leads to longer scan times). Physical detector size also affects costs since the number of SiPM and processing electronics increases significantly with decreasing physical detector pixel size. A reduction of pixel size below 1 mm is not recommended on the grounds of the proton bleed effect, and the significant reduction in count rates (increasing the necessary scan time for good image quality). It is possible to reduce the pixel size with a detailed charge locating multiplexing system, but such a system would require altering the detector electronics significantly.

7.6.3 Noise reduction

The background counts in the neutron imaging process provides a significant amount of noise that needs to be accounted for in post-processing. Some methods can be used to limit this contribution to the signal and reduce the amount of background scatter counts present in the detector measurement before post-processing:

Collimators: collimators for neutron systems, such as the one used by Joyce et al. [118], can reduce or remove the background count contribution to the detector measurement. The collimator is useful for a benchtop setup, or systems where large source to object distances can be tolerated since the dimensions of the collimator tend to be large (the neutron path through material is long).

Associated particle imaging (API): associated particle imaging uses the reaction of the neutron generator to track which neutrons are direct and which are scattered contributions. The API method measures the direction of the alpha particle that is emitted in coincidence with the neutron in the D-D fusion reaction using a position sensitive alpha detector located on the back side of the emission direction. Based on the time of flight and direction between the detected alpha particle and detected neutron, the scattered neutron counts can be rejected. For example this method has been used in simulation to show the improvement of the image reconstruction [143]. Such methods reduce the amount of necessary post-processing of the data but increase costs.

The implementation of an API system would eliminate the dependence of the detector response to background, object, and crosstalk counts, thus removing the constraint on scintillator thickness and the requirement of an energy threshold to suppress noise counts. The full efficiency of the scintillator can therefore be utilized, which increases the efficiency of the detector by approximately a factor of 2 and thereby reduces the statistical counting noise. Thus with API one can achieve almost noiseless CT measurements.

A combination of API systems and enhanced target design [120] can therefore improve the detection rate of direct neutrons by 20 times. Lastly, the resolution of the system would be improved since a) smaller detector areas can be used since particle tracking can identify the initiating pixel event and eliminate proton bleed and b) crosstalk can be eliminated. Therefore, detector pixel sizes of 1 mm or less can be used, thus enhancing resolution, and limiting spot size effects if lower magnifications are used (note that lower magnifications are possible due to no scatter noise effects while using the API system).

7.6.4 Scan time reduction

Scan times can be reduced via improvements in technology (e.g., neutron generator output, reconstruction algorithms) or by incorporating less moving parts (e.g., by using multiple generators, similar to the X-ray system design by Hori et al. [42]). Neutron generators have increased effective output by over 2 orders of magnitude since 2016, and further development in target design and cooling may mean that generators using spinning target designs [120], similar to those used in X-ray tubes, can provide even higher outputs with smaller spot sizes. With higher output generators coupled to an API system, many neutron generators can be placed around a test object and actuated in series to provide faster scan times with significantly reduced noise (albeit with significantly higher cost).

Machine learning algorithms may provide a less costly solution for scan time reduction. As shown in this thesis, machine learning can significantly improve image quality under low scan time (high stochastic noise) conditions. Machine learning algorithms can be trained on representative data (generated using the models developed in this thesis for example) to reconstruct images in a cost-effective way. This method of reduced scan time imaging has been a focal point in the medical industry to reduce patient dose rates while maintaining diagnostic quality as outlined in the review by Lell and Kachelrieß [144]. The review highlights the trajectory from the traditional iterative image reconstruction methods for low dose imaging to the state-of-the-art solutions using deep learning models.

Deep learning models are interesting since they present an option to not only reduce scan times, but to also improve image quality by increasing resolution and/or removing artifacts. The application of deep learning in the medical industry is new and active. Leveraging the experience and techniques already developed by the medical industry can help reduce the scan times for the current system while maintaining or improving image quality.

7.6.5 Reconstruction measurement improvements

Overall improvements in masking and reconstruction meshing can eliminate any effects of masking circular pins with square pixels. Such conformal meshes have been successfully used for image reconstructions for BWR two-phase flow [65]. Such meshes can be used in conjunction with noise elimination of CNN models to improve the void prediction through more accurate masking on curved surfaces (through the conformal mesh). Such meshing can be effectively used only when the location and sizes of pins are known. For example, thermal expansion occurs when the pins are heated and therefore an image registration algorithm is required to adjust for this. An example of a registration algorithm for a double subchannel geometry was used by Bolesch et al. [54]. The application of image registration in CANDU bundles is more complicated, due to the number of subchannels, although it could be possible to correct the image on a subchannel by subchannel (local) level. This could be done through general image registration techniques using an optimization function criterion (such as gradient descent with a mean squared error minimization) or through machine learning models.

7.6.6 Detector maintenance

An exploration for potential detector drift due to radiation damage or long count times can be quantified more thoroughly in the future by monitoring detector count output over time through tracking the bias voltage (detector gain) required to obtain correct count rates/uniformity. This can quantify the noise for inclusion in the model for when the counting statistics may not be the most dominant error source.

7.6.7 Collaboration

Improvements in the device can be realized through collaboration with other laboratories and companies. Several laboratories and companies have been investigating the use of neutron generators for object interrogation, for example at LLNL [145] and ORNL [146]. It would be beneficial to the system development to attempt these connections to build out the system and develop broader group expertise.

8 References

[1] "World Energy Outlook 2021," 2021. Accessed: Nov. 25, 2022. [Online]. Available: www.iea.org/weo.

[2] "Nuclear power plants - Canadian Nuclear Safety Commission." https://www.cnsc-ccsn.gc.ca/eng/reactors/power-plants/index.cfm (accessed Nov. 25, 2022).

[3] R. A. Fortman, G. I. Hadaller, R. C. Hamilton, R. C. Hayes, K. S. Shin, and F. Stern, "A new facility for the determination of critical heat flux in nuclear fuel assemblies," 1993.

[4] N. E. Todreas and M. S. Kazimi, "Nuclear Systems: Vol. 1," *Fr. Taylor*, 1990.

[5] A. A. Harms and F. A. R. Laratta, "The dynamic-bias in radiation interrogation of two-phase flow," *Int. J. Heat Mass Transf.*, 1973, doi: 10.1016/0017-9310(73)90152-X.

[6] G. Yadigaroglu and G. F. Hewitt, *Introduction to multiphase flow: basic concepts, applications and modelling*. Springer, 2017.

[7] R. T. Lahey, B. S. Shiralkar, D. W. Radcliffe, and E. E. Polomik, *Out-of-Pile Subchannel Measurements in a Nine-Rod Bundle for Water At 1000 Psia*. Pergamon Press, 1972.

[8] G. D. McPherson, "THE USE OF ENTHALPY IMBALANCE IN EVALUATING THE DRYOUT PERFORMANCE OF FUEL BUNDLES," Chalk River, ON, 1971.

[9] M. Tayal and M. Gacesa, "Chapter 17: Fuel," *Essent. CANDU*, no. December 2014, 2014.

[10] B. Neykov, F. Aydogan, L. Hochreiter, K. Ivanov, and M. Martin, “BWR Full-size Fine-mesh Bundle Test (BFBT) Benchmark Volume I: Specifications,” 2006.

[11] A. Rubin, A. Schoedel, M. Avramova, H. Utsuno, S. Bajorek, and A. Velazquez-Lozada, “OECD/NRC Benchmark Based on NUPEC PWR Sub-channel and Bundle Tests (PSBT) Volume I: Experimental Database and Final Problem Specifications NUCLEAR ENERGY AGENCY Organisation for Economic Co-operation and Development,” 2012, Accessed: Nov. 02, 2022. [Online]. Available: http://www.nea.fr/html/science/egrsltb/PSBT/.

[12] B. J. Yun, G. C. Park, J. E. Julia, and T. Hibiki, “Flow structure of subcooled boiling water flow in a subchannel of 3 × 3 rod bundles,” *J. Nucl. Sci. Technol.*, vol. 45, no. 5, pp. 402–422, 2008, doi: 10.1080/18811248.2008.9711450.

[13] S. Paranjape, M. Ishii, and T. Hibiki, “Modeling and measurement of interfacial area concentration in two-phase flow,” *Nucl. Eng. Des.*, vol. 240, no. 9, pp. 2329–2337, 2010, doi: 10.1016/j.nucengdes.2009.11.009.

[14] X. Yang, J. P. Schlegel, Y. Liu, S. Paranjape, T. Hibiki, and M. Ishii, “Experimental study of interfacial area transport in air-water two phase flow in a scaled 8×8 BWR rod bundle,” *Int. J. Multiph. Flow*, vol. 50, no. 2013, pp. 16–32, 2013, doi: 10.1016/j.ijmultiphaseflow.2012.10.006.

[15] Q. yao Ren, L. ming Pan, W. xiong Zhou, S. jia Du, and Z. chun Li, “Phase distribution characteristics of bubbly flow in 5 × 5 vertical rod bundles with mixing vane spacer grids,” *Exp. Therm. Fluid Sci.*, vol. 96, no. December 2017, pp. 451–459, 2018, doi: 10.1016/j.expthermflusci.2018.04.002.

[16] X. Han, X. Shen, T. Yamamoto, K. Nakajima, H. Sun, and T. Hibiki, “Experimental study on local interfacial parameters in upward air-water bubbly flow in a vertical 6 × 6 rod bundle,” *Int. J. Heat Mass Transf.*, vol.

144, p. 118696, Dec. 2019, doi: 10.1016/J.IJHEATMASSTRANSFER.2019.118696.

[17] X. Shen, S. Miwa, Y. Xiao, X. Han, and T. Hibiki, “Local measurements of upward air-water two-phase flows in a vertical 6×6 rod bundle,” *Exp. Comput. Multiph. Flow 2019 13*, vol. 1, no. 3, pp. 186–200, Jun. 2019, doi: 10.1007/S42757-019-0031-0.

[18] S. Hosokawa, K. Hayashi, and A. Tomiyama, “Void distribution and bubble motion in bubbly flows in a 4×4 rod bundle. Part I: Experiments,” *J. Nucl. Sci. Technol.*, vol. 51, no. 2, pp. 220–230, 2014, doi: 10.1080/00223131.2013.862189.

[19] U. P. M. Senaratne and L. K. H. Leung, “Void Fraction Distribution In A Horizontal 37- Element Bundle,” pp. 1–12, 2005.

[20] J. M. Le Corre, “Experimental investigation and modeling of void drift in modern BWR fuel designs,” *Nucl. Eng. Des.*, vol. 341, no. July 2018, pp. 259–268, 2019, doi: 10.1016/j.nucengdes.2018.11.011.

[21] J. M. Le Corre, “Experimental characterization of boiling two-phase flow structures under BWR core operating conditions,” *Nucl. Eng. Des.*, vol. 365, p. 110708, Aug. 2020, doi: 10.1016/J.NUCENGDES.2020.110708.

[22] H. M. Prasser, A. Böttger, and J. Zschau, “A new electrode-mesh tomograph for gas-liquid flows,” *Flow Meas. Instrum.*, vol. 9, no. 2, pp. 111–119, 1998, doi: 10.1016/S0955-5986(98)00015-6.

[23] I. D. Johnson, “Method and Apparatus for Measuring Water in Crude Oil, United States Patent, No , Date of Patent: , 1987,” 1987.

[24] H. M. Prasser, J. Zschau, D. Peters, G. Pietzsch, W. Taubert, and M. Trepte, “Wire-mesh sensor - now 10,000 frames per second,” *Inst. Saf. Res.*, vol. 15, pp. 15–18, 2000.

[25] U. Hampel *et al.*, “A Review on Fast Tomographic Imaging Techniques and Their Potential Application in Industrial Process Control,” 2022.

[26] A. Ylönen, W. M. Bissels, and H. M. Prasser, “Single-phase cross-mixing measurements in a 4 × 4 rod bundle,” *Nucl. Eng. Des.*, vol. 241, no. 7, pp. 2484–2493, 2011, doi: 10.1016/j.nucengdes.2011.04.014.

[27] A. Ylönen, “High-resolution flow structure measurements in a rod bundle,” 2013.

[28] S. Liu, L. Liu, H. Gu, and K. Wang, “Experimental study of gas-liquid flow patterns and void fraction in prototype 5 × 5 rod bundle channel using wire-mesh sensor,” *Ann. Nucl. Energy*, vol. 171, p. 109022, 2022, doi: 10.1016/j.anucene.2022.109022.

[29] H. Pietruske and H.-M. Prasser, “Wire-mesh sensors for high-resolving two-phase flow studies at high pressures and temperatures,” *Flow Meas. Instrum.*, vol. 18, no. 2, pp. 87–94, 2007, doi: 10.1016/j.flowmeasinst.2007.01.004.

[30] T. Arai, M. Furuya, T. Kanai, and K. Shirakawa, “Development of a subchannel void sensor and two-phase flow measurement in 10×10 rod bundle,” *Int. J. Multiph. Flow*, vol. 47, pp. 183–192, 2012, doi: 10.1016/j.ijmultiphaseflow.2012.07.012.

[31] T. Arai, M. Furuya, T. Kanai, and K. Shirakawa, “Development of a Multi-Dimensional Measurement Sensor of Void Fraction and Phasic Velocity for Boiling Two-Phase Flow,” pp. 1–8, 2014.

[32] T. Arai, M. Furuya, and K. Shirakawa, “Development of Subchannel Void Sensor for Wide Pressure and Temperature Ranges and Its Application to Boiling Flow Dynamics in a Heated Rod Bundle,” *Nucl. Technol.*, vol. 208, no. 2, pp. 203–221, 2022, doi: 10.1080/00295450.2021.1897733.

[33] T. Arai, M. Furuya, H. Takiguchi, Y. Nishi, and K. Shirakawa, “Void-

fraction measurement with high spatial resolution in a 5×5 rod bundle by linear-accelerator-driven X-ray computed tomography over a wide pressure range," *Flow Meas. Instrum.*, vol. 69, no. November 2018, p. 101614, 2019, doi: 10.1016/j.flowmeasinst.2019.101614.

[34] C. Tompkins, H. M. Prasser, and M. Corradini, "Wire-mesh sensors: A review of methods and uncertainty in multiphase flows relative to other measurement techniques," *Nucl. Eng. Des.*, vol. 337, no. May, pp. 205–220, 2018, doi: 10.1016/j.nucengdes.2018.06.005.

[35] S. W. Chen *et al.*, "Experimental investigation on local/global void distribution of air-water two-phase flow in a 3 × 3 rod bundle channel under low-flow conditions," *Int. J. Heat Fluid Flow*, vol. 85, no. December 2019, p. 108623, 2020, doi: 10.1016/j.ijheatfluidflow.2020.108623.

[36] M. Damsohn and H.-M. Prasser, "Experimental studies of the effect of functional spacers to annular flow in subchannels of a BWR fuel element," *Nucl. Eng. Des.*, vol. 240, no. 10, pp. 3126–3144, Oct. 2010, doi: 10.1016/j.nucengdes.2010.05.032.

[37] S. Morooka, T. Ishizuka, M. Iizuka, and K. Yoshimura, "Experimental study on void fraction in a simulated BWR fuel assembly (evaluation of cross-sectional averaged void fraction)," *Nucl. Eng. Des.*, 1989, doi: 10.1016/0029-5493(89)90128-3.

[38] T. Mitsutake, S. Morooka, K. Suzuki, S. Tsunoyama, and K. Yoshimura, "Void fraction estimation within rod bundles based on three-fluid model and comparison with x-ray CT void data," *Nucl. Eng. Des.*, vol. 120, no. 2–3, pp. 203–212, Jun. 1990, doi: 10.1016/0029-5493(90)90373-6.

[39] A. Inoue, T. Kurosu, T. Aoki, M. Yagi, T. Mitsutake, and S. ichi Morooka, "Void fraction distribution in BWR fuel assembly and evaluation of subchannel code," *J. Nucl. Sci. Technol.*, 1995, doi:

10.1080/18811248.1995.9731754.

[40] K. Hori, T. Fujimoto, and K. Kawanishi, “Development of ultrafast Xray computed tomography scanner,” 1998.

[41] K. Hori, K. Kawanishi, H. Hamamura, M. Ochi, and M. Akai, “A high speed X-ray computed tomography scanner for multipurpose flow visualization and measurement,” *4TH Int. Top. Meet. Nucl. Therm. Hydraul. Oper. Saf.*, 1994, Accessed: Sep. 10, 2018. [Online]. Available: https://inis.iaea.org/search/search.aspx?orig_q=RN:35097899.

[42] K. Hori, T. Fujimoto, K. Kawanishi, and H. Nishikawa, “Development of an ultrafast X-ray computed tomography scanner system: Application for measurement of instantaneous void distribution of gas-liquid two-phase flow,” *Heat Transf. - Asian Res.*, vol. 29, no. 3, pp. 155-165*, 2000, doi: 10.1002/(SICI)1523-1496(200005)29:3<155::AID-HTJ1>3.0.CO;2-M.

[43] H. M. Prasser, M. Misawa, and I. Tiseanu, “Comparison between wire-mesh sensor and ultra-fast X-ray tomograph for an air-water flow in a vertical pipe,” *Flow Meas. Instrum.*, 2005, doi: 10.1016/j.flowmeasinst.2005.02.003.

[44] U. Hampel *et al.*, “Experimental ultra fast X-ray computed tomography with a linearly scanned electron beam source,” *Flow Meas. Instrum.*, vol. 16, no. 2–3, pp. 65–72, 2005, doi: 10.1016/j.flowmeasinst.2005.02.002.

[45] M. Bieberle and U. Hampel, “Evaluation of a limited angle scanned electron beam x-ray CT approach for two-phase pipe flows,” *Meas. Sci. Technol.*, 2006, doi: 10.1088/0957-0233/17/8/001.

[46] M. Bieberle *et al.*, “Ultrafast limited-angle-type x-ray tomography,” *Appl. Phys. Lett.*, vol. 91, no. 12, 2007, doi: 10.1063/1.2787879.

[47] M. Bieberle *et al.*, “Dual-plane ultrafast limited-angle electron beam x-ray tomography,” *Flow Meas. Instrum.*, 2010, doi:

10.1016/j.flowmeasinst.2009.12.001.

[48] F. Fischer *et al.*, “An ultra fast electron beam x-ray tomography scanner,” *Meas. Sci. Technol.*, vol. 19, no. 9, 2008, doi: 10.1088/0957-0233/19/9/094002.

[49] F. Fischer and U. Hampel, “Ultra fast electron beam X-ray computed tomography for two-phase flow measurement,” 2010, doi: 10.1016/j.nucengdes.2009.11.016.

[50] M. Banowski, M. Beyer, L. Szalinski, and D. Lucas, “Comparative study of ultrafast X-ray tomography and wire-mesh sensors for vertical gas–liquid pipe flows,” *Flow Meas. Instrum.*, vol. 53, pp. 95–106, Mar. 2017, doi: 10.1016/J.FLOWMEASINST.2016.02.001.

[51] F. Barthel, M. Bieberle, D. Hoppe, M. Banowski, and U. Hampel, “Velocity measurement for two-phase flows based on ultrafast X-ray tomography,” *Flow Meas. Instrum.*, vol. 46, pp. 196–203, 2015, doi: 10.1016/j.flowmeasinst.2015.06.006.

[52] K. Katono, J. Nukaga, K. Fujimoto, T. Nagayoshi, and K. Yasuda, “Three-dimensional time-averaged void fraction distribution measurement technique for BWR thermal hydraulic conditions using an X-ray CT system,” *J. Nucl. Sci. Technol.*, 2015, doi: 10.1080/00223131.2014.952699.

[53] J. Nukaga, K. Katono, N. Sadaoka, K. Yasuda, and T. Aoki, “Investigation on applicability of time-averaged X-ray CT images in two-phase flow measurement,” *J. Nucl. Sci. Technol.*, vol. 56, no. 12, pp. 1130–1140, 2019, doi: 10.1080/00223131.2019.1644245.

[54] C. Bolesch, L. Robers, R. Adams, and H. M. Prasser, “Non-adiabatic annular flow experiments in a subchannel geometry with spacer grid,” *Nucl. Eng. Des.*, vol. 356, no. October 2019, p. 110378, 2020, doi: 10.1016/j.nucengdes.2019.110378.

[55] R. Zboray, C. Bolesch, and H.-M. Prasser, "Development of neutron and X-ray imaging techniques for nuclear fuel bundle optimization," *Nucl. Eng. Des.*, May 2017, doi: 10.1016/j.nucengdes.2017.04.035.

[56] L. Robers, R. Adams, C. Bolesch, and H. M. Prasser, "Time averaged tomographic measurements before and after dryout in a simplified BWR subchannel geometry," *Nucl. Eng. Des.*, vol. 380, no. November 2020, p. 111295, 2021, doi: 10.1016/j.nucengdes.2021.111295.

[57] T. Arai *et al.*, "Effect of nonheated rod arrangements on void fraction distribution in a rod bundle in high-pressure boiling flow," *Nucl. Eng. Des.*, vol. 402, p. 112101, Feb. 2023, doi: 10.1016/J.NUCENGDES.2022.112101.

[58] A. Nava-Dominguez, Y. F. Rao, and G. M. Waddington, "Assessment of subchannel code ASSERT-PV for flow-distribution predictions," *Nucl. Eng. Des.*, vol. 275, pp. 122–132, 2014, doi: 10.1016/j.nucengdes.2014.05.001.

[59] O. Nylund *et al.*, "HYDRODYNAMIC AND HEAT TRANSFER MEASUREMENTS ON A FULL-SCALE SIMULATED 36-ROD MARVIKEN FUEL ELEMENT WITH UNIFORM HEAT FLUX DISTRIBUTION.," 1968.

[60] K. Hori, K. Miyazaki, T. Kurosu, S. Sugiyama, J. Matsumoto, and Y. Akiyama, "In bundle void fraction measurement of PWR fuel assembly," 1993, Accessed: Aug. 23, 2022. [Online]. Available: http://inis.iaea.org/Search/search.aspx?orig_q=RN:25058803.

[61] K. Hori, Y. Akiyama, and K. Miyazaki, "Void fraction in a single channel simulating one subchannel of a PWR fuel assembly," *Two-Phase Flow Model. Exp.*, pp. 1013–1027, 1995, [Online]. Available: http://www.oecd-nea.org/science/egrsltb/PSBT/Ref.(3) Void Fraction in A Single Channel Simulating One Subchannel of A PWR Fuel Assembly (1995).pdf.

[62] Y. Akiyama, K. Hori, K. Miyazaki, K. Mishima, and S. Sugiyama,

"Pressurized water reactor fuel assembly subchannel void fraction measurement," *Nucl. Technol.*, vol. 112, no. 3, pp. 412–421, 1995, doi: 10.13182/NT95-A35167.

[63] A. Rubin, M. Avramova, and H. Utsuno, "OECD/NRC benchmark based on nupec PWR subchannel and bundle tests (PSBT)," 2010.

[64] G. Windecker and H. Anglart, "Phase Distribution in a BWR Fuel Assembly and Evaluation of a Multidimensional Multifield Model," *Nucl. Technol.*, vol. 134, no. 1, pp. 49–61, 2001, doi: 10.13182/NT01-A3185.

[65] J. Le Corre, "ITERATIVE COMPUTER TOMOGRAPHY RECONSTRUCTION OF VOID FRACTION IN A FUEL BUNDLE ON UNSTRUCTURED MESH," 2022.

[66] A. Bieberle, D. Hoppe, E. Schleicher, and U. Hampel, "Void measurement using high-resolution gamma-ray computed tomography," *Nucl. Eng. Des.*, vol. 241, no. 6, pp. 2086–2092, Jun. 2011, doi: 10.1016/j.nucengdes.2011.03.028.

[67] R. Adams, V. Petrov, and A. Manera, "Advanced Radiation-Based Imaging Techniques for Detailed Void Fraction Measurements in High-Pressure Flow Loops," 2017.

[68] U. Hampel *et al.*, "High resolution gamma ray tomography scanner for flow measurement and non-destructive testing applications," *Rev. Sci. Instrum.*, vol. 78, no. 10, p. 103704, Oct. 2007, doi: 10.1063/1.2795648.

[69] R. Adams, J. Diaz, V. Petrov, and A. Manera, "Development and testing of a high resolution fan-beam gamma tomography system with a modular detector array," *Nucl. Instruments Methods Phys. Res. Sect. A Accel. Spectrometers, Detect. Assoc. Equip.*, vol. 942, no. March, p. 162346, 2019, doi: 10.1016/j.nima.2019.162346.

[70] R. Adams, J. Diaz, V. Petrov, and A. Manera, “Simulation and experiments on the feasibility of using gamma tomography for void fraction measurements in nuclear fuel bundle mock-ups,” *Ann. Nucl. Energy*, vol. 154, p. 108073, 2021, doi: 10.1016/j.anucene.2020.108073.

[71] J. Diaz, R. Adams, V. Petrov, and A. Manera, “DETAILED MEASUREMENTS OF VOID-FRACTION DISTRIBUTION IN AN ADIABATIC FUEL BUNDLE PERFORMED WITH HIGH RESOLUTION GAMMA-RAY TOMOGRAPHY IMAGING,” 2019.

[72] R. Adams, R. Zboray, and H.-M. Prasser, “A novel fast-neutron tomography system based on a plastic scintillator array and a compact D–D neutron generator,” *Appl. Radiat. Isot.*, vol. 107, pp. 1–7, Jan. 2016, doi: 10.1016/j.apradiso.2015.09.002.

[73] Z. Cheng, Y. F. Rao, and G. M. Waddington, “Assessment of Assert-PV void fraction and CHF predictions against PSBT Benchmark,” *17th Int. Top. Meet. Nucl. React. Therm. Hydraul. NURETH 2017*, vol. 2017-Septe, no. September, 2017.

[74] K. Mishima, T. Hibiki, and H. Nishihara, “Visualization and measurement of two-phase flow by using neutron radiography,” *Nucl. Eng. Des.*, vol. 175, no. 1–2, pp. 25–35, Nov. 1997, doi: 10.1016/S0029-5493(97)00159-3.

[75] G. D. Harvel, K. Hori, K. Kawanishi, and J. S. Chang, “Real-time cross-sectional averaged void fraction measurements in vertical annulus gas-liquid two-phase flow by neutron radiography and X-ray tomography techniques,” *Nucl. Instruments Methods Phys. Res. Sect. A Accel. Spectrometers, Detect. Assoc. Equip.*, 1996, doi: 10.1016/0168-9002(95)00807-1.

[76] A. A. Harms, S. Lo, and W. T. Hancox, “Measurement of Time-Averaged Voids by Neutron Diagnosis,” *J. Appl. Phys.*, vol. 42, no. 10, pp. 4080–4082, 1971.

[77] C. Lani and R. Zboray, “Development of a high frame rate neutron imaging method for two-phase flows,” *Nucl. Instruments Methods Phys. Res. Sect. A Accel. Spectrometers, Detect. Assoc. Equip.*, vol. 954, p. 161707, Feb. 2020, doi: 10.1016/J.NIMA.2018.12.022.

[78] I. C. Lim *et al.*, “Measurement of the void fraction in a channel simulating the HANARO fuel assembly using neutron radiography,” *Nucl. Instruments Methods Phys. Res. Sect. A Accel. Spectrometers, Detect. Assoc. Equip.*, vol. 542, no. 1–3, pp. 181–186, Apr. 2005, doi: 10.1016/J.NIMA.2005.01.097.

[79] G. D. Harvel, J. S. Chang, and V. S. Krishnan, “Investigation of large amplitude stratified waves in a CANDU-type 37 rod nuclear fuel channel by a real-time neutron radiography technique,” *Nucl. Eng. Des.*, vol. 200, no. 1–2, pp. 221–231, Aug. 2000, doi: 10.1016/S0029-5493(99)00330-1.

[80] N. Takenaka, H. Asano, T. Fujii, M. Mizubata, and K. Yoshii, “Application of fast neutron radiography to three-dimensional visualization of steady two-phase flow in a rod bundle,” *Nucl. Instruments Methods Phys. Res. Sect. A Accel. Spectrometers, Detect. Assoc. Equip.*, vol. 424, no. 1, pp. 73–76, Nov. 1999, doi: 10.1016/S0168-9002(98)01322-9.

[81] N. Takenaka and H. Asano, “Quantitative CT-reconstruction of void fraction distributions in two-phase flow by neutron radiography,” *Nucl. Instruments Methods Phys. Res. Sect. A Accel. Spectrometers, Detect. Assoc. Equip.*, vol. 542, no. 1–3, pp. 387–391, Apr. 2005, doi: 10.1016/J.NIMA.2005.01.166.

[82] M. Kureta, “Experimental Study of Three-Dimensional Void Fraction Distribution in Heated Tight-Lattice Rod Bundles Using Three-Dimensional Neutron Tomography,” *J. Power Energy Syst.*, vol. 1, no. 3, pp. 225–238, 2007, doi: 10.1299/jpes.1.225.

[83] M. Kureta, “Development of a neutron radiography three-dimensional computed tomography system for void fraction measurement of boiling flow

in tight lattice rod bundles," *J. Power Energy Syst.*, vol. 1, no. 3, pp. 211–224, 2007.

[84] M. Kureta, H. Tamai, H. Yoshida, A. Ohnuki, and H. Akimoto, "Development of design technology on thermal-hydraulic performance in tight-lattice rod bundles: V-estimation of void fraction," *J. Power Energy Syst.*, vol. 2, no. 1, pp. 271–282, 2008.

[85] R. Zboray, J. Kickhofel, M. Damsohn, and H.-M. Prasser, "Cold-neutron tomography of annular flow and functional spacer performance in a model of a boiling water reactor fuel rod bundle," *Nucl. Eng. Des.*, vol. 241, no. 8, pp. 3201–3215, Aug. 2011, doi: 10.1016/J.NUCENGDES.2011.06.029.

[86] J. L. Kickhofel, R. Zboray, M. Damsohn, A. Kaestner, E. H. Lehmann, and H. M. Prasser, "Cold neutron tomography of annular coolant flow in a double subchannel model of a boiling water reactor," *Nucl. Instruments Methods Phys. Res. Sect. A Accel. Spectrometers, Detect. Assoc. Equip.*, vol. 651, no. 1, pp. 297–304, 2011, doi: 10.1016/j.nima.2011.01.062.

[87] R. Zboray and H. M. Prasser, "Measuring liquid film thickness in annular two-phase flows by cold neutron imaging," *Exp. Fluids*, vol. 54, no. 9, 2013, doi: 10.1007/s00348-013-1596-1.

[88] R. Zboray, C. Bolesch, and H.-M. Prasser, "Development of neutron and X-ray imaging techniques for nuclear fuel bundle optimization," *Nucl. Eng. Des.*, vol. 336, pp. 24–33, Sep. 2017, doi: 10.1016/J.NUCENGDES.2017.04.035.

[89] M. Taylor, E. Sengbusch, C. Seyfert, E. Moll, and R. Radel, "Thermal Neutron Radiography using a High-flux Compact Neutron Generator," 2017, doi: 10.1016/j.phpro.2017.06.024.

[90] J. R. Buell, D. . Byskal, M. R. Desrosiers, E. M. A. Hussein, P. J. Ingham, and R. S. Swartz, "A neutron scatterometer for void-fraction measurement

in heated rod-bundle channels under CANDU LOCA conditions," *Int. J. Multiph. Flow*, vol. 31, no. 4, pp. 452–472, Apr. 2005, doi: 10.1016/j.ijmultiphaseflow.2005.01.004.

[91] E. Hussein, D. L. Bot, S. Banerjee, and D. A. Meneley, "Design Aspects of a Fast Neutron Scattering Technique for Phase Distribution Measurement in Two-Phase Flow," in *Measuring Techniques in Gas-Liquid Two-Phase Flows*, 1984.

[92] P. Andersson, E. Andersson-Sunden, H. Sjöstrand, and S. Jacobsson-Svärd, "Neutron tomography of axially symmetric objects using 14 MeV neutrons from a portable neutron generator," *Rev. Sci. Instrum.*, 2014, doi: 10.1063/1.4890662.

[93] P. Andersson, J. Valldor-Blücher, E. Andersson Sundén, H. Sjöstrand, and S. Jacobsson-Svärd, "Design and initial 1D radiography tests of the FANTOM mobile fast-neutron radiography and tomography system," *Nucl. Instruments Methods Phys. Res. Sect. A Accel. Spectrometers, Detect. Assoc. Equip.*, vol. 756, pp. 82–93, 2014, doi: 10.1016/j.nima.2014.04.052.

[94] P. Andersson, "Fast-Neutron Tomography using a Mobile Neutron Generator for Assessment of Steam-Water Distributions in Two-Phase Flows," Acta Universitatis Upsaliensis, 2014.

[95] R. Adams, R. Zboray, M. Cortesi, and H.-M. Prasser, "Conceptual design and optimization of a plastic scintillator array for 2D tomography using a compact D–D fast neutron generator," *Appl. Radiat. Isot.*, vol. 86, pp. 63–70, Apr. 2014, doi: 10.1016/j.apradiso.2014.01.001.

[96] R. Adams, L. Bort, R. Zboray, and H. M. Prasser, "Development and characterization of a D-D fast neutron generator for imaging applications," *Appl. Radiat. Isot.*, 2015, doi: 10.1016/j.apradiso.2014.11.017.

[97] R. E. Adams *et al.*, "Development of Tomography Techniques Using a

Compact Fast Neutron Generator," pp. 51–60, 2018.

[98] F. Abbasian, G. I. Hadaller, and R. A. Fortman, "Single-phase and two-phase CFD simulations of the coolant flow inside a bruce/darlington candu flow channel," *Int. Top. Meet. Nucl. React. Therm. Hydraul. 2015, NURETH 2015*, vol. 9, pp. 7820–7829, 2015.

[99] G. D. Harvel, K. Hori, K. Kawanishi, and J. S. Chang, "Cross-sectional void fraction distribution measurements in a vertical annulus two-phase flow by high speed X-ray computed tomography and real-time neutron radiography techniques," *Flow Meas. Instrum.*, vol. 10, no. 4, pp. 259–266, Dec. 1999, doi: 10.1016/S0955-5986(99)00008-4.

[100] M. Wang, *Industrial Tomography: Systems and Applications*. 2015.

[101] G. A. Johansen and P. Jackson, *Radioisotope Gauges for industrial process measurements*. 2004.

[102] G. Knoll, "Radiation detection and measurement," *Wiley*, vol. 2008, no. June, 2005.

[103] J. R. Lamarsh, A. J. Baratta, and others, *Introduction to nuclear engineering*, vol. 3. Prentice hall Upper Saddle River, NJ, 2001.

[104] P. P. Bruyant, "Analytic and iterative reconstruction algorithms in SPECT," *J. Nucl. Med.*, vol. 43, no. 10, pp. 1343–1358, 2002.

[105] P. C. Hansen and J. S. Jørgensen, "AIR Tools II: algebraic iterative reconstruction methods, improved implementation," *Numer. Algorithms*, 2018, doi: 10.1007/s11075-017-0430-x.

[106] A. C. Kak and M. Slaney, *Principles of Computed Tomography*, 2nd ed. Society for Industrial and Applied Mathematics, 2001.

[107] M. Beister, D. Kolditz, and W. A. Kalender, "Iterative reconstruction methods in X-ray CT," *Phys. Medica*, vol. 28, no. 2, pp. 94–108, 2012, doi:

10.1016/j.ejmp.2012.01.003.

[108] T. Buzug, “Computed tomography: From photon statistics to modern cone-beam CT,” *Comput. Tomogr. From Phot. Stat. to Mod. Cone-Beam CT*, pp. 1–521, 2008, doi: 10.1007/978-3-540-39408-2/COVER.

[109] J. Diaz, “Radiation Transmission Imaging Applications for Nuclear Reactor Systems for Nuclear Reactor Systems,” 2022.

[110] T. Narabayashi, T. Tobimaksu, H. Nagasaka, and T. Kagawa, “Measurement of transient flow pattern by high speed scanning X-ray void fraction meter.,” 1984.

[111] D. R. Wyman and A. A. Harms, “Statistical uncertainty in the radiation diagnosis of two-phase flows,” *Nucl. Eng. Des.*, 1985, doi: 10.1016/0029-5493(85)90291-2.

[112] P. Andersson, E. A. Sundén, S. J. Svärd, and H. Sjöstrand, “Correction for dynamic bias error in transmission measurements of void fraction,” *Rev. Sci. Instrum.*, 2012, doi: 10.1063/1.4772704.

[113] J. Diaz, J. J. Serrano-Aguilera, V. Petrov, and A. Manera, “Development of a More Accurate Dynamic Bias Error Model for Two-Phase Flow Measurements Performed with Radiation Transmission,” *Int. J. Multiph. Flow*, vol. 146, no. October 2021, p. 103881, 2022, doi: 10.1016/j.ijmultiphaseflow.2021.103881.

[114] M. Wagner, A. Bieberle, M. Bieberle, and U. Hampel, “Dynamic bias error correction in gamma-ray computed tomography,” *Flow Meas. Instrum.*, 2017, doi: 10.1016/j.flowmeasinst.2016.10.012.

[115] P. R. Barrett, “SYSTEMATIC ERRORS IN THE DISCRETE TIME-INTERVAL TRANSMISSION METHOD FOR THE ESTIMATION OF VOID STATISTICS IN BOILING CHANNELS,” vol. 30, 1974.

[116] U. Hampel and M. Wagner, “A method for correct averaging in transmission radiometry,” *Meas. Sci. Technol.*, vol. 22, no. 11, 2011, doi: 10.1088/0957-0233/22/11/115701.

[117] N. Höflich and O. Pooth, “Studies on fast neutron imaging with a pixelated stilbene scintillator detector,” *Nucl. Instruments Methods Phys. Res. Sect. A Accel. Spectrometers, Detect. Assoc. Equip.*, vol. 1040, p. 167211, Oct. 2022, doi: 10.1016/J.NIMA.2022.167211.

[118] M. J. Joyce *et al.*, “Fast neutron tomography with real-time pulse-shape discrimination in organic scintillation detectors,” *Nucl. Instruments Methods Phys. Res. Sect. A Accel. Spectrometers, Detect. Assoc. Equip.*, vol. 834, pp. 36–45, 2016, doi: 10.1016/j.nima.2016.07.044.

[119] J. Csikai, *CRC Handbook of Fast Neutron Generators*. 1987.

[120] H. Kromer, R. Adams, and H. M. Prasser, “Development, design, and testing of a microwave-driven compact rotating-target D-D fast neutron generator for imaging applications,” *Appl. Radiat. Isot.*, vol. 174, p. 109715, Aug. 2021, doi: 10.1016/J.APRADISO.2021.109715.

[121] Saint-Gobain, “Organic Scintillation Materials and Assemblies.” p. 16, 2015, [Online]. Available: http://www.crystals.saint-gobain.com/uploadedFiles/SG-Crystals/Documents/SGC Organics Brochure.pdf.

[122] S. Yip, “Nuclear Radiation Interactions,” *Nucl. Radiat. Interact.*, Dec. 2014, doi: 10.1142/8275.

[123] J. R. Taylor, *Classical Mechanics*. Sausalito, California: University Science Books, 2005.

[124] J. J. Duderstadt and L. J. Hamilton, *Nuclear reactor analysis*. Wiley, 1976.

[125] M. Cecconello, “Liquid Scintillators Neutron Response Function: A

Tutorial," *J. Fusion Energy*, vol. 38, no. 3–4, pp. 356–375, 2019, doi: 10.1007/s10894-019-00212-w.

[126] P. Andersson, H. Sjöstrand, and S. Jacobsson Svärd, "Effects of proton escape on detection efficiency in thin scintillator elements and its consequences for optimization of fast-neutron imaging," *Nucl. Instruments Methods Phys. Res. Sect. A Accel. Spectrometers, Detect. Assoc. Equip.*, vol. 651, no. 1, pp. 110–116, Sep. 2011, doi: 10.1016/j.nima.2011.01.002.

[127] sensL, "Introduction to SiPM An Introduction to the Silicon Photomultiplier," *sensL*, pp. 1–16, 2011.

[128] S. S. Piatek and D. Ph, "Emerging Applications for Single-Photon Detection SiPM and SPAD : SiPM and SPAD : emerging applications."

[129] C. J. Wharton, E. H. Seabury, D. L. Chichester, A. J. Caffrey, J. Simpson, and M. Lemchak, "X-Ray Measurements Of A Thermo Scientific P385 DD Neutron Generator," *AIP Conf. Proc.*, vol. 1336, no. 1, p. 538, Jun. 2011, doi: 10.1063/1.3586158.

[130] S. Utrup *et al.*, "Design and performance of a 32-slice CT detector system using back-illuminated photodiodes," *Med. Imaging 2004 Phys. Med. Imaging*, vol. 5368, p. 40, 2004, doi: 10.1117/12.534646.

[131] LA-UR-17-29981, *MCNP User's Manual, Code Version 6.2*. 2017.

[132] S. Industries, "Starfire Industries® nGen™ 400 Operation Manual." 2021.

[133] Hamamatsu, "MPPC (Multi-Pixel Photon Counter) arrays S13361-3050 series." pp. 1–7, 2022.

[134] Saint Gobain, "Premium Plastic Scintillators," *Ceramics*. .

[135] Weeroc, "Petiroc 2A Datasheet," 2017.

[136] CAEN, "User Manual UM6698 A55PETx PETIROC Piggyback Board for

DT5550W.” 2020.

[137] A. G. M. Santos, R. S. F. Dam, W. L. Salgado, R. Schirru, and C. M. Salgado, “Determination of mass attenuation coefficient of polylactic acid using gamma densitometry in 50-1000 keV energy range,” 2020, doi: 10.1016/j.radphyschem.2020.109097.

[138] M. Yang *et al.*, “Center of rotation automatic measurement for fan-beam CT system based on sinogram image features,” *Neurocomputing*, vol. 120, pp. 250–257, Nov. 2013, doi: 10.1016/J.NEUCOM.2012.08.066.

[139] K. H. Jin, M. T. McCann, E. Froustey, and M. Unser, “Deep convolutional neural network for inverse problems in imaging,” *IEEE Trans. Image Process.*, vol. 26, no. 9, pp. 4509–4522, 2017.

[140] M. Nishio *et al.*, “Convolutional auto-encoders for image denoising of ultra-low-dose CT,” *Heliyon*, vol. 3, no. 8, Aug. 2017, doi: 10.1016/J.HELIYON.2017.E00393.

[141] H. Chen *et al.*, “Low-dose CT via convolutional neural network,” *Biomed. Opt. Express*, vol. 8, no. 2, pp. 679–694, 2017.

[142] T. Akiba, S. Sano, T. Yanase, T. Ohta, and M. Koyama, “Optuna: A Next-generation Hyperparameter Optimization Framework,” 2019, doi: 10.1145/3292500.3330701.

[143] S. Sun and X. Ouyang, “A simulation study of a fan-beam time-of-flight fast-neutron tomography system,” *Appl. Radiat. Isot.*, vol. 149, no. January, pp. 52–59, 2019, doi: 10.1016/j.apradiso.2019.04.017.

[144] M. M. Lell and M. Kachelrieß, “Recent and upcoming technological developments in computed tomography: High speed, low dose, deep learning, multienergy,” *Investigative Radiology*, vol. 55, no. 1. Lippincott Williams and Wilkins, pp. 8–19, Jan. 01, 2020, doi:

10.1097/RLI.0000000000000601.

[145] M. S. Johnson *et al.*, “Computed tomography with fast-neutron sources,” no. iCT, pp. 1–6, 2020.

[146] M. C. Wright, E. W. Nelius, J. T. Mihalczo, S. M. McConchie, and P. A. Hausladen, “Initial Investigation of the Small Feature Detection Capability of the ORNL Fast Neutron Tomographic Imaging System,” *2018 IEEE Nucl. Sci. Symp. Med. Imaging Conf. NSS/MIC 2018 - Proc.*, no. April, 2018, doi: 10.1109/NSSMIC.2018.8824304.

[147] C. L. Williams and A. C. Peterson, “Two-Phase Flow Patterns With High-Pressure Water in a Heated Four-Rod Bundle.,” *Nucl Sci Eng*, vol. 68, no. 1, pp. 155–169, 1978, doi: 10.13182/nse78-a27286.

[148] P. Venkateswararao, R. Semiat, and A. E. Dukler, “Flow pattern transition for gas-liquid flow in a vertical rod bundle,” *Int. J. Multiph. Flow*, vol. 8, no. 5, pp. 509–524, Oct. 1982, doi: 10.1016/0301-9322(82)90021-0.

[149] T. M. Anklam and R. F. Miller, “Void fraction under high pressure, low flow conditions in rod bundle geometry,” *Nucl. Eng. Des.*, vol. 75, no. 1, pp. 99–108, Apr. 1983, doi: 10.1016/0029-5493(83)90083-3.

[150] H. Kumamaru, M. Kondo, H. Murata, and Y. Kukita, “Void-fraction distribution under high-pressure boil-off conditions in rod bundle geometry,” *Nucl. Eng. Des.*, 1994, doi: 10.1016/0029-5493(94)90054-X.

[151] N. Takenaka, H. Asano, T. Fujii, and M. Matsubayashi, “Three-dimensional Void Fraction Measurement of Steady Two-phase Flow by Neutron Radiography Three-dimensional oid fraction distributions of a steady air- % vater two-phasc flow in a x4 rod-bundle with circular ferrule type spacers werc measured by neutron,” 1998.

[152] H. V. Kok, T. H. J. J. Van Der Hagen, and R. F. Mudde, “Subchannel void-

fraction measurements in a 6×6 rod bundle using a simple gamma-transmission method," *Int. J. Multiph. Flow*, 2001, doi: 10.1016/S0301-9322(00)00005-7.

[153] M. Kureta and H. Iikura, "Development of an ultra-high-speed scanning neutron tomography system for high-quality and four-dimensional visualizations," *Nucl. Instruments Methods Phys. Res. Sect. A Accel. Spectrometers, Detect. Assoc. Equip.*, vol. 605, no. 1–2, pp. 81–84, Jun. 2009, doi: 10.1016/j.nima.2009.01.164.

9 Appendix

9.1 Derivations

9.1.1 Void fraction

Using Figure 9.1.1 as a reference, the following is a derivation of the expression from [110].

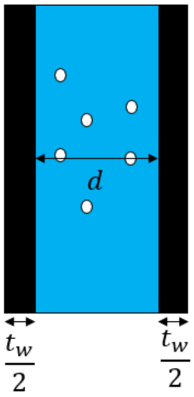

Figure 9.1.1: 2-phase flow in a tube.

If one were to take an empty test section reference sample (filled with air) and a reference with water filled, the relations according to Beer's law is:

$$I_a = I_0 \exp(-\mu_a \rho_a d) \exp(-\mu_{wall} \rho_{wall} t_w) \tag{1}$$

$$I_f = I_0 \exp(-\mu_f \rho_f d) \exp(-\mu_{wall} \rho_{wall} t_w) \tag{2}$$

And under two-phase flow conditions:

$$I_\phi = I_0 \exp\left(-\mu_f d\left(\rho_f'(1-\alpha) + \rho_v'\alpha\right)\right)\exp(-\mu_{wall}\rho_{wall}t_w) \tag{3}$$

Now, dividing equation 3 by equation 2:

$$\frac{I_\phi}{I_f} = \exp\left(d\mu_f\left(\rho_f - \left(\rho_f'(1-\alpha) + \rho_v'\alpha\right)\right)\right) \tag{4}$$

And equation 1 by equation 2:

$$\frac{I_a}{I_f} = \exp\left(d\left(\mu_f\rho_f - \mu_a\rho_a\right)\right) \tag{5}$$

Since d is the distance travelled in the region of measurement, it is the same in both equation 4 and 5. Thus, the equations can be related and solved for α.

$$\alpha = F\left(\frac{\ln\left(\frac{I_\phi}{I_f}\right)}{\ln\left(\frac{I_a}{I_f}\right)}\right) - G \tag{6}$$

Where:

$$F = \frac{\rho_f - \left(\frac{\mu_a}{\mu_f}\right)\rho_a}{\rho_f' - \rho_v'}$$

$$G = \frac{\rho_f - \rho'_f}{\rho'_f - \rho'_v}$$

Additionally, given that:

$$\ln\left(\frac{I_\phi}{I_f}\right) = d\left(\mu_f^{lin} - \mu_\phi^{lin}\right)$$

$$\ln\left(\frac{I_a}{I_f}\right) = d\left(\mu_f^{lin} - \mu_a^{lin}\right)$$

The relation becomes:

$$\alpha = F\left(\frac{\mu_\phi^{lin} - \mu_f^{lin}}{\mathrm{\mu}_\mathrm{a}^{lin} - \mu_f^{lin}}\right) - G \quad \blacksquare$$

9.1.2 Chordal void fraction error equation

Main equation:

$$\boldsymbol{\alpha = \frac{\ln\left(\frac{I_{2\phi}}{I_l}\right)}{\ln\left(\frac{I_v}{I_l}\right)} = \frac{\ln(I_{2\phi}) - \ln(I_l)}{\ln(I_v) - \ln(I_l)} = \frac{\mu_l - \mu_{2\phi}}{\mu_l - \mu_v}}$$

The error equation is expressed as the error for a function of several variables:

$$\boldsymbol{\sigma_\alpha^2 = \left(\frac{\partial\alpha}{\partial I_{2\phi}}\right)^2 \sigma_{I_{2\phi}}^2 + \left(\frac{\partial\alpha}{\partial I_l}\right)^2 \sigma_{I_l}^2 + \left(\frac{\partial\alpha}{\partial I_v}\right)^2 \sigma_{I_v}^2}$$

By expressing count rate in the form:

$$I_x = \frac{N_x}{t_x}$$

where N_x is the number of counts and t_x is the capture time for case x (**note that the time is assumed to have no error in this derivation**), the errors can be expressed as:

$$\sigma_{I_x}^2 = \left(\frac{\partial I_x}{\partial N_x}\right)^2 \sigma_{N_x}^2$$

The error for N_x is simple to find as it is based on poisson statistics. The errors for each case are:

$$\sigma_{N_{2\phi}}^2 = N_{2\phi},\ \left(\frac{\partial I_{2\phi}}{\partial N_{2\phi}}\right)^2 = \frac{1}{t_{2\phi}^2},\ \boldsymbol{\sigma_{I_{2\phi}}^2 = \frac{N_{2\phi}}{t_{2\phi}^2}}$$

$$\sigma_{N_l}^2 = N_l, \left(\frac{\partial I_l}{\partial N_l}\right)^2 = \frac{1}{t_l^2},\ \boldsymbol{\sigma_{I_l}^2 = \frac{N_l}{t_l^2}}$$

$$\sigma_{N_v}^2 = N_v, \left(\frac{\partial I_v}{\partial N_v}\right)^2 = \frac{1}{t_v^2},\ \boldsymbol{\sigma_{I_v}^2 = \frac{N_v}{t_v^2}}$$

The derivative terms become:

$$\boldsymbol{\left(\frac{\partial\alpha}{\partial I_{2\phi}}\right)^{2}} = \left(\frac{I_l}{I_{2\phi}}\right)\left(\frac{1}{I_l}\right)\left(\frac{1}{\ln\left(\frac{I_v}{I_l}\right)}\right) = \boldsymbol{\frac{1}{I_{2\phi}}\left(\frac{1}{\ln\left(\frac{I_v}{I_l}\right)}\right)}$$

$$\left(\frac{\partial\alpha}{\partial I_l}\right)^{2} = \left(\frac{1}{\left(\ln\left(\frac{I_v}{I_l}\right)\right)^{2}}\right)\left(\left(\frac{I_l}{I_{2\phi}}\right)\left(\frac{-I_{2\phi}}{I_l^2}\right)\left(\ln\left(\frac{I_v}{I_l}\right)\right) - \left(\frac{I_l}{I_v}\right)\left(\frac{-I_v}{I_l^2}\right)\left(\ln\left(\frac{I_{2\phi}}{I_l}\right)\right)\right)$$

$$\boldsymbol{\left(\frac{\partial\alpha}{\partial I_l}\right)^{2}} = \frac{\left(\frac{1}{I_l}\right)\left(\ln\left(\frac{I_{2\phi}}{I_v}\right)\right)}{\left(\ln\left(\frac{I_v}{I_l}\right)\right)^{2}} = \boldsymbol{\frac{-(1-\alpha)}{I_l}\left(\frac{1}{\ln\left(\frac{I_v}{I_l}\right)}\right)};\ \frac{\ln\left(\frac{I_{2\phi}}{I_v}\right)}{\ln\left(\frac{I_v}{I_l}\right)} = -(1-\alpha)$$

$$\boldsymbol{\left(\frac{\partial\alpha}{\partial I_v}\right)^{2}} = \frac{\left(-\ln\left(\frac{I_{2\phi}}{I_v}\right)\right)\left(\frac{I_l}{I_v}\right)\left(\frac{1}{I_l}\right)}{\left(\ln\left(\frac{I_v}{I_l}\right)\right)^{2}} = \boldsymbol{\frac{-(\alpha)}{I_v}\left(\frac{1}{\ln\left(\frac{I_v}{I_l}\right)}\right)}$$

$$\sigma_{\alpha}^{2} = \frac{1}{I_{2\phi}^{2}}\left(\frac{1}{\ln\left(\frac{I_v}{I_l}\right)}\right)^{2}\frac{N_{2\phi}}{t_{2\phi}^{2}} + \left(\frac{-(1-\alpha)}{I_l}\left(\frac{1}{\ln\left(\frac{I_v}{I_l}\right)}\right)\right)^{2}\frac{N_l}{t_l^{2}} + \left(\frac{-(\alpha)}{I_v}\left(\frac{1}{\ln\left(\frac{I_v}{I_l}\right)}\right)\right)^{2}\frac{N_v}{t_v^{2}}$$

Since $I_x = \frac{N_x}{t_x}$,

$$\sigma_{\alpha} = \frac{1}{\ln\left(\frac{I_v}{I_l}\right)}\sqrt{\frac{1}{N_{2\phi}} + \frac{(1-\alpha)^{2}}{N_l} + \frac{\alpha^{2}}{N_v}}$$

$$\frac{\sigma_{\alpha}}{\alpha} = \frac{1}{\ln\left(\frac{I_{2\phi}}{I_l}\right)}\sqrt{\frac{1}{N_{2\phi}} + \frac{(1-\alpha)^{2}}{N_l} + \frac{\alpha^{2}}{N_v}}$$

9.1.3 Dynamic bias error

The time averaged void fraction is represented by

$$\langle\alpha\rangle = \frac{1}{\tau}\int_{0}^{\tau}\alpha(t)\,\mathrm{d}t$$

Ideally, this would be the measurement that is made by the system. However, the attenuation is not a linear function, and instead is exponential. So, the actual measurement made by the system is the time average of the attenuation due to a void distribution, not the void fraction itself:

$$\langle T \rangle = \frac{1}{\tau} \int_0^{\tau} \exp\big(\lambda \alpha(t)\big)\, dt$$

Therefore, the void fraction that is represented by the measurement is actually:

$$\alpha_m = \frac{1}{\lambda} \ln\left(\frac{1}{\tau} \int_0^{\tau} \exp\big(\lambda \alpha(t)\big)\, dt\right)$$

Which is clearly different than the actual time averaged void fraction. The difference between the measured void fraction, and the actual average void fraction is deemed the dynamic bias error:

$$\Delta\alpha = \langle \alpha \rangle - \alpha_m$$

9.1.4 SART algorithm

The SART algorithm as given in the AIRTools II toolbox is[105]:

$$\boldsymbol{x}^{i+1} = \boldsymbol{x}^{i} + \lambda \boldsymbol{D} \boldsymbol{A}^{T} \boldsymbol{M}\big(\boldsymbol{p} - \boldsymbol{A}\boldsymbol{x}^{i}\big)$$

Where $\boldsymbol{x}$ is the image vector estimate, λ is the relaxation parameter (set to 1.9 by default), $\boldsymbol{A}$ is the system matrix, $\boldsymbol{D}$ is a diagonal matrix of the inverse of the row sums of $\boldsymbol{A}$, $\boldsymbol{M}$ is a diagonal matrix of the inverse of the column sums of $\boldsymbol{A}$, and $\boldsymbol{p}$ is the projection vector.

9.2 Detector processing

9.2.1 Bulk scintillator experiments

The first task for the detection system was to explore the difference between bulk and pixelated scintillator. Bulk crystals are cheaper and easier to manufacture than the pixelated scintillators. Such bulk scintillators have been used with SiPM detectors, but this is due to using individual pixels as opposed to arrays. It was thought that the mirrored surfaces that divide the pixels would increase the light collection of the SiPM whereas the bulk scintillator light collection will be more diffuse (Figure 9.2.1).

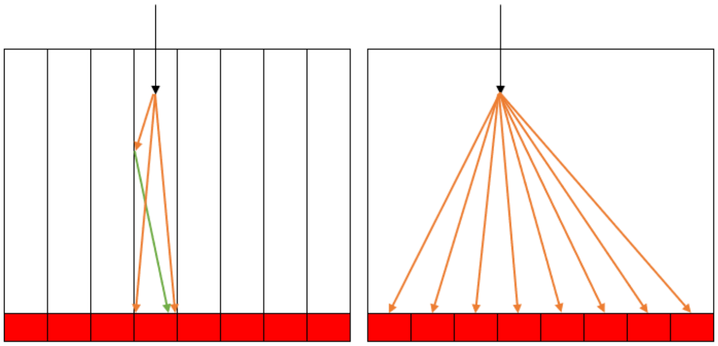

Figure 9.2.1: Pixelated (left) vs bulk (right) scintillator light collection.

Measurements were made using a 1µCi Na-22 gamma source with both a bulk and pixelated CsI(Tl) scintillator attached to an array, with one pixel output. The resultant spectra show that energy resolution and counting uniformity are significantly reduced when using a bulk scintillator over a pixelated scintillator, and thus a pixelated array is better suited for this application (Figure 9.2.2). It should be noted that if all the pixel responses are added together upon readout, the output spectrum would be the same as the single pixel readout case since most of the light from the interaction would be collected (aside from light escaping the scintillator).

Additionally, the energy response of the pulse processing electronics was tested using a 1μCi Na-22 source as well as a 1μCi Cs-137 source with the CsI(Tl) pixelated scintillator with the readout of one pixel (Figure 9.2.3). The resultant spectra show both the peak and Compton edge with modest energy resolution.

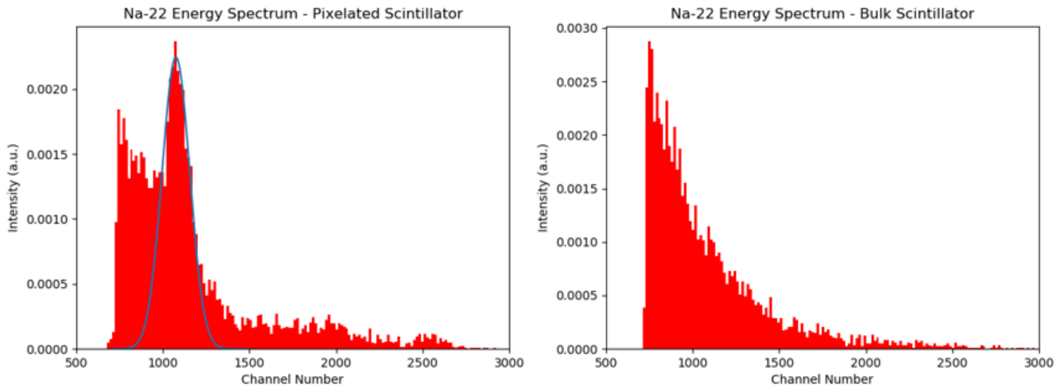

Figure 9.2.4: Comparison of pixelated and bulk scintillator response

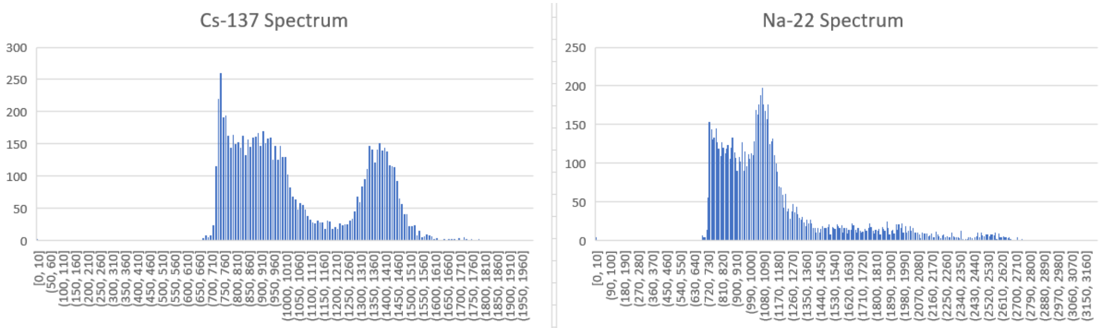

Figure 9.2.5: Sample spectra from the pulse processing electronics

9.2.2 Peak timing derivation

The output of the CR-RC shaper is used to determine both the hold delay and the energy calibration. To determine the hold delay, the shaper peaking time must be calculated. To do this, a simplified model is used to determine the output response due to an ideal step input. The output pulse shape of a CR-RC shaper due to a step input signal can be expressed as

$$V_{out}(t) = \frac{V_0 \tau_1}{\tau_1 - \tau_2}\left(\exp\left(-\frac{t}{\tau_1}\right) - \exp\left(-\frac{t}{\tau_2}\right)\right)$$

The peaking time is the time to obtain the peak value of the voltage and is simply found by taking the derivative:

$$T_p = \frac{\tau_1 \tau_2}{\tau_1 - \tau_2} \ln\left(\frac{\tau_1}{\tau_2}\right)$$

And for equal time constant shapers the peaking time is:

$$T_p = \tau$$

This information is converted to an 8-bit time delay signal for the sample and hold system using the given expression

$$T_{8bit} = \frac{T_p\ [\mathrm{ns}] - 27\ [\mathrm{ns}]}{0.34\ \left[\frac{\mathrm{ns}}{\mathrm{unit}}\right]}$$

9.3 Standard operating procedures

9.3.1 Initial Startup

1. Set the desired object (or no object) on the rotation stage for imaging.
2. Open the control software for the rotation stage by going to the start menu and searching "APTUser". Info can be found here on page 8.
3. Calibrate the rotation stage.
    a. Any angle can be entered and set.
4. Check that the detector config file has the correct board entries and settings
    a. Check the HV on after acquiring setting and set it to stay on after acquiring. This helps with readout stability and time.

       Set -> "switch_off_hv_on_end" : false

    b. Set the desired projection scan time

       Set -> "TargetValue": t where t is the desired scan time in seconds
5. Open the ngen control software by searching "ngen Controller" in the start menu to connect the generator.
6. Set to desired voltage.
7. **Set Interlock**.
8. After the interlocks are set, head to the control room and turn on the generator. Wait for the output (anode current) to stabilize.
    a. Watch the current in the plot and acquire when the level is pretty much stable (~2-5 minutes usually). Corrections in post-processing can account for unstable operation, but this makes the readouts more reliable in general.

9. Proceed to the **Operation** section.

9.3.2 Operation

1. Activate the “MultiboardDAQDT5550W_PETIROC.exe” executable to acquire a detector readout on all boards.
2. Use the rotation stage software to rotate the object to the next desired angle.
3. Repeat until all desired angles are acquired.
4. If another acquisition is required, turn off the generator and go to the **Secondary run** section. If not, proceed to the Shutdown section.

9.3.3 Secondary run

1. Set the desired object (or no object) on the rotation stage for imaging.
2. Check that the detector config file has the correct board entries and settings
    a. Check the HV on after acquiring setting and set it to stay on after acquiring

       Set -> "switch_off_hv_on_end" : false

    b. Set the desired projection scan time

       Set -> "TargetValue": t where t is the desired scan time in seconds
3. Open the ngen control software by searching “ngen Controller” in the start menu to connect the generator.
4. Set to desired accelerator voltage.
5. **Set Interlock**.
6. After the interlocks are set, head to the control room, and turn on the generator. Wait for the output (anode current) to stabilize.

   b. Watch the current in the plot and acquire when the level is pretty much stable (~2-5 minutes usually). Corrections in post-processing can account for unstable operation, but this makes the readouts more reliable in general.

9.3.4 Shutdown

1. Set the generator to “off”.
    a. Make sure the readings from the dose monitors are zero.
2. Disable interlocks.
3. Enter the room and shut off the neutron generator.
    a. Turn off the power and press down the E-stop switch.
4. Turn off detector systems
    a. Turn off each power switch
    b. Unplug each board unit
5. Turn off the rotation stage controller.
    a. Turn off power switch
    b. Unplug the unit
6. Close all programs